Theses and Dissertations

12-15-2014

Surface Modification of Nanoplatelets in Polymer Nanocomposites

Shailesh K. Shori

University of South Carolina - Columbia

Follow this and additional works at: http://scholarcommons.sc.edu/etd

Surface Modification of Nanoplatelets in Polymer Nanocomposites

by

Shailesh K. Shori

Bachelor of Science
University of Cincinnati, 2003

Master of Science
The Pennsylvania State University, 2008

Submitted in Partial Fulfillment of the Requirements

For the Degree of Doctor of Philosophy in

Chemical Engineering

College of Engineering and Computing

University of South Carolina

2014

Accepted by:

Harry J. Ploehn, Major Professor

James A. Ritter, Committee Member

John W. Weidner, Committee Member

Hans-Conrad zur Loye, Committee Member

Lacy Ford, Vice Provost and Dean of Graduate Studies

Acknowledgements

Abstract

In polymer nanocomposites (PNCs), it is very important that the nanofiller (typically an inorganic) is well-dispersed in an organic polymer matrix. Optimal compatibility results in end-use products such as packaging materials with enhanced properties. In practice, however, this is challenging to achieve because "ideal" dispersions require the complete uniform separation, termed exfoliation, of the nanofiller within the matrix. As a result, different nanofillers including calcium niobate (CN) and montmorillonite (MMT) are first studied for their ability to exfoliate in aqueous suspensions by measuring the organic cation uptake. The cation exchange capacity, or CEC, determined that CN needs further work before introduction into a polymer matrix, while MMT is more suitable for directly making PNCs. As hypothetical solutions, both nanofillers are surface modified (after ion-exchange) and evaluated by characterization testing.

To improve compatibility, the covalent grafting of phenylphosphonate (PPA) onto exfoliated, protonated calcium niobate (HCN) was explored. PPA can be readily grafted onto the face surfaces of exfoliated HCN, which has reactive apical oxygen atoms. HCN can be fully exfoliated in aqueous solutions of tetrabutylammonium hydroxide (TBAOH), denoted as TBACN. The effect of reflux conditions on the dispersion state of TBACN suspensions was investigated, along with PPA grafting onto both non-exfoliated HCN and exfoliated TBACN dispersed in deionized (DI) water, TBA solution, and

various alcohols. The characterization results confirm the grafting of PPA on HCN and TBACN, quantify the extent of PPA grafting, and identify various grafting modes (mono-, bi-, and tridentate). All of these aspects are found to be dependent on the layered materials' exfoliation state, suspension processing conditions, and solvent composition.

The factors that control the dispersion of exfoliated MMT in poly(vinyl alcohol) (PVOH) during solution blending and solvent evaporation were also studied in making polymer nanocomposite films. Dynamic light scattering (DLS) indicates that addition of dilute suspensions of fully exfoliated MMT platelets to aqueous PVOH solutions results in undesired particle aggregation and thus poor MMT dispersion in cast films. It is believed that PVOH bridging induces MMT platelet aggregation. To counteract bridging aggregation, the novel idea of pretreating the MMT surface with a small amount of compatible polymer prior to solution blending with PVOH was explored. It is hypothesized that "pretreating" the MMT platelet surfaces with adsorbed polymer in dilute suspensions will protect the platelets from bridging aggregation during solution blending and solvent evaporation. DLS shows that pretreated MMT platelets are less susceptible to aggregation during blending with PVOH solutions. Characterization results compare the crystalline structure, thermal properties, dynamic mechanical properties, gas permeability, and dissolution behavior of MMT/PVOH films incorporating untreated versus pretreated MMT.

Table of Contents

List of Tables

List of Figures

xvii

Introduction

        Polymer nanocomposites (PNCs) are extensively utilized in numerous products and across a wide variety of industries. In essence, the difference between a pure polymer and a PNC as the choice of use for application is the addition of a suitable nanofiller, an inorganic material consisting of stacked layers at the nanoscale, to the polymer "matrix". The purpose is to enhance the physical properties of the pure or "neat" polymer that becomes a PNC with embedded nanofiller so as to improve performance. This is achieved by creating an interfacial phase due to the nanofiller dispersed within the "bulk" phase of the polymer. For optimal results, the nanofiller layers need to be completely separated and dispersed uniformly throughout, called exfoliation. In practice, this is challenging because of the inorganic/organic incompatibility between the phases that typically results in aggregation.

        There are various techniques to make PNCs. Solution blending, melt extrusion, and in situ polymerization are commonly employed among others. Solution blending is the chosen route to make "model" or "ideal" PNCs, and therefore the focus for this work. "Ideal" PNCs consist of nanofillers uniformly dispersed within the matrix resulting in the direct enhancement of properties and performance. For this to happen, the polymer must be able to strongly adsorb onto the surface of the filler nanoparticles. A common solvent is also needed that both produces stable suspensions of exfoliated nanoparticles while also solubilizes the polymer so that the two can be smoothly blended together. The

selection of water calls for the studied nanofillers (montmorillonite and calcium niobate-see next paragraph) to be able to exfoliate in aqueous suspensions. On the other hand, poly(vinyl alcohol) (PVOH) is a water-soluble polymer that is widely available that can readily adsorb onto nanofillers including montmorillonite. It is also critical to control the quality of the dispersion during solvent evaporation in forming the polymer nanocomposite with the solution blending method. If these conditions are not met, PNCs with sub-optimal properties may result.

To improve compatibility and to make more "ideal" PNCs, ion-exchange and surface modification of nanofillers are two possible solutions. Calcium niobate (CN) – a Dion-Jacobson synthetic perovskite – and montmorillonite (MMT), a naturally-occurring silicate, are both platelet-shaped nanofillers studied in this work. In Chapter 1, the organic cation uptake (or cation exchange capacity) of the nanoplatelets was measured as an "indicator" for how well they may disperse in aqueous suspensions prior to adding to a polymer. Using these results proceeding forward, Chapter 2 describes the surface modification of CN by covalently grafting phenylphosphonate as a first step towards improving compatibility. Lastly, Chapter 3 is devoted to determining the effect of "pretreating" the surface of MMT with low-weight compatible polymers in PVOH nanocomposites by characterization testing.

Chapter 1: Organic Cation Uptake

1.1. Introduction

Chapter 1 discusses the measurement of the organic cation uptake of various nanofillers including CN and MMT utilizing two methods: cation exchange and TGA. For cation exchange, a copper ethylenediamine complex was mixed with a nanofiller and measured for light absorbance; while TGA provided weight loss data for CN after cation exchange. The purpose of measuring the organic cation uptake is to evaluate a nanofiller's ability to uniformly disperse in aqueous suspensions. This provides a good "indicator" of how well a particular nanofiller may disperse in a polymer matrix, or whether the nanofiller may need further work before making a polymer nanocomposite (PNC).

1.2. Copper Ethylenediamine Method

The cation exchange capacity (CEC) is a measure that can quantify the ability of a nanomaterial to readily disperse in a suspension by exchanging cations. An established protocol for measuring the CEC of clay minerals [1, 2] was adapted to explore the organic cation uptake by protonated CN (HCN) and Na^+ MMT (Cloisite Na^+, Southern

Clay Products). To start, 1.0 M solutions of copper (II) chloride dihydrate (Alfa Aesar) and ethylenediamine (EDA, Alfa Aesar) are mixed in a 1:2 volume ratio, followed by dilution with deionized (DI) water to produce a 0.1 M $Cu(EDA)_2^{+2}$ stock solution. The stock solution is further diluted to make a series of standard solutions with concentrations ranging between 0.002 M and 0.020 M. The solutions' absorbances (at 548 nm and 800 nm) are measured by UV-vis spectrophotometry (model UV-2101PC, Shimadzu). The absorbance at 800 nm is subtracted from that at 548 nm to correct for light scattered by dust or residual particles in the solutions. This data is used to construct a calibration curve giving $[Cu^{+2}]$ as a function of corrected absorbance at 548 nm.

For determining cation uptake by HCN, 0.1 g of inorganic powder was added to 10 mL aliquots of each of the standard solutions, mixed for 15 minutes, and centrifuged (Eppendorf Centrifuge 5403, Brinkmann) at 6500 rpm for 30 minutes. The absorbances of the supernatant solutions were measured by UV-vis spectrophotometry, again subtracting the absorbance at 800 nm from that at 548 nm to correct for light scattered by residual particles in the solutions. The calibration curve is used to determine $[Cu^{+2}]_{residual}$ in the solutions. For each solution, $[Cu^{+2}]_{initial}$-$[Cu^{+2}]_{residual}$ gives the moles of Cu^{+2} per liter exchanged into the inorganic powder. Using the solution volume (10 mL) and the powder mass for each sample, $[Cu^{+2}]_{initial}$ and $[Cu^{+2}]_{residual}$ are converted to mEq per 100 g of powder sample and plotted as $[Cu^{+2}]_{residual}$ as a function of $[Cu^{+2}]_{initial}$ (Figure 1.1). A linear fit of the data points at higher $[Cu^{+2}]_{initial}$ values intersects the x-axis at the CEC value (0.405 meq/g).

Utilizing this method (Figure 1.1), we also measured the cation uptake of 0.829 meq/g for Na$^+$ MMT, in good agreement with literature values for cation exchange capacity [2] and the manufacturer's reported CEC value of 0.92 meq/g as measured by ammonium acetate titration. The CEC for MMT is approximately twice that of HCN, meaning that MMT can be dispersed more easily (after proton exchange with Na$^+$) into completely exfoliated dispersions in aqueous suspensions. This is because a higher CEC value means that more cations in a nanofiller can be exchanged out for other cations more facilely in a suspension that allows for the layered stacks to separate into individual platelets. The physical separation of the negatively charged platelets can occur either by electrostatic repulsion such as in water (MMT) or by introducing a bigger cation that gets in between more compact nanosheets (CN) and forces the larger basal spacing. Figure 1.2 shows the stability of CEC values for various nanofillers including magadiite before and after ion-exchange with time.

Nanofillers that are characterized to have higher CEC values tend to disperse more completely and more uniformly in a suspension than those with lower values. This means that an aqueous MMT suspension, for example, will provide a greater exposed surface area that allows for the amplification of enhanced interfacial properties upon addition into a polymer matrix than say an aqueous suspension of CN platelets. Therefore, the properties of MMT in PNCs can be directly studied (Chapter 3), while HCN requires further work (Chapter 2) beginning with introducing a bulky cation TBA$^+$, tetrabutylammonium, to achieve exfoliation via cation exchange. TGA can be used to measure the organic uptake of TBA$^+$ by HCN in the next section.
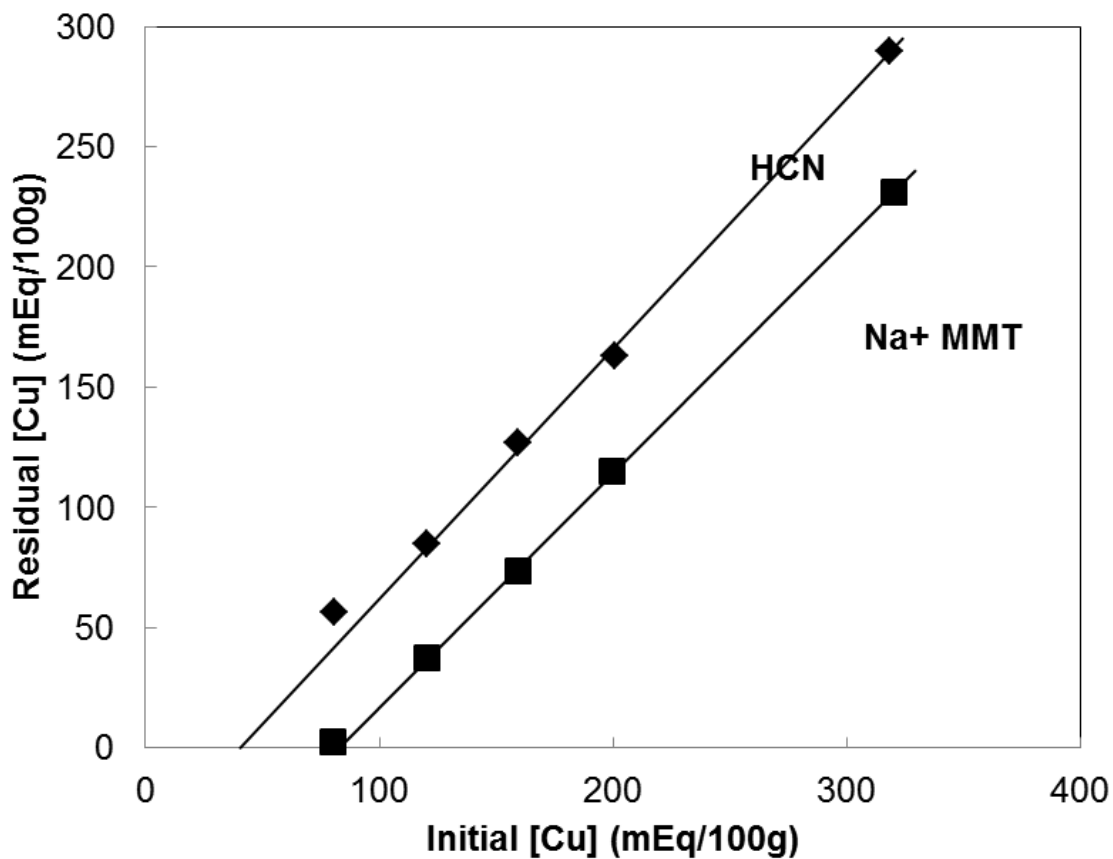
Figure 1.1. Plot of residual Cu^{2+} concentration versus initial Cu^{2+} concentration (expressed in units of mEq per 100 g of either HCN or MMT, as indicated) for determination of cation uptake values. The x-axis intercepts of the linear fits (solid lines based on three highest data points) give cation uptake values of 0.405 mEq/g and 0.829 mEq/g for HCN and MMT, respectively.
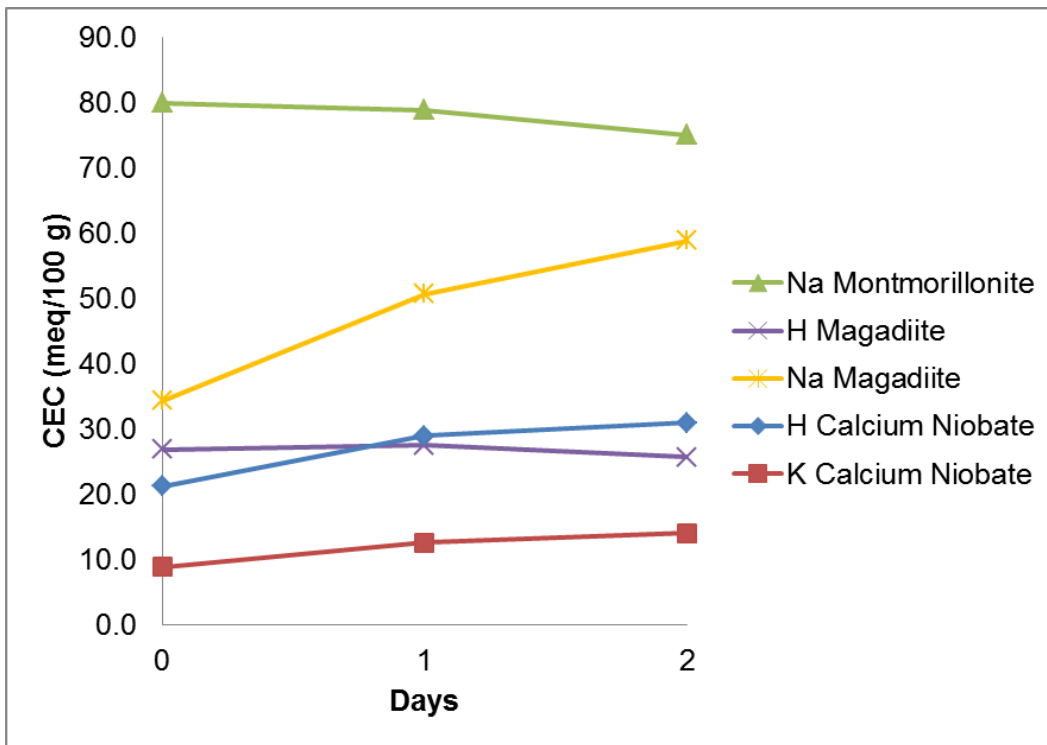
Figure 1.2. CEC values of various nanofillers before and after ion-exchange with time.

1.3. TBA$^+$ Uptake of HCN as Measured by TGA

Samples for TGA were prepared from aqueous suspensions (HCN and 1:1 molar TBA$^+$:CN unit cells, henceforth TBACN) that were stirred for at least 7 days. After centrifuging for 1 h at 6000 rpm, the recovered solid fraction was dried in an oven for 12 h at 50°C prior to TGA measurement. Figure 1.3 shows that the HCN sample lost 0.41% of its mass upon heating to 150°C, presumably due to water loss. Between 150°C and 330°C, the remaining dry HCN (99.59% of the original sample) lost another 1.73% of its mass due to a dehydration reaction producing calcium hexaniobate ($Ca_4Nb_6O_{19}$), as observed previously [3].

The TBACN sample lost a total of 8.67% of its mass when heated to 700°C (Figure 1.3). The shape of the weight loss curve makes it difficult to resolve the distinct contributions from water loss, TBA decomposition, and water elimination via the dehydration reaction. To estimate the TBA weight loss, we assume that (1) the 1.16% mass decrease up to 150°C is entirely due to water; (2) the dehydration reaction accounts for 1.73% of the total mass loss up to 700°C; and (3) the residue at 700°C is $Ca_4Nb_6O_{19}$. Assumptions (1) and (2) imply that of the 8.67% total mass loss, 5.78% was due to TBA decomposition. Using 1.0 g of the starting TBACN solids as a basis, the TBA decomposition accounted for 0.0578 g (0.239 mmol) and left 0.9133 g of $Ca_4Nb_6O_{19}$ residue (0.894 mmol, corresponding to 1.788 mmol of HCN). The TBA:CN molar ratio is thus estimated to be about 0.134. The results presented here are discussed further in Chapter 2.
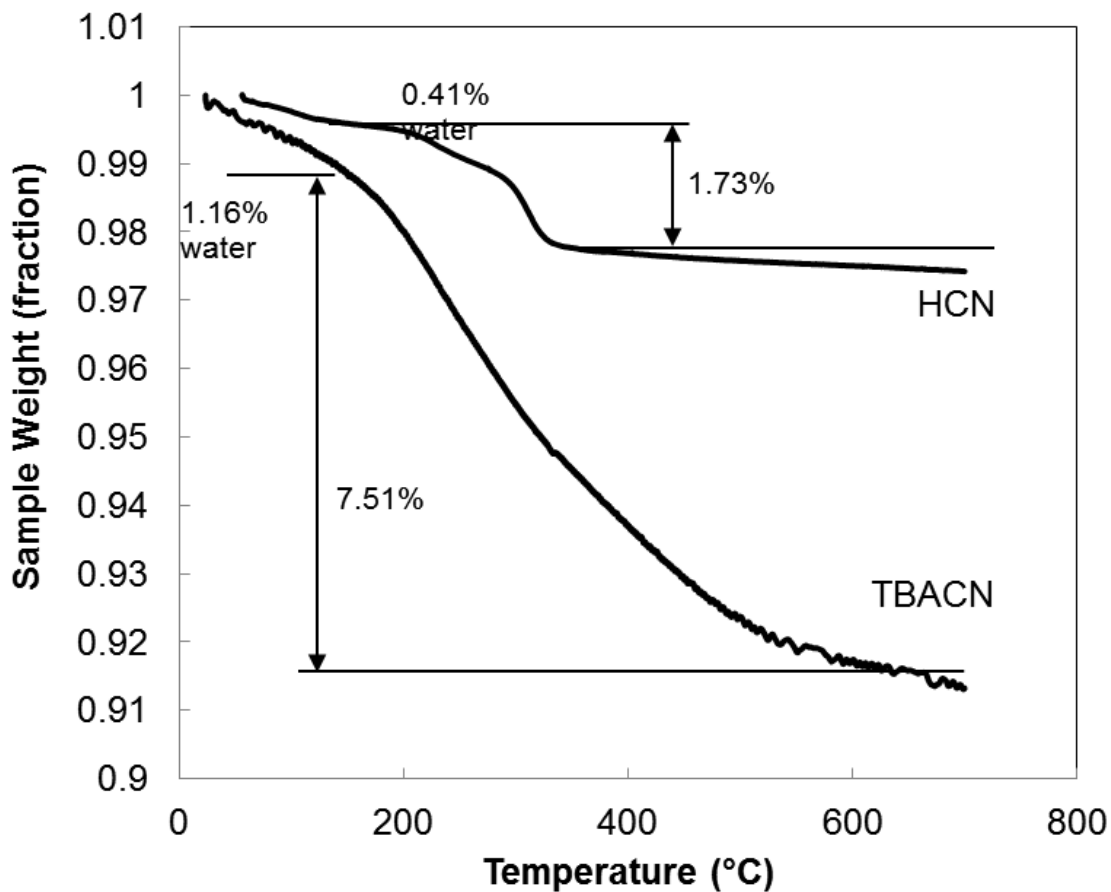
Figure 1.3. Sample weight (expressed as a fraction of initial sample weight) versus temperature for HCN and TBACN, as measured by TGA.

Chapter 2: Covalent Grafting of Phenylphosphonate on Calcium Niobate Platelets

Calcium niobate (CN) requires further study before introduction in a polymer matrix based on the organic cation uptake results presented back in Chapter 1. In Chapter 2, a step is taken closer in that direction. After proceeding with cation exchange of protonated calcium niobate with tetrabutylammonium in order to achieve full exfoliation, the surface of CN is further modified by covalently grafting phenylphosphonate (PPA) under various experimental conditions. Several characterization techniques are then employed to demonstrate grafting, which allows inorganic CN to now become functionalized with organic groups that serve as the starting point for making tailored polymer-grafted platelets. Thus, polymer nanocomposites (PNCs) may be composed of compatible, exfoliated CN platelets.

2.1. Introduction

Inorganic platelets exfoliated in stable suspensions are potential building blocks for making PNCs with enhanced properties and performance. In PNCs, the platelet-polymer interface (really an "interphase") plays two crucial roles. First, the interphase should promote platelet-polymer compatibility and thus platelet dispersion in the polymer, maximizing interfacial area. Second, the interphase should have structure and properties distinct from those of the bulk phases, as well as beneficial to performance in end-use applications.   Synergy   is   achieved   when   both   roles   are

fulfilled, because the interphase's beneficial properties are amplified by the high interfacial area/volume ratio achieved when the platelets are well dispersed.

Considerable research has focused on methods of adding organic functional groups to the surface of inorganic platelets to improve polymer-platelet compatibility. The classic example is ion exchange treatment of clay mineral platelets (e.g., montmorillonite) with alkyl ammonium cations to render them more hydrophobic. Although this improves clay platelet compatibility with polymers, it does not (at least by design) contribute significantly to improving composite functionality through beneficial interphase structure or properties.

Covalent organic functionalization of platelet surfaces can be used to tailor the interphase to enhance platelet compatibility with polymers and create "designer" interphase structures. Silane grafting chemistry is well established for layered aluminosilicates (e.g., laponite [4-8] and montmorillonite [9-16]) via condensation reactions with surface silanol or aluminol groups. Surface modification using organophosphonic acids (oPAs) [17, 18], reviewed recently, offers enhanced hydrolytic stability relative to silane grafting [17, 19]. Various oPAs have been used to chemically modify ceramic membranes [20, 21], oxide particles [22-26], oxide thin films [27], hydroxyapatite [28], and porous zeolites [29]. Grafting of oPAs onto the interlamellar face surfaces of layered inorganics has been reported for kaolinite [30, 31], natural phlogopite [32], hydrotalcite [33], layered silicates [34], and layered double hydroxides [35-38]. Functionalization of polymers with oPAs [39] and polymers carrying oPA functionality [40] have also been studied.

This work explores the covalent surface functionalization of inorganic layered perovskites [41-43] with oPAs. In the past, the surfaces of layered perovskites have been modified via acid treatment [44] or other kinds of ion-exchange [45-50]. Several papers describe various approaches for covalent surface modification of layered perovskites. For example, *n*-alkoxy groups have been grafted to the interlayer surfaces of proton-exchanged niobate [51-54], titanate [55], and tantalite [56] perovskites. Alcohol-functionalized niobates have been used as the starting point for subsequent grafting reactions, such as interlayer polyether grafting [57]. Shimada et al. [58] first functionalized the interlayer surfaces of $HLaNb_2O_7 \bullet xH_2O$ with *n*-propanol, exchanged it for *n*-decanol, and then proceeded with interlayer grafting using phenylphosphonic acid (PPA) and *n*-alkylphosphonic acids. The work of Shimada et al. is the only report to date of covalent functionalization of a layered perovskite with any oPA.

It is well known that layered perovskites may be exfoliated via cation exchange with bulky alkylammonium cations in aqueous suspensions [41, 42, 59-67]. Much of this work focused on calcium niobate, $KCa_2Nb_3O_{10}$ (KCN), or its proton-exchanged form, $HCa_2Nb_3O_{10} \bullet 1.5H_2O$ (HCN). Using AFM with quantitative image analysis, Gao et al. [67] proved that complete exfoliation of HCN in aqueous suspensions requires at least a 1:1 molar ratio of tetrabutylammonium cations (TBA^+) to calcium niobate (CN) unit cells. Use of lower TBA^+ concentrations (or less bulky cations) result in incomplete CN exfoliation. Steric interactions among bulky TBA^+ cations limit the exchange of H^+ for TBA^+ to about 15-20% of the theoretical cation exchange capacity. Thus the surface of (TBA,H)CN (henceforth denoted as TBACN) has a significant number of Lewis acid

sites (Nb-OH) available for reaction with oPAs. No one to date has explored the possibility of covalent surface modification of TBA-exfoliated CN by oPAs.

This work investigates the covalent grafting of PPA onto TBA-exfoliated CN platelets. In particular, we explore the effect of solvent (water, aqueous TBA solution, alcohols) on grafted amount and binding mode. Dynamic light scattering (DLS) characterizes the dispersion state of TBACN platelets in suspension. ^{31}P MAS NMR data prove that PPA has grafted onto TBACN, and XRD results identify conditions for which grafting occurs on platelet face surfaces, as opposed to edges and exterior particle surfaces. XPS results provide estimates of the PPA grafted amount. Finally, FT-IR, NMR, and XPS spectra provide evidence of different binding modes of PPA on CN platelet surfaces.

Our investigation is timely and relevant for two reasons. First, CN and related layered perovskite materials are well known as active photocatalysts with significant potential for hydrogen production via water hydrolysis [68-78]. Recent work has shown that TBA-exfoliated CN in water can be used to produce hydrogen gas [79-85]. Surface modification of CN may be useful for maintaining its suspension stability and tailoring its interfacial photocatalytic properties. However, CN's photocatalytic activity may make it difficult to covalently graft organic molecules onto its face surfaces, so this question merits investigation. Second, prior studies of grafting onto layered perovskites (reviewed earlier) all used organic solvents and examined interlayer reactions without consideration of exfoliation. Compared to the multistep process of Shimada et al. [58], facile TBA-mediated exfoliation of CN followed by grafting in aqueous suspensions may be a more straightforward route to organically-modified CN and related perovskites.

13

2.2. Materials and Methods

2.2.1. Materials

2.2.1.1. Exfoliated CN Suspension

Calcium niobate ($KCa_2Nb_3O_{10}$, KCN) was synthesized as described previously [67] and proton-exchanged in 6.5 M HNO_3 to produce $HCa_2Nb_3O_{10} \bullet 1.5H_2O$ (HCN). Aqueous stock suspensions of TBACN were prepared following an established protocol [67]. We add 1.0 g of HCN powder and 1.25 g of 40% w/w tetrabutylammonium hydroxide (TBAOH, Sigma-Aldrich) solution to 150 mL deionized (DI) water, followed by stirring at room temperature for a minimum of 7 days. The resulting suspension has a 1:1 molar ratio of TBA^+ to HCN unit cells and contains, based on our previous work [67], more than 95% exfoliated TBACN platelets.

2.2.1.2. PPA Grafting Protocol

In a typical grafting reaction, 25 mL of TBACN stock suspension was added to a 100 ml round-bottom flask and stirred, followed by addition of 0.27 g of phenylphosphonic acid (PPA, Sigma-Aldrich, used as received); this quantity represents a 3:1 molar ratio of PPA to CN unit cells. The mixture was then refluxed at a temperature near the solvent's boiling point, with stirring and slow N_2 bubbling, for 3 days. Reflux reactions were usually carried out under lighted conditions in a fume hood. The flask was located approximately 1 m below two standard, 32 W fluorescent bulbs (Phillips 700 series) behind a Plexiglas sheet. In some cases, reflux reactions were carried out in darkness with the lights off and the flask/condenser wrapped in aluminum foil. The products of grafting reactions prepared following this protocol are denoted as

14

PPA+TBACN(light) and PPA+TBACN(dark), with the terms in parentheses denoting variations in suspension and/or reflux conditions.

For TBACN, suspension conditions prior to PPA addition were also varied, including (1) additional dilution, or (2) drying followed by re-dispersion in a new solvent. For dilution cases, 25 mL of TBACN stock suspension was diluted with 25 mL of either DI water or TBAOH solution; these suspensions are denoted as TBACN(dil-DI) and TBACN(dil-TBA), respectively.

Experiments were also carried out in which 25 mL of the TBACN stock suspension was dried and then re-dispersed in 50 mL of a new solvent (DI water; TBAOH solution; 94-96% anhydrous, denatured ethanol, Alfa-Aesar; 99.5+% ethanol, Sigma-Aldrich; 99.5+% n-propanol, Alfa-Aesar; or n-propanol diluted with water to 95% n-propanol). The stock suspension was dried in the flask by heating in an oven at 90-100°C. After adding 50 mL of the new solvent, the suspension was ultrasonicated for 10 min (Solid-State/Ultrasonic FS-28, Fisher Scientific) and stirred for at least 1 h at room temperature. These suspensions are denoted, for example, as TBACN(dried, dil-DI) for the case of re-dispersion into DI water. The product of the grafting reaction for this suspension is denoted as PPA+TBACN(dried, dil-DI), with corresponding notation used for other solvents.

For reactions utilizing non-exfoliated HCN without TBA$^+$, the corresponding dry weight of HCN powder (0.30 g) was weighed into the flask, followed by addition of 50 mL of solvent (DI water, alcohols). The suspension was sonicated for 10 min and then stirred at room temperature for at least 1 h. Products of grafting reactions are denoted, for example as PPA+HCN(dil-DI).

15

After cooling to room temperature, the suspension was centrifuged at 6000 rpm for 1 h to recover the product. All products were washed twice with DI water (with mixing, sonication, and centrifugation) to remove unreacted PPA. The final products were dried overnight in an oven at 90-100°C.

2.2.2. Characterization Methods

Powder X-ray Diffraction (XRD) patterns were acquired using an X-ray diffractometer (Rigaku Ultima IV, Cu Kα radiation, λ = 1.5418 Å), typically over the 2θ range of 2-20° with a step size of 0.04° and a scan speed of 0.25°/min.

^{31}P *MAS NMR Spectroscopy.* Solid-state ^{31}P MAS NMR spectra were collected on either a Varian Inova 500 MHz or a Bruker Avance III-HD 500 MHz spectrometer (202.49 MHz). The Varian spectrometer used a Doty Scientific 4mm XC MAS probe. These spectra were collected at ambient temperature with a sample rotation rate of 10 kHz and TPPM decoupling at a ^1H field strength of 64 kHz. The Bruker system was fitted with a 1.9 mm MAS probe. These spectra were collected at ambient temperature with a sample rotation rate of 20 kHz. ^1H dipolar decoupling was performed with SPINAL64 modulation and 145 kHz field strength. Bloch decays were collected with 50 ms acquisition time over 300 or 400 ppm spectrum width with a relaxation delay of 10 s. Chemical shifts are reported with respect to H_3PO_4 and referenced externally with $NH_4 \cdot H_2PO_4$, which was assigned a value of 0.72 ppm.

Fourier Transform-Infrared (FT-IR) spectra were obtained utilizing a Perkin-Elmer Spectrum 100 FT-IR Spectrometer.

X-ray Photoelectron Spectroscopy (XPS) measurements utilized a Kratos AXIS Ultra DLD XPS system equipped with a monochromatic Al Kα source. The energy scale of the system is calibrated using an Au foil with Au4f scanned for the Al radiation and a Cu foil with Cu2p scanned for the Mg radiation resulting in a difference of 1081.70 ± 0.025 eV between these two peaks. The binding energy is calibrated using an Ag foil with $Ag3d_{5/2}$ set at 368.21 ± 0.025 eV for the monochromatic Al X-ray source. The monochromatic Al Kα source was operated at 15 keV and 120 W. The pass energy was typically fixed at 40 eV for the detailed scans. A charge neutralizer was used to compensate for the surface charge.

Thermogravimetric Analysis (TGA) (TA Instruments, model Q5000-0413) quantified the temperature-dependent mass loss of dried CN samples. Samples were placed on a Pt pan and heated in air from room temperature to 700°C with a 10°C/min ramp rate.

Dynamic Light Scattering (DLS) measurements employed a Zetasizer Nano ZS (ZEN3600, Malvern Instruments). Every DLS measurement was accompanied by a calibration test using 0.24 μm polystyrene latex microspheres (Bangs Laboratories, Inc.) as a sizing standard. Samples for DLS were diluted with specified solvent to a consistent concentration ($\sim 5 \times 10^{-5}$ g/mL, ~1 mL sample volume), sonicated for at least 10 minutes, mixed on a vortex mixer, and then characterized at 25°C. DLS theory for platelet-like particles is not well developed [86]. We use the quadratic cumulant method with the Stokes-Einstein equation to determine the effective spherical diameter of CN particles in suspension.

17

2.3. Results and Discussion

2.3.1. Characterization of HCN and TBACN

2.3.1.1. As-Prepared HCN and TBACN

Proton-exchanged CN (HCN) and TBA-exfoliated CN (TBACN) have physical characteristics similar to those previously reported [67]. Upon heating from room temperature to 150°C, HCN loses about 0.4% of its mass due to loss of residual moisture in the sample (Figure 2.1a). From 150°C to 700°C, HCN undergoes an additional 2.2% mass loss. Most of this loss (1.9%) occurs between 250°C and 350°C and is due to a dehydroxylation reaction producing calcium hexaniobate ($Ca_4Nb_6O_{19}$), as observed previously [87]. The (001) peak in the XRD pattern for HCN (Figure 2.1b) is located at $2\theta = 6.05°$, giving a d-spacing of 1.46 nm; the full pattern has been published previously [67].

After exfoliation with TBA^+ (1:1 TBA:CN molar ratio), the resulting TBACN forms a stable suspension of exfoliated platelets [67]. DLS measurements (Table 2.1) indicate an equivalent spherical diameter of 390 nm for TBACN particles in stock suspension, comparable to the 451 nm size reported previously [67]. Dilution of stock suspension into DI water, stirring for three days, and then further dilution with DI water does not lead to aggregation, since the particle diameter (365 nm) remains about that of the original suspension. After drying the stock suspension, TBACN particles readily re-disperse in aqueous TBA solution (D = 328 nm), but not in DI water (D = 650 nm).

TGA analysis of dried TBACN indicates a mass loss of 2.5% up to 150°C (assumed to be residual moisture), and a further loss of 11.6% from 150°C to 700°C. The peak rates of mass loss, around 250°C and 325°C, are associated with TBA^+

decomposition. After accounting for an estimated mass loss of 1.6% due to the dehydration reaction, the remaining TBA$^+$ mass loss leads to a 0.21 molar ratio of TBA$^+$ to CN unit cells. Repeated measurements give an average TBA:CN ratio of 0.18±0.03, consistent with previous reports [61]. XRD analysis of dried TBACN powder gives the expected XRD pattern [67] with the broad (001) peak indicating a d-spacing of 2.48 nm, consistent with turbostratic ordering of restacked TBA-coated CN platelets. The small secondary peak at 6° probably represents some non-exfoliated HCN.

Table 2.1. DLS results for TBACN suspensions (aqueous and alcoholic). The suspension concentrations were 5.0×10^{-5} g/mL for all DLS measurements.

Sample ID	Description	DLS Diluent (a)	Sphere Diam. (b) (nm)	Platelet Length (c) (nm)
As-prepared suspensions				
TBACN	As-prepared stock suspension, TBA+HCN	TBA/DI	390	540
TBACN(dil-DI)	TBACN diluted 1:1 (v/v) in DI, stirred for 3 days	DI	365	488
TBACN(dried, dil-DI)	TBACN dried, then re-dispersed in DI water	DI	650	1159
TBACN(dried, dil-TBA)	TBACN dried, then re-dispersed in TBA solution	TBA/DI	328	416
TBACN(dil-Et95)	TBACN diluted into 95% ethanol for DLS	Et95	352	462
TBACN(dried, dil-Et95)	TBACN dried, re-dispersed into 95% ethanol	Et95	474	723
TBACN(dried, dil-Et99)	TBACN dried, re-dispersed into 99% ethanol	Et99	897	1881
TBACN(dried, dil-nPr95)	TBACN dried, re-dispersed into 95% *n*-propanol	nPr95	509	805
TBACN(dried, dil-nPr99)	TBACN dried, re-dispersed into 99% *n*-propanol	nPr99	459	689
Refluxed suspensions				
TBACN(dil-DI, reflux)	TBACN diluted 1:1 in DI, refluxed 3 days in light	DI	398	556
TBACN(reflux)	TBACN refluxed 3 days in darkness	TBA/DI	400	560
PPA-grafted suspension				
PPA+TBACN	TBACN + 3:1 (molar) PPA, refluxed in light	TBA/DI	392	544

(a) Solvent used to dilute sample for DLS; abbreviations: DI = deionized water; TBA/DI = aqueous TBA solution; Et95 = 95% ethanol (balance water); Et99 = 99% ethanol (balance water); nPr95 = 95% *n*-propanol (balance water); nPr99 = 99% *n*-propanol (balance water).
(b) Intensity-mean equivalent spherical diameter.
(c) Average platelet length based on Eqn. (3) in ref. [86].
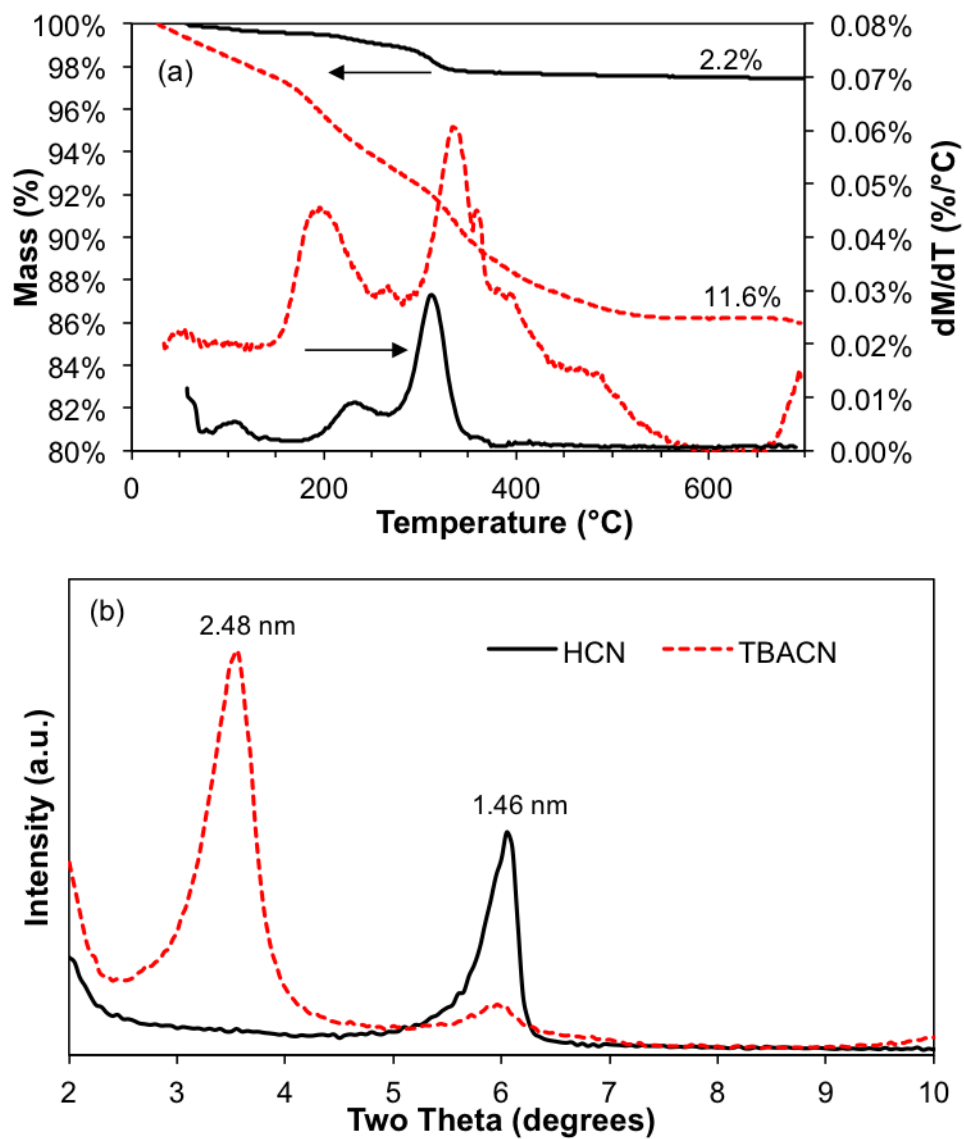
Figure 2.1. Characterization of as-prepared HCN (solid curves) and TBACN (dashed curves): (a) mass (%) and its derivative as functions of temperature from TGA, and (b) XRD patterns over the low-angle range. Numbers in (a) indicate "total" (non-water) percentage mass decreases from 150°C to 700°C.

TBACN suspensions were refluxed in darkness and under fluorescent lights as control experiments for the PPA grafting experiments discussed in section 2.3.2. For TBACN refluxed in darkness, the dried product exhibits a 9.1% mass loss from 150°C to 700°C (Figure 2.2a), slightly less than that found for the starting stock suspension. The derivative mass loss pattern is also similar to that of the starting TBACN stock suspension (Figure 2.1a). Most of the mass loss occurs between 150 and 350°C, presumably due to TBA^+ oxidation and fragmentation. Additional mass loss up to 550°C probably occurs due to oxidation of the residual carbonaceous char (see Figure 2.1a). XRD results (Figure 2.2b) show that TBACN refluxed in darkness has a d-spacing of 2.66 nm, close to that of starting TBACN (2.48 nm). These results indicate that refluxing TBACN in darkness does not have much of an effect on the state of the TBACN platelets.

In contrast, the product of refluxing TBACN suspension in the light exhibits a 5.2% mass loss between 150°C and 700°C (Figure 2.2a), less than half that of the starting stock suspension. The derivative mass loss pattern differs from that of the stock suspension as well; the peak rate of mass loss occurs at 250°C. The d-spacing of TBACN refluxed in light decreases from 2.48 nm to 1.52 nm (Figure 2.2b). These results indicate that HCN may catalyze the degradation of TBA^+ in the presence of light at elevated temperatures. This should not be surprising, given the well-established photocatalytic properties of HCN and other layered perovskites [68-85].
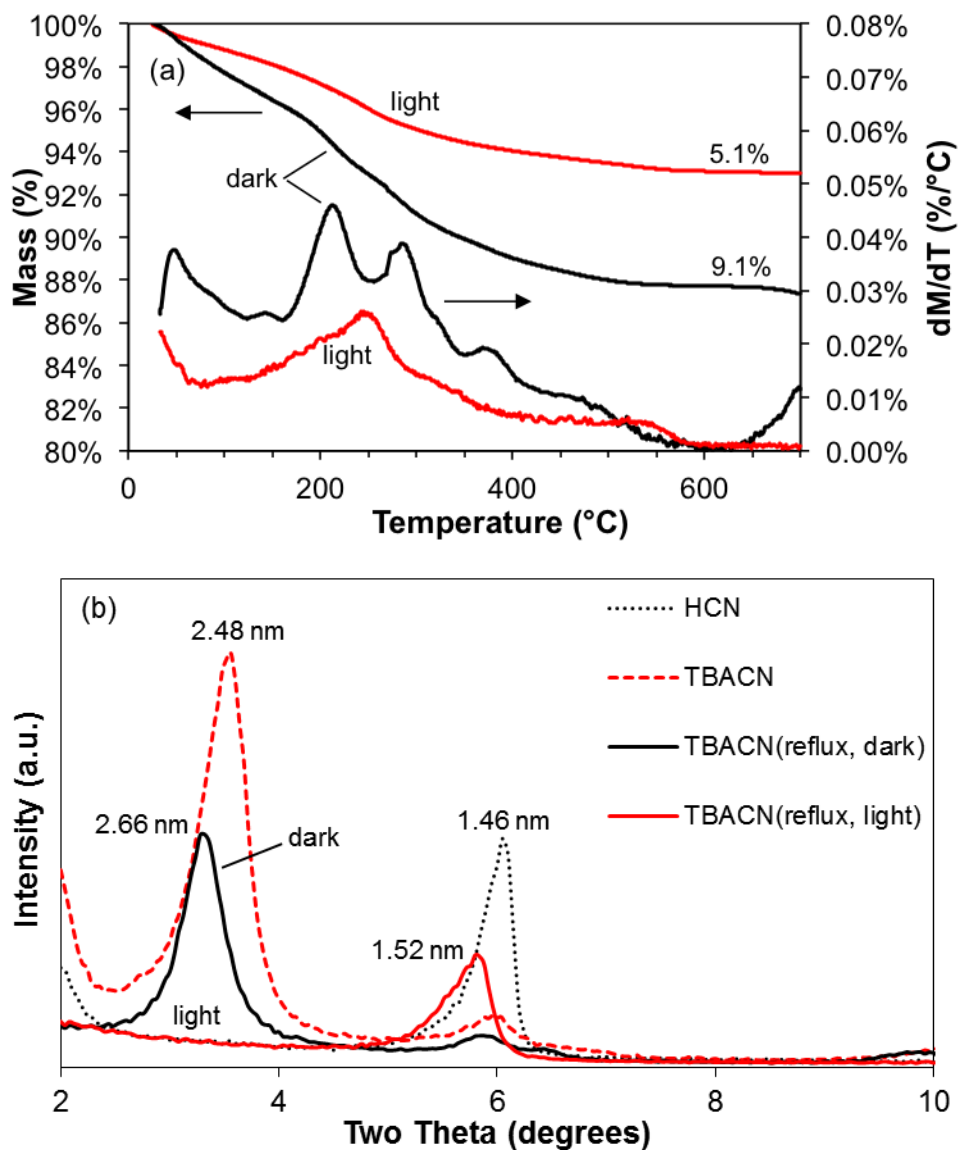
Figure 2.2. Characterization of TBACN refluxed in light (solid red curves, "light") and in darkness (solid black curves, "dark"): (a) mass (%) and its derivative as functions of temperature from TGA, and (b) XRD patterns over the low-angle range. Panel (b) also includes patterns for as-prepared HCN (dotted black curve) and TBACN stock suspension (dashed red curve). Numbers in (a) indicate "total" (non-water) percentage mass decreases from 150°C to 700°C.

TGA and XRD provide useful information on the effect of sample processing conditions on the state of TBACN. Figure 2.3 summarizes TGA mass loss results for TBACN suspensions subjected to various processing conditions and refluxed under lighted conditions. As-prepared HCN does not contain TBA^+, so it exhibits only a small mass loss due to dehydroxylation. For TBACN diluted 1:1 (v/v) with DI water, stirred, but not refluxed (Figure 2.3, "TBACN(dil-DI, stir)"), the mass loss values over 150-350°C and 150-700°C are about 15% less than those of the TBACN stock suspension. This suggests that dilution into DI water may result in desorption of some weakly bound TBA^+ from the HCN platelets.

The last three samples in Figure 2.3 are TBACN stock suspensions diluted and refluxed under lighted conditions. The mass loss values for TBACN diluted 1:1 into DI water and refluxed [TBACN(dil-DI, reflux)] are 30% lower than those for TBACN stock suspension. This might be explained by a combination of TBA^+ desorption and photocatalytic-degradation. The mass loss values are even lower if TBACN is dried before re-dispersion into DI water and refluxed [TBACN(dried, dil-DI, reflux)]. DLS results (Table 2.1) indicate that after drying, TBACN platelets do not fully re-disperse in DI water. While not necessarily favoring TBA^+ desorption, the local environment in TBACN aggregates may be more favorable for photo-degradation. Finally, TBACN diluted 1:1 into TBA solution and refluxed [TBACN(dil-TBA, reflux)] has the lowest mass loss values (about 60% less than TBACN stock suspension). This sample thus had the lowest final TBA content, despite the excess TBA^+ initially present. This may be explained by active TBA^+ photo-degradation catalyzed by HCN.
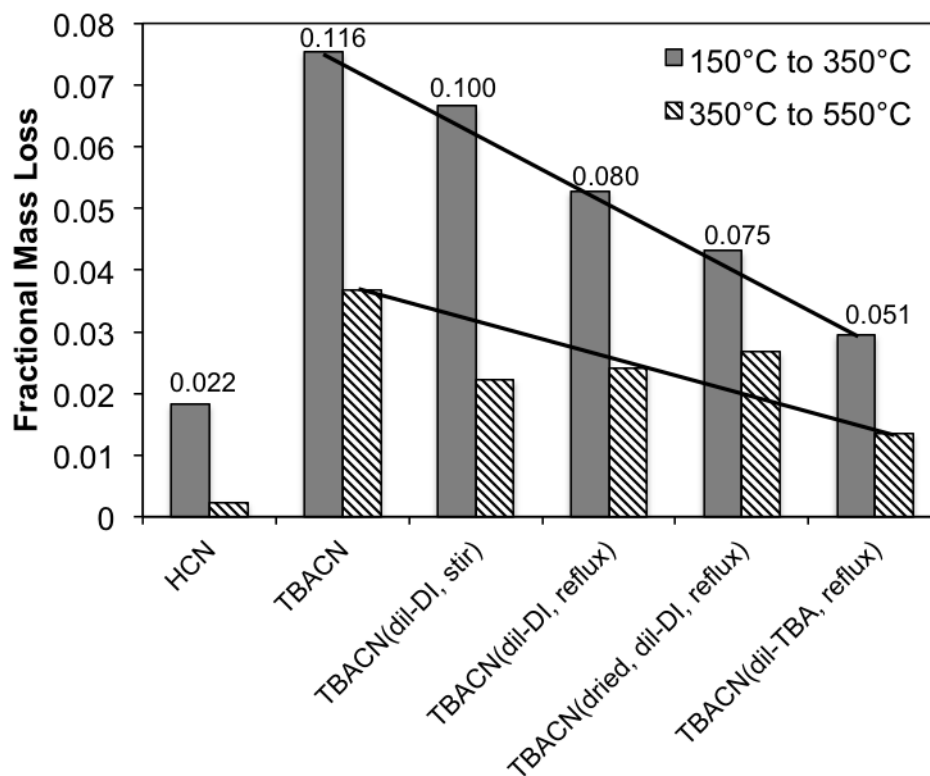
Figure 2.3. Fractional mass losses measured by TGA for as-prepared HCN and TBACN subjected to various processing conditions: as-prepared stock suspension (TBACN); TBACN diluted 1:1 with DI water and stirred [TBACN(dil-DI, stir)]; TBACN diluted 1:1 with DI water and refluxed [TBACN(dil-DI, reflux)]; TBACN dried, re-dispersed in DI water, and refluxed [TBACN(dried, dil-DI, reflux)]; and TBACN diluted 1:1 with TBA solution and refluxed [TBACN(dil-TBA, reflux)]. The starting suspensions all had the same TBACN wt%, and were refluxed in light. Numbers above each pair of bars denote the total fractional mass loss from 150 to 700°C. Trend lines are drawn to guide the eye.

XRD characterization (Figure 2.4) generally supports the TGA analysis. TBACN suspension diluted 1:1 in DI water and only stirred [TBACN(dil-DI, stir)] has an XRD pattern (after drying) like that of undiluted TBACN suspension (Figure 2.1b). The (001) peak gives a d-spacing of 2.57 nm, consistent with restacking of TBA-covered CN platelets. A small peak at 1.52 nm indicates the presence of some non-exfoliated HCN. TBACN suspension diluted 1:1 in DI water and refluxed [TBACN(dil-DI, reflux)] has a similar XRD pattern (primary d-spacing of 2.66 nm), but with a larger secondary peak near 6° (1.48 nm). In this case, desorption and/or degradation of some TBA may have caused restacking of some HCN platelets with less (or no) TBA$^+$ in the interlayer spaces. For the TBACN suspension that was first dried, re-dispersed in DI water, and refluxed [TBACN(dried, dil-DI, reflux)], the XRD pattern does not show strong Bragg reflections, indicating disorder in the dried product. Magnification shows that there is a peak near 5.8° (d-spacing 1.55 nm) that could be some non-exfoliated or restacked, bare HCN. The main observation is the near absence of a (001) peak near 3.4° associated with restacked, TBA-coated CN platelets, consistent with desorption and photo-degradation of the TBA$^+$. Lastly, the pattern for TBACN suspension diluted 1:1 in TBA solution and refluxed [TBACN(dil-TBA, reflux)] also has no 3.4° (001) peak, but it does have a prominent peak near 6° (1.48 nm). This is consistent with considerable photo-degradation of the TBA$^+$, followed by platelet restacking during the drying of the product.
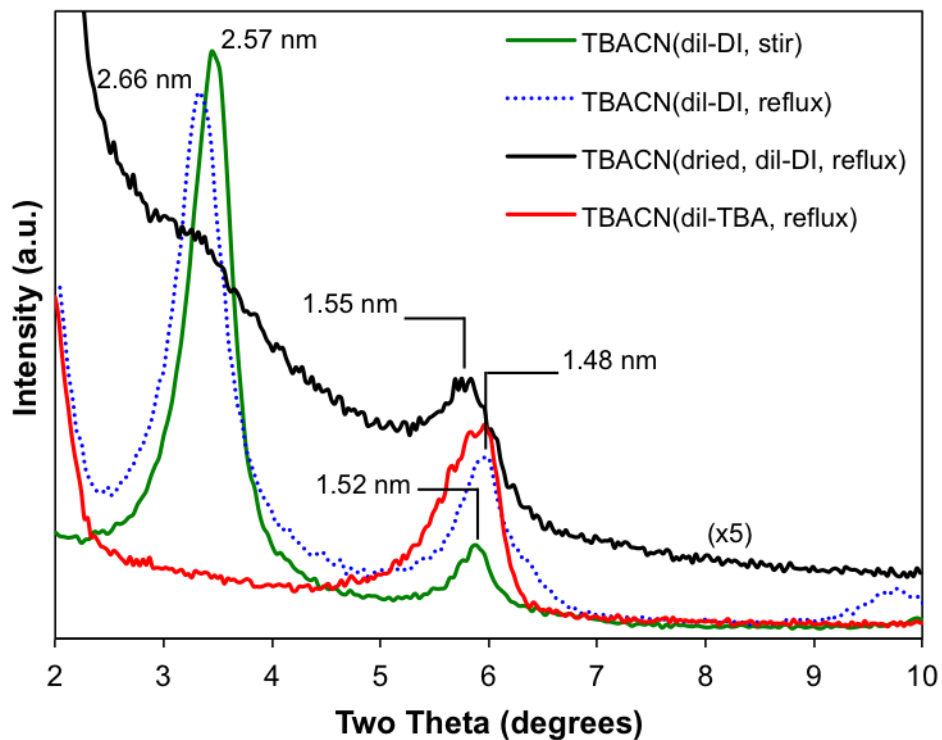
Figure 2.4. XRD patterns of TBACN subjected to various processing conditions: TBACN diluted 1:1 with DI water and stirred [TBACN(dil-DI, stir)]; TBACN diluted 1:1 with DI water and refluxed [TBACN(dil-DI, reflux)]; TBACN dried, re-dispersed in DI water, and refluxed [TBACN(dried, dil-DI, reflux)]; and TBACN diluted 1:1 with TBA solution and refluxed [TBACN(dil-TBA, reflux)]. The starting suspensions all had the same TBACN wt% and were refluxed in light.

2.3.2. PPA Grafting in HCN and TBACN Aqueous Suspensions

2.3.2.1. Evidence for PPA Grafting and Grafted Amounts

We now consider covalent modification of HCN and TBACN using phenylphosphonic acid (PPA). As in previous studies of organophosphonic acid grafting [22-24, 29, 32, 36, 58, 88, 89], ^{31}P MAS NMR (Figure 2.5) provides direct evidence for PPA grafting onto calcium niobate. The NMR spectrum for pure PPA (Figure 2.5a) has a signature peak at 21.4 ppm. The other spectra in Figure 2.5 are for the washed, dried products of refluxed HCN or TBACN suspensions with added PPA. In all cases, the spectra show broad, sometimes multimodal peaks shifted 4-17 ppm upfield relative to the peak for pure PPA. The peak locations for the reflux products (centered at around 11-13 ppm) are consistent with previous reports for PPA grafting onto titania [23] and layered lanthanum hexaniobate [58]. None of the product spectra in Figure 2.5 have peaks at 21.4 ppm indicative of free, non-grafted PPA. These spectra show that PPA readily grafts onto HCN and TBACN platelets. The apparent presence of multiple, overlapping peaks suggests different PPA grafting modes, which will be discussed in section 2.3.2.4.
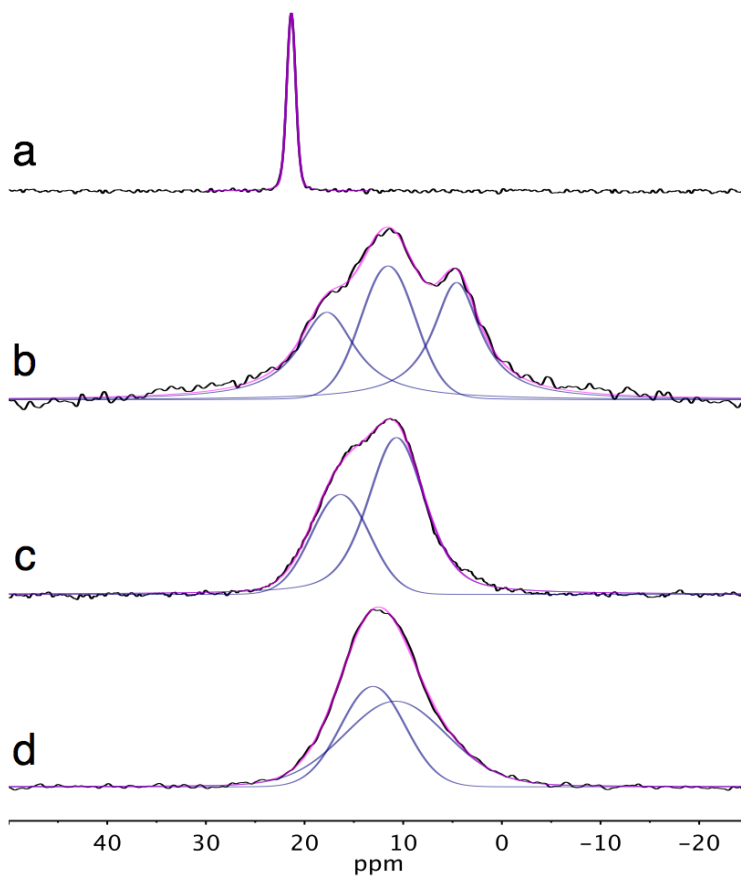
Figure 2.5. ^{31}P MAS NMR spectra with peak fitting for: (a) pure PPA, (b) PPA+HCN refluxed in DI water and in light, (c) PPA+TBACN refluxed in light, and (d) PPA+TBACN refluxed in darkness. PPA was added to CN in a 3:1 molar ratio.

XRD patterns for the washed, dried products (Figure 2.6) provide evidence about the location of PPA grafting. The pattern for PPA refluxed in DI water with non-exfoliated HCN has one peak at 6.05° (d-spacing 1.46 nm), essentially the same as that of the as-prepared HCN (Figure 2.1b). This shows that PPA does not penetrate HCN's interlayer space, but instead grafts solely on the exterior of the non-exfoliated HCN particles. The patterns for PPA added to TBACN suspension and refluxed (in light or in darkness) have distinct, broad peaks centered near 4.2° with d-spacings in the 2.1-2.2 nm

range, in between the d-spacings of as-prepared HCN (1.46 nm) and TBACN stock suspension (2.48 nm). These patterns also have smaller peaks at 5.84° (1.51 nm), but no evidence of a peak at 3.56° (2.48 nm) consistent with the starting TBACN; this shows that PPA grafting at least partially displaces adsorbed TBA[+].

Taken together, the NMR and XRD data show that PPA has been grafted onto the face surfaces of the exfoliated TBACN platelets. Upon drying, these "PPA+TBACN" platelets restack with turbostratic order with an average interlayer gap width expanded by about 0.7 nm relative to HCN (for PPA+TBACN prepared in the light, 2.17 - 1.46 nm = 0.71 nm). This expansion is consistent with that reported previously for interlayer grafting of PPA on layered double hydroxides [36, 38], interpreted in terms of a bilayer of grafted PPA molecules with tilted orientation. Alternately, the 0.71 nm expansion approximately equals the length of a PPA molecule [37, 58, 90-93], possibly consistent with an "interdigitated" bilayer of grafted PPA molecules oriented normal to the surface [32]. Although these pictures of the interlayer structure are speculative, the NMR and XRD data provide clear evidence that PPA has been grafted onto the face surfaces of the exfoliated TBACN platelets. We are not aware of any previous reports of covalent grafting onto any kind of exfoliated niobate platelets.

Previous studies suggest the possibility of side reactions between PPA and TBACN to form small quantities of layered calcium or niobium phenylphosphonate (CaPPA, NbPPA). Reports of the synthesis of layered CaPPA [94, 95] provide XRD patterns and ^{31}P NMR spectra. The XRD pattern for CaPPA [95] has three distinct peaks (at about 5.7°, 11.5°, and 17.4°) that are difficult to distinguish from those of residual unexfoliated HCN. The ^{31}P NMR spectrum of hydrated CaPPA [95] has two peaks: one

at 20.0 ppm is not seen in the product spectra in Figure 2.5, and the other at 12.4 ppm overlaps with those seen in Figure 2.5. Thus the quantity of CaPPA produced in the grafting reactions carried out in this work is likely to be small or nonexistent. The synthesis of NbPPA has not been reported in the literature. We have recently synthesized NbPPA via a melt process, to be reported in a future publication. The peaks in the XRD pattern attributable to NbPPA do not match the peaks in XRD patterns for our products, so we can rule out the presence of NbPPA as a byproduct.
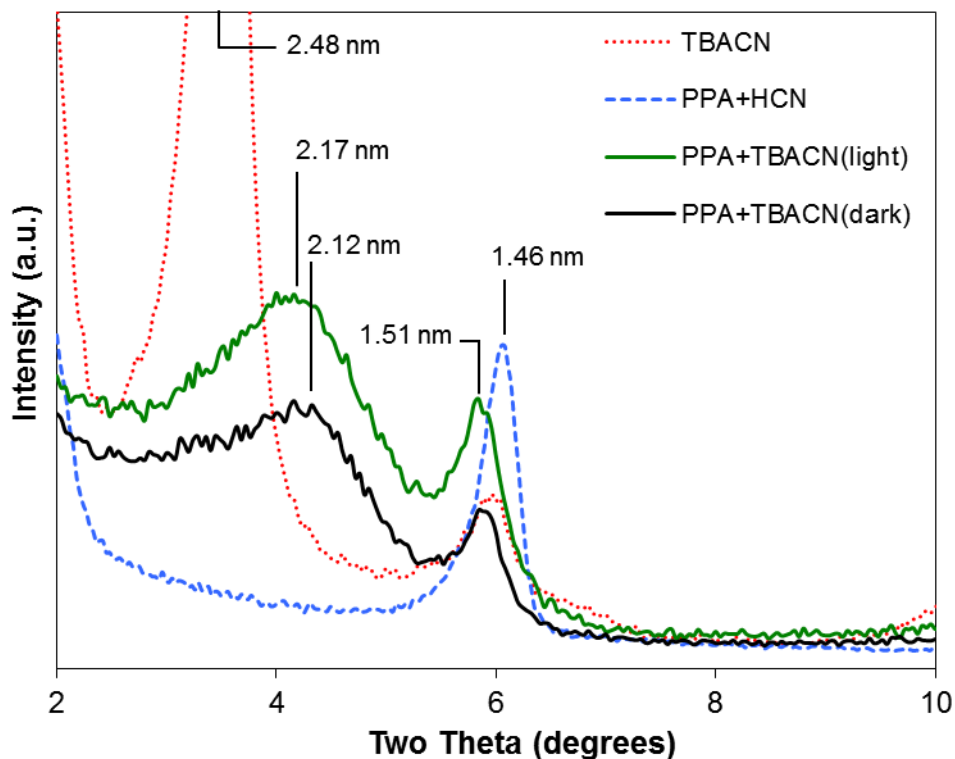
Figure 2.6. XRD patterns for: TBACN; PPA+HCN refluxed in DI water and in light; PPA+TBACN refluxed in light; and PPA+TBACN refluxed in darkness.

The XRD patterns in Figure 2.6 imply that PPA grafting removes at least some of the adsorbed TBA^+ from the surfaces of the PPA+TBACN products, as evidenced by the absence of peaks at 3.56°. TBA^+ could be eliminated by photocatalytic-degradation or physical displacement from the HCN surface by grafted PPA. FT-IR spectra (Figure 2.7) provide additional insight. The FT-IR spectrum for TBACN shows strong bands at 2961, 2933, and 2874 cm^{-1} associated with CH_3 stretching and symmetric and asymmetric CH_2 stretching vibrations, respectively [96-98]. However, these bands are much weaker in the PPA+TBACN products. The same is true for CH_3 and CH_2 bending vibrations in the 1500-1370 cm^{-1} region (see section 2.3.2.4) [96, 98]. These observations indicate that the amounts of residual TBA^+ in the PPA+TBACN products are relatively small.
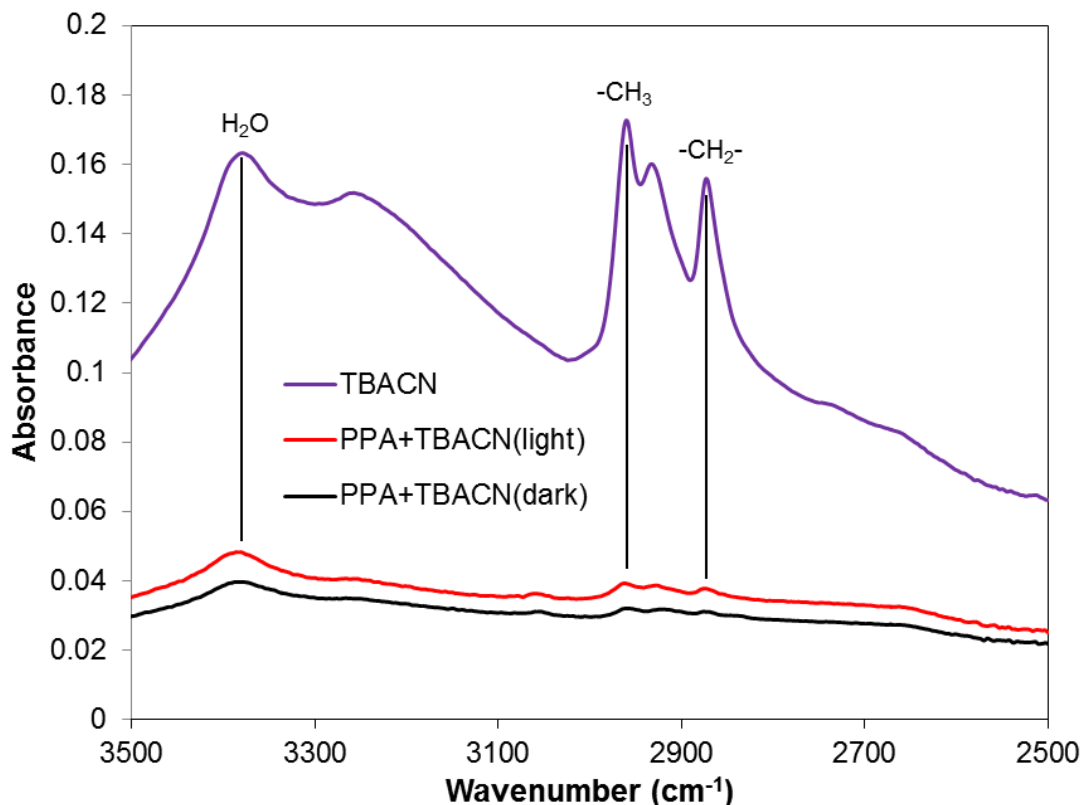
Figure 2.7. FT-IR spectra in the 3500-2500 cm^{-1} range for: TBACN; PPA+TBACN refluxed in light; and PPA+TBACN refluxed in darkness.

32

The TGA mass loss and derivative mass loss curves (Figure 2.8) also provide additional information. The mass loss curves (Figure 2.8a) appear to be shifted vertically relative to each other, mainly due to differences in water loss below 150°C. Between 150 and 350°C, the PPA+HCN product loses 2.0 wt%, almost equal to that of as-prepared HCN (1.8 wt%, Figure 2.1a); the peaks in the derivative mass loss (i.e., mass loss rate, Figures 2.1a and 2.8b) are similar, as well. This implies that the 150-350°C mass loss for PPA+HCN is due to CN dehydroxylation. The PPA+HCN product loses 4.2 wt% from 350 to 550°C (Figure 2.8a) and has a distinct peak in the mass loss rate curve at 500°C (Figure 2.8b). As-prepared HCN loses almost no mass (0.2 wt%, Figure 2.3) over the same temperature range. From this, we infer that the decomposition of PPA in PPA+HCN occurs only in the 350-550°C temperature range, consistent with previous reports for PPA decomposition after grafting onto other metal oxides [24, 37].
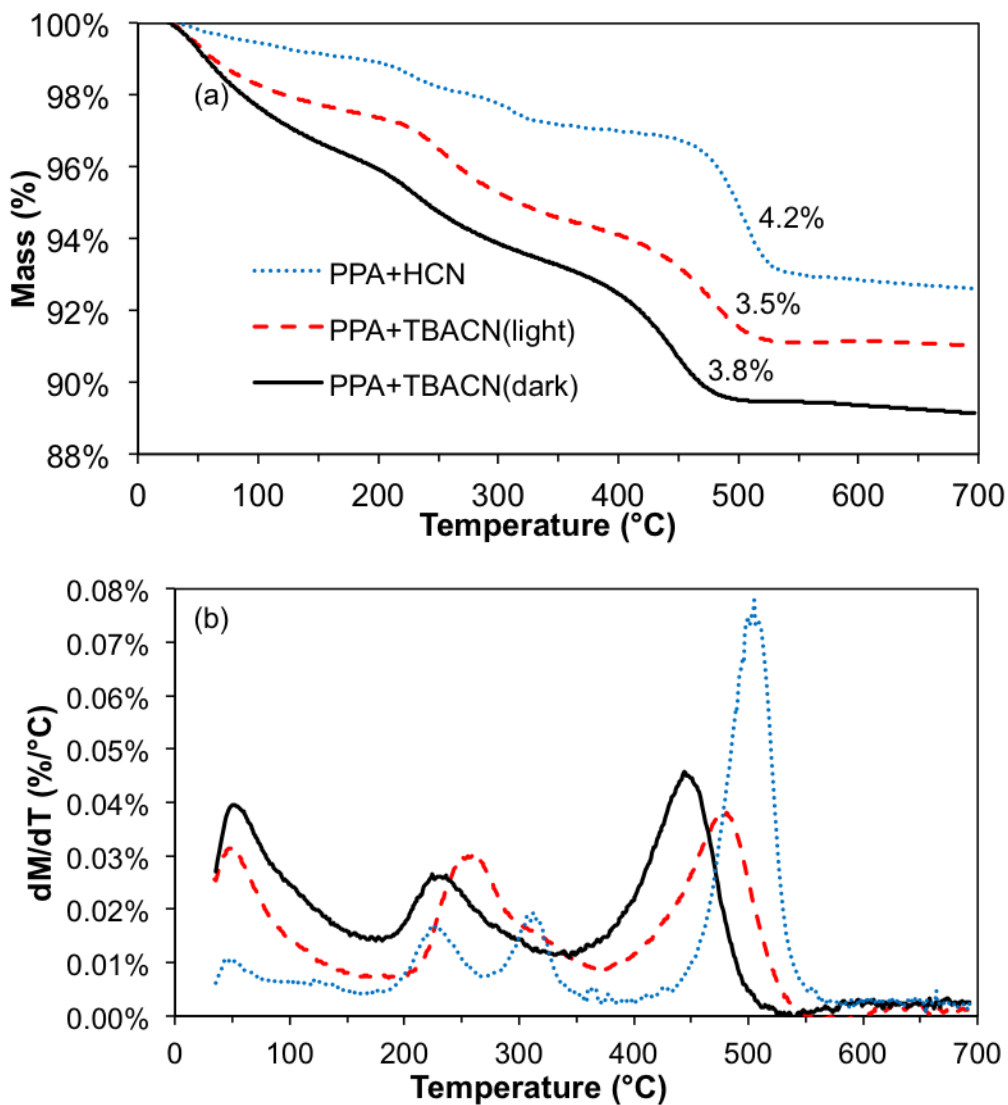
Figure 2.8. TGA characterization of mass percentage (a) and its derivative (b) as functions of temperature for: PPA+HCN refluxed in DI water and in light; PPA+TBACN refluxed in light; and PPA+TBACN refluxed in darkness. Numbers in (a) indicate percentage mass decreases from 350°C to 550°C.

The derivative mass loss patterns for the PPA+TBACN products in the 150-350°C range (Figure 2.8b) are similar to that of TBACN suspension refluxed in light (Figure 2.2a). Presumably, these mass losses are associated with residual TBA$^+$. The PPA+TBACN products lose significant additional mass in the 350-550°C range (Figure 2.8a) with distinct acceleration between 425 and 500°C (Figure 2.8b), again consistent with PPA decomposition in oxidizing environments [24, 37]. Figure 2.9 quantifies the TGA mass losses over the key temperature ranges. Both of the PPA+TBACN(light, dark) products have significantly larger losses in the 350-550°C range than the corresponding refluxed TBACN stock suspensions (Figure 2.9). The additional mass losses must be due to the decomposition of grafted PPA.

For refluxed TBACN suspensions (Figure 2.9), most of the mass loss occurs over 150-350°C, but TBA$^+$ decomposition continues through the 350-550°C range. Thus, we cannot assume that the 350-550°C mass losses are entirely due to PPA decomposition for the PPA+TBACN products.
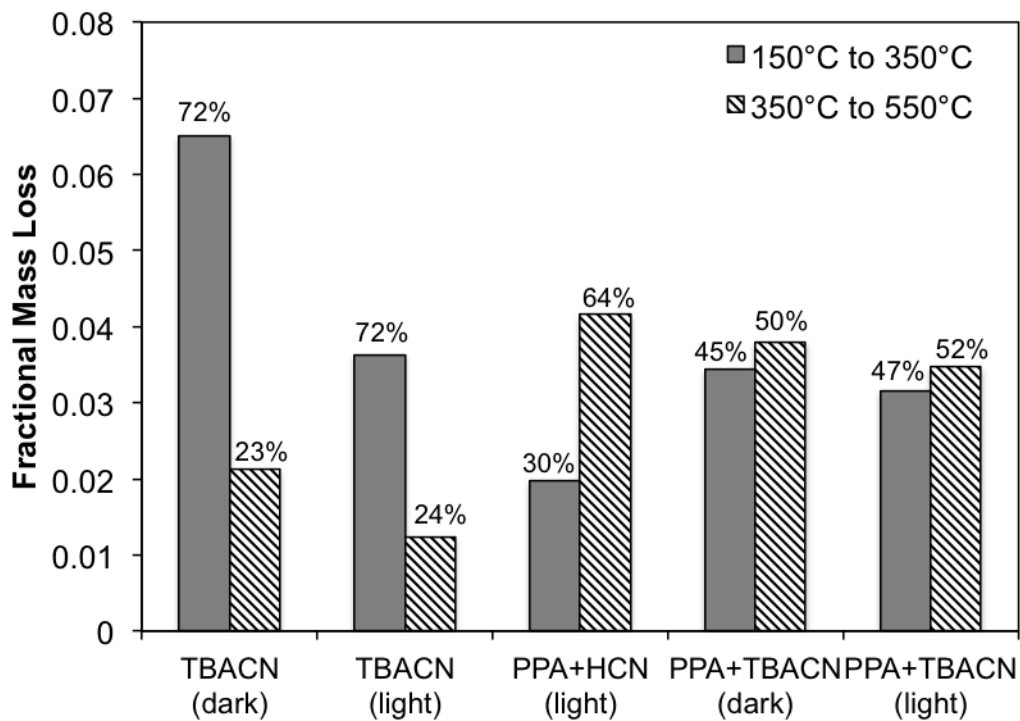
Figure 2.9. Fractional TGA mass losses for various products after refluxing (in darkness or in light, as indicated in the category label): as-prepared TBACN stock suspension (TBACN); PPA added to aqueous, non-exfoliated HCN (PPA+HCN); and PPA added to TBACN stock suspension (PPA+TBACN). The number above each bar denotes its percentage of the total fractional mass loss from 150 to 700°C.

TGA-based estimates of PPA grafted amounts are also complicated by uncertainty in the stoichiometry of PPA oxidation during TGA. For the TGA residue from PPA+TBACN refluxed in light, ^{31}P MAS NMR and FT-IR results (Figures 2.10 and 2.11) indicate the presence of free $(PO_4)^{3-}$ and $(HPO_4)^{2-}$, perhaps as $Ca_3(PO_4)_2$ and $CaHPO_4$. Thus, during TGA in air, PPA loses its phenyl ring but gains oxygen atoms as it is oxidized to phosphates, which may have complex stoichiometry [99, 100]. This makes it difficult to estimate the moles of PPA from the net mass loss without additional data or making strong assumptions.

36
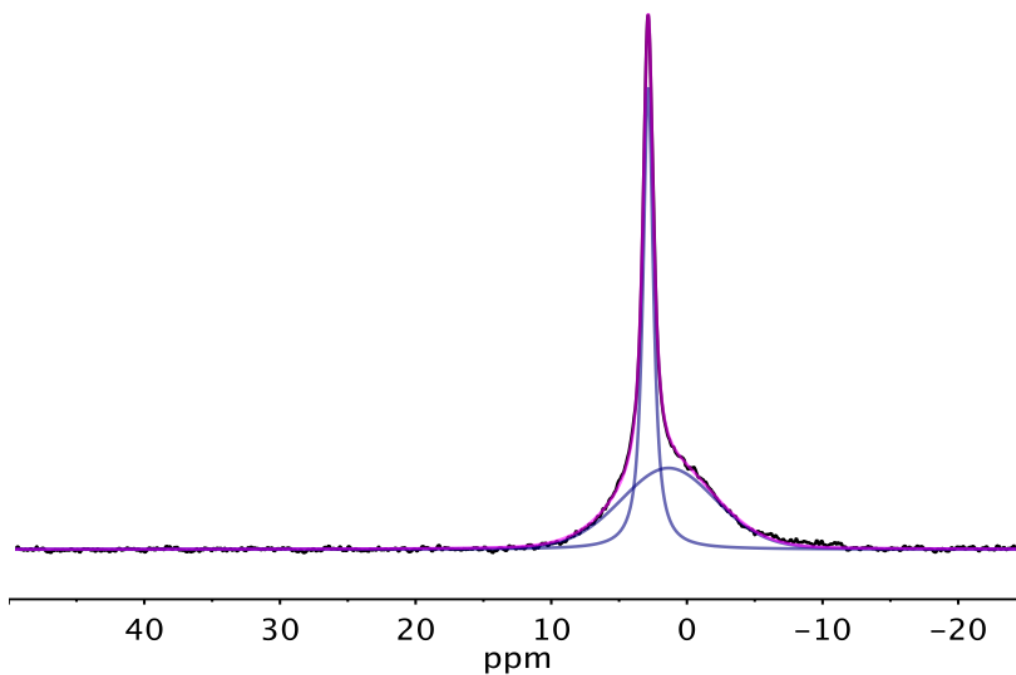
Figure 2.10. ^{31}P MAS NMR spectrum for PPA+TBACN, refluxed in DI water and in light, and then heated at 700°C in air for 12 h. Deconvolution gives a sharp primary peak at 2.74 ppm, and a weaker, broad secondary peak centered at 1.22 ppm. The primary peak agrees with that of $Ca_3(PO_4)_2$, as reported previously [101]. The secondary peak may represent protonated phosphate [102], perhaps as $CaHPO_4$.
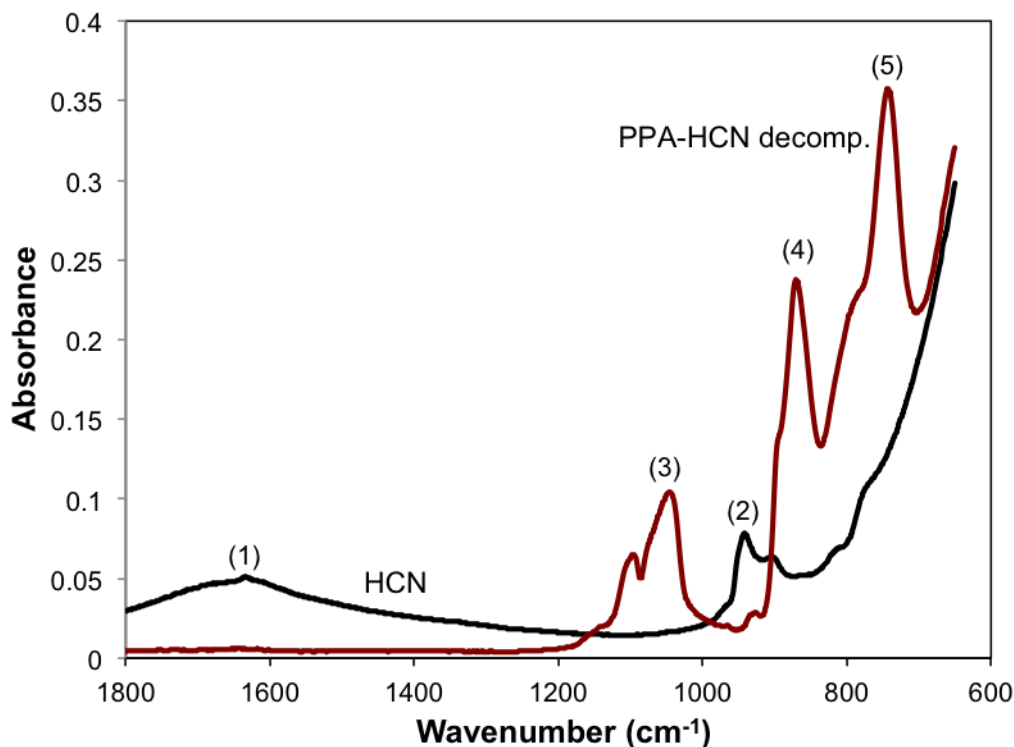
Figure 2.11. FT-IR spectrum for PPA+TBACN, refluxed in DI water and in light, and then heated at 700°C in air for 12 h ("PPA-HCN decomp."). The figure also shows the spectrum for the starting material, protonated calcium niobate (HCN). Peak assignments for HCN: peak (1) at 1635 cm^{-1} is H-O-H bending; and the peak/shoulder (2) at 942 and 904 cm^{-1} are Nb-O$_{terminal}$ stretching vibrations [103]. Peak assignments for PPA-HCN decomp.: peaks (3) centered at 1046 and 1096 cm^{-1} are vibrations of PO$_4^{3-}$; peak (4) may be HPO$_4^{2-}$ [99, 100]; peak (5) is as yet unidentified; speculating, it could be a Nb-O-P vibration.

PPA grafted amounts can be estimated from XPS results (Table 2.2). For as-prepared HCN and TBACN stock suspension, the O:Nb ratios are close to the expected value of 3.33 (10:3). The Nb:Ca ratios for HCN (2.73) and TBACN (1.75) are higher than the expected value of 1.5, perhaps due to shielding of the Ca atoms within the CN structure.

XPS also provides the molar percentage of P atoms in samples with added PPA; each HCN unit cell contains 3 Nb atoms, so 3(P:Nb) gives the PPA:CN molar ratio. The

maximum possible PPA:CN ratio is 2, assuming one reactive apical oxygen on each face surface of the CN unit cell and monodentate PPA grafting. The maximum "practical" ratio may be less than 2 due to steric hindrance, since the reported 0.24 nm^2 parking area for a phosphonate graft [20, 22, 23, 58, 104] is greater than the 0.148 nm^2 area of one CN unit cell [105]. Based solely on steric considerations, the maximum PPA:CN ratio may be as little as 1.23 (=2×0.148/0.24). PPA grafting via bi- or tridentate binding modes (discussed below in section 2.3.2.4) might further reduce the PPA:CN ratio.

For PPA+TBACN suspensions refluxed in light or in darkness, the measured PPA:CN ratios are both just over 0.5 (Table 2.2). This represents a graft density of about 1.70/nm^2 [=0.5/(2×0.148)], which is less than the 4.8/nm^2 reported for PPA grafting on TiO_2 [23]. In addition to the factors mentioned above, PPA must displace adsorbed TBA^+ in order to graft onto the CN surface, which probably hinders grafting. PPA's acidic protons probably assist by exchanging for TBA^+, but ion exchange, and thus displacement, do not appear to be complete. For PPA grafted onto unexfoliated HCN particles, XPS yields a higher PPA:CN ratio, 0.785, equivalent to a graft density of 2.65/nm^2. In this case, PPA does not compete with TBA^+ for space on the surface. The PPA:CN ratio may be underestimated in this sample because PPA grafts only on the exterior surface of the HCN particles, while the XPS X-rays may penetrate multiple CN layers.

Table 2.2. XPS results for elemental compositions and PPA:CN ratios of PPA+CN products.

Sample ID	Composition (mol%)				PPA:CN Molar Ratio Based on P:Nb	PPA Graft Density (1/nm^2)
	P	Ca	Nb	O		
HCN (HCa$_2$Nb$_3$O$_{10}\bullet$1.5H$_2$O)	0.00	5.76	15.7	52.2	0	n.a.
TBACN	0.00	8.40	14.7	49.1	0	n.a.
PPA+HCN(light)	3.01	3.71	11.5	42.8	0.785	2.65
PPA+TBACN(light)	2.28	7.94	13.6	47.0	0.504	1.70
PPA+TBACN(dark)	2.47	7.72	13.1	46.4	0.566	1.91
PPA+TBACN(dil-DI)	1.64	7.69	14.1	50.5	0.349	1.18
PPA+TBACN(dried, dil-DI)	1.59	7.60	14.3	48.3	0.333	1.13
PPA+TBACN(dried, dil-TBA)	1.10	7.99	14.0	50.5	0.235	0.79
PPA+HCN(dil-Et95)	0.76	5.12	14.1	45.1	0.162	0.55 (a)
PPA+HCN(dil-nPr99)	1.09	4.87	13.4	43.8	0.245	0.83 (a)
PPA+TBACN(dried, dil-Et95)	0.70	8.71	15.3	50.7	0.138	0.47
PPA+TBACN(dried, dil-Et99)	0.38	8.57	15.7	52.1	0.073	0.25
PPA+TBACN(dried, dil-nPr95)	0.49	8.99	15.5	51.6	0.095	0.32
PPA+TBACN(dried, dil-nPr99)	0.71	8.67	15.0	51.2	0.142	0.48

(a) Values reported for consistency; NMR, FT-IR, and TGA data support the conclusion that little or no PPA grafts onto unexfoliated HCN in alcoholic suspensions. See section 2.3.3.

2.3.2.2. *Influence of Light on PPA Grafting*

TGA and XRD results presented in Figures 2.2-2.4 demonstrate that adsorbed TBA$^+$ cations undergo at least partial degradation when TBACN suspensions are exposed to light, attributed to photocatalytic activity of the layered calcium niobate perovskite. Does exposure to light affect PPA grafting on TBACN? XRD patterns (Figure 2.6), FT-IR spectra (Figure 2.7 and, presented later, Figure 2.16), and TGA data (Figures 2.8 and 2.9) do not reveal significant differences between the product of PPA+TBACN refluxed in light versus that refluxed in darkness. XPS results (Table 2.2) indicate that the PPA:CN molar ratio for PPA+TBACN(dark) is 12% higher than that for PPA+TBACN(light). For PPA+TBACN(dark), the TGA mass loss in the 350-550°C temperature range (Figure 2.8a) is about 9% higher than that for PPA+TBACN(light).

This may seem counterintuitive, since photo-degradation of TBA$^+$ should open up space on the TBACN surface for additional PPA grafting.

However, the ^{31}P MAS NMR spectra (Figure 2.5c and d) provide evidence that some grafted PPA may undergo TBACN-catalyzed photo-degradation, which accounts for the lower PPA grafted amount in PPA+TBACN refluxed in light. The upfield shift of the peak in Figure 2.5d suggests that for PPA+TBACN refluxed in darkness, PPA grafts primarily in a bidentate grafting mode (deconvolution into two peaks may not be justified). The same probably occurs in PPA+TBACN refluxed in light. However, for PPA+TBACN(light), prolonged light exposure (3 days) under acidic, aqueous reflux conditions may result in some PPA photo-degradation, accompanied by reversion of a fraction of bidentate grafts to monodentate form. This rationalizes the two separate deconvoluted peaks (with upfield shifts corresponding to a mixture of mono- and bidentate grafts) observed in the NMR spectrum (Figure 2.5c) for PPA+TBACN(light). PPA grafting modes are discussed more thoroughly in section 2.3.2.4.

2.3.2.3. *Effect of Suspension Processing Conditions on PPA Grafting*

This section explores the effect of suspension processing steps, such as dilution or drying and re-dispersion, on PPA grafting onto TBACN platelets. Figure 2.12 displays ^{31}P MAS NMR spectra for washed, dried PPA+TBACN products made from TBACN suspensions processed in different ways. Each spectrum has a dominant monomodal peak centered at just above 11 ppm. This upfield shift of about 10.4 ppm (relative to PPA's peak at 21.4 ppm, Figure 2.5a) shows that PPA has been grafted onto TBACN. The PPA signature peak does not appear in Figure 2.12, indicating the absence of non-

grafted PPA. These results demonstrate that PPA grafting occurs in TBACN suspensions diluted into DI water or dried and re-dispersed in DI water or TBA solution.

XPS and XRD results (Table 2.2, Figure 2.13) indicate that the location and amount of PPA grafting are affected by suspension processing conditions. For TBACN stock suspension diluted 1:1 into DI water [TBACN(dil-DI)], DLS (Table 2.1) shows that the TBACN platelets are well dispersed, if not fully exfoliated [67]. Thus, PPA has access to all of the CN platelet surfaces in this case. After PPA grafting, the product [PPA+TBACN(dil-DI)] has a PPA:CN ratio of 0.349 (Table 2.2), indicating less PPA grafting than in the PPA+TBACN(light, dark) products discussed earlier. The PPA concentration in PPA+TBACN(dil-DI) is only half that in the PPA+TBACN(light, dark) cases. This reduces the driving force for PPA grafting, resulting in the lower PPA:CN ratio. The XRD pattern for the PPA+TBACN(dil-DI) product (Figure 2.13) has a relatively broad peak centered near 5.1°. The peak shape suggests weak turbostratic ordering with considerable polydispersity of interlayer spacing centered at 1.72 nm. The product (after drying) has a d-spacing less than that of PPA+TBACN(light, dark) (2.12-2.17 nm, Figure 2.6), also consistent with the lower PPA grafted amount.

For TBACN suspension that is first dried and then re-dispersed/diluted in DI water [TBACN(dried, dil-DI)], DLS (Table 2.1) shows that TBACN platelets do not fully re-disperse, but remain partially aggregated. After PPA grafting, the PPA+TBACN(dried, dil-DI) product has a PPA:CN ratio of 0.333 (Table 2.2), comparable to that of the PPA+TBACN(dil-DI) product. This indicates that the TBACN aggregates are sufficiently open to allow PPA access to the platelets' surfaces over the three-day reaction period. The ^{31}P MAS NMR spectrum for the PPA+TBACN(dried, dil-

DI) product (Figure 2.12b) confirms PPA grafting, but the XRD pattern (Figure 2.13) has no peak (other than residual non-exfoliated HCN), and thus no evidence of CN platelet ordering in the dried product. If the suspension initially contained disordered aggregates of TBACN before PPA grafting, then the lack of layering order in the dried PPA+TBACN(dried, dil-DI) product seems reasonable.

Finally, for TBACN stock suspension dried and then re-dispersed/diluted into TBA solution [TBACN(dried, dil-TBA)], DLS (Table 2.1) again shows that the TBACN platelets are well dispersed, as expected, with all face surfaces accessible to PPA. After adding PPA (3:1 molar ratio to CN unit cells), its concentration is again one-half of that in the PPA+TBACN(light, dark) samples. However, because TBACN(dried, dil-TBA) was dried and then re-dispersed into fresh TBA solution, the TBA^+:CN ratio was 2:1, double that of the starting TBACN stock suspension. The lower driving force for PPA grafting and the greater competition from TBA^+ for the CN surface result in a lower PPA grafted amount: PPA:CN is 0.235 (Table 2.2) for PPA+TBACN(dried, dil-TBA). The XRD pattern for this product (Figure 2.13) again has a relatively broad peak centered near 5.1°, consistent with turbostratic ordering and a polydispersity of d-spacing centered at 1.73 nm. Despite the lower PPA grafted amount, grafting still appears to occur on the face surfaces of exfoliated TBACN platelets.   Upon drying, the platelets in PPA+TBACN(dried, dil-TBA) restack with turbostratic order and a mean d-spacing less than that of TBACN (2.48 nm) or PPA+TBACN(light, dark) (2.12-2.17 nm), but more than that of the starting HCN (1.48 nm).
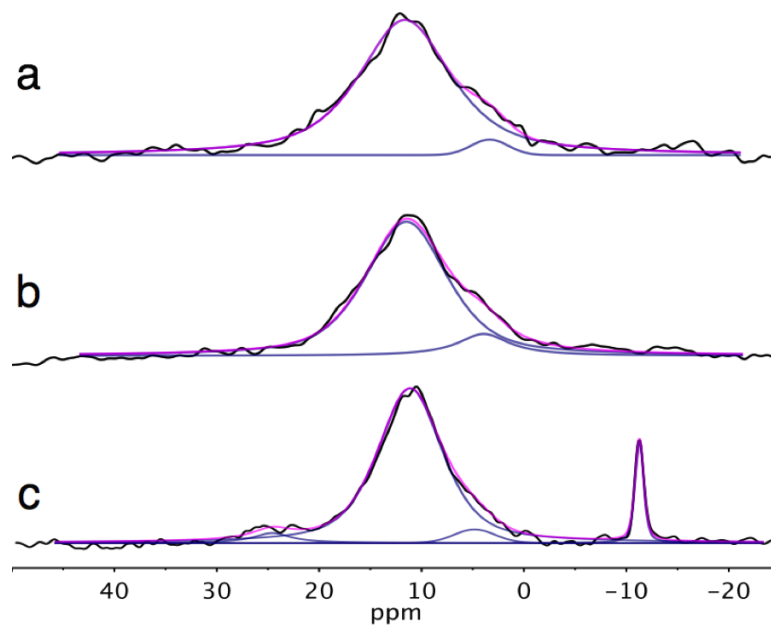
Figure 2.12. ^{31}P MAS NMR spectra with peak fitting for PPA+TBACN products prepared using TBACN suspensions processed in various ways: PPA added to (a) TBACN diluted 1:1 with DI water [PPA+TBACN(dil-DI)]; (b) TBACN dried and re-dispersed in DI water [PPA+TBACN(dried, dil-DI)]; and (c) TBACN dried and re-dispersed in TBA solution [PPA+TBACN(dried, dil-TBA)]. The resulting suspensions all had the same TBACN wt% and 3:1 PPA:CN ratio, and all were refluxed in light.
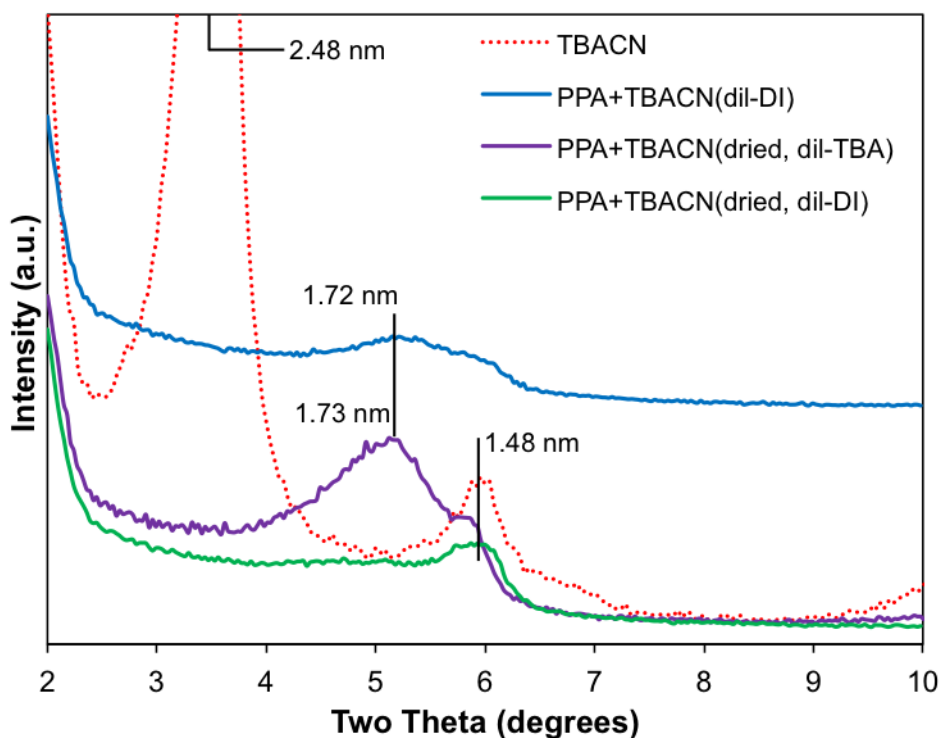
Figure 2.13. XRD patterns for TBACN and PPA+TBACN products prepared using TBACN suspensions processed in various ways: PPA added to TBACN diluted 1:1 with DI water [PPA+TBACN(dil-DI)]; PPA added to TBACN dried and re-dispersed in DI water [PPA+TBACN(dried, dil-DI)]; and PPA added to TBACN dried and re-dispersed in TBA solution [PPA+TBACN(dried, dil-TBA)]. The curve for PPA+TBACN(dil-DI) is shifted upwards for clarity.

The ^{31}P MAS NMR results provide another piece of evidence suggesting that the driving force for PPA grafting is lower in the diluted suspensions. For PPA grafting in TBACN suspension dried and re-dispersed in TBA solution [PPA+TBACN(dried, dil-TBA)], the NMR spectrum (Figure 2.12c) has an additional peak at -11.5 ppm, consistent with the production of polyphosphate or polyphosphonate species [22, 23, 104, 106]. To reiterate, in this reaction mixture, the TBA:CN ratio is 100% higher (2:1) than in TBACN stock suspension, but the PPA concentration is 50% lower. The adsorbed TBA^{+} presents a more formidable steric barrier that may inhibit PPA grafting, especially when the PPA

concentration is low. Some of the PPA may oligomerize in solution to form poly(phenylphosphonate) esters that may be adsorbed or grafted on the CN platelets. Alternately, the forcing conditions may result in the production of a small amount of precipitated calcium phenylphosphonate [23, 89, 94, 95, 107].

TGA results for PPA+TBACN products prepared using diluted or dried/re-dispersed TBACN suspensions are consistent with the NMR, XPS, and XRD results. Figure 2.14 shows the TGA mass losses and loss rates for PPA+TBACN products prepared using diluted or dried/re-dispersed TBACN suspensions. In all three cases, the mass losses of the PPA+TBACN products over 150-700°C (values in Figure 2.15) are less than the corresponding values (Figure 2.3) for TBACN suspensions processed the same way, but containing no PPA. This tells us that these PPA+TBACN products contain less TBA^+ than the corresponding TBACN suspensions processed the same way, but containing no PPA, implying that the PPA grafting process facilitated the removal of TBA^+ from the CN platelets. More TBA^+ remained on the CN platelets when the stock suspensions were simply diluted and refluxed (Figure 2.3) in the absence of PPA.

The mass loss and derivative mass loss curves (Figure 2.14) show that these PPA+TBACN products have significant mass losses and accelerated mass loss rates in the 350-550°C range, which must be due primarily to grafted PPA. However, the amounts of grafted PPA are less than those found for PPA grafted in more concentrated suspensions (Figure 2.8a). For PPA+TBACN prepared in TBACN suspension that had been dried and re-dispersed in DI water (Figure 2.14a), the total (150-700°C) and 350-550°C mass losses are higher than the other two cases. This suggests that PPA may

46

preferentially partition into, and graft within the TBACN aggregates present in this suspension.

The shapes of the derivative curves in Figure 2.14b suggest that these PPA+TBACN products contain some residual TBA^+ or byproducts of its photo-degradation. This is consistent with the view that for grafting in diluted suspensions, there is less driving force for PPA to displace the adsorbed TBA^+. Figure 2.15 provides values of the mass losses for these PPA+TBACN products over the key temperature ranges. Comparison with Figure 2.9 suggests that the PPA+TBACN products prepared in diluted or dried/re-dispersed suspensions contain both grafted PPA and residual TBA^+. The total amounts of organics are less than that in the starting TBACN (indicating loss of TBA^+). However, the presence of both PPA and residual TBA^+ (or its degradation byproducts) make it difficult to extract more quantitative information on their relative amounts in these products.
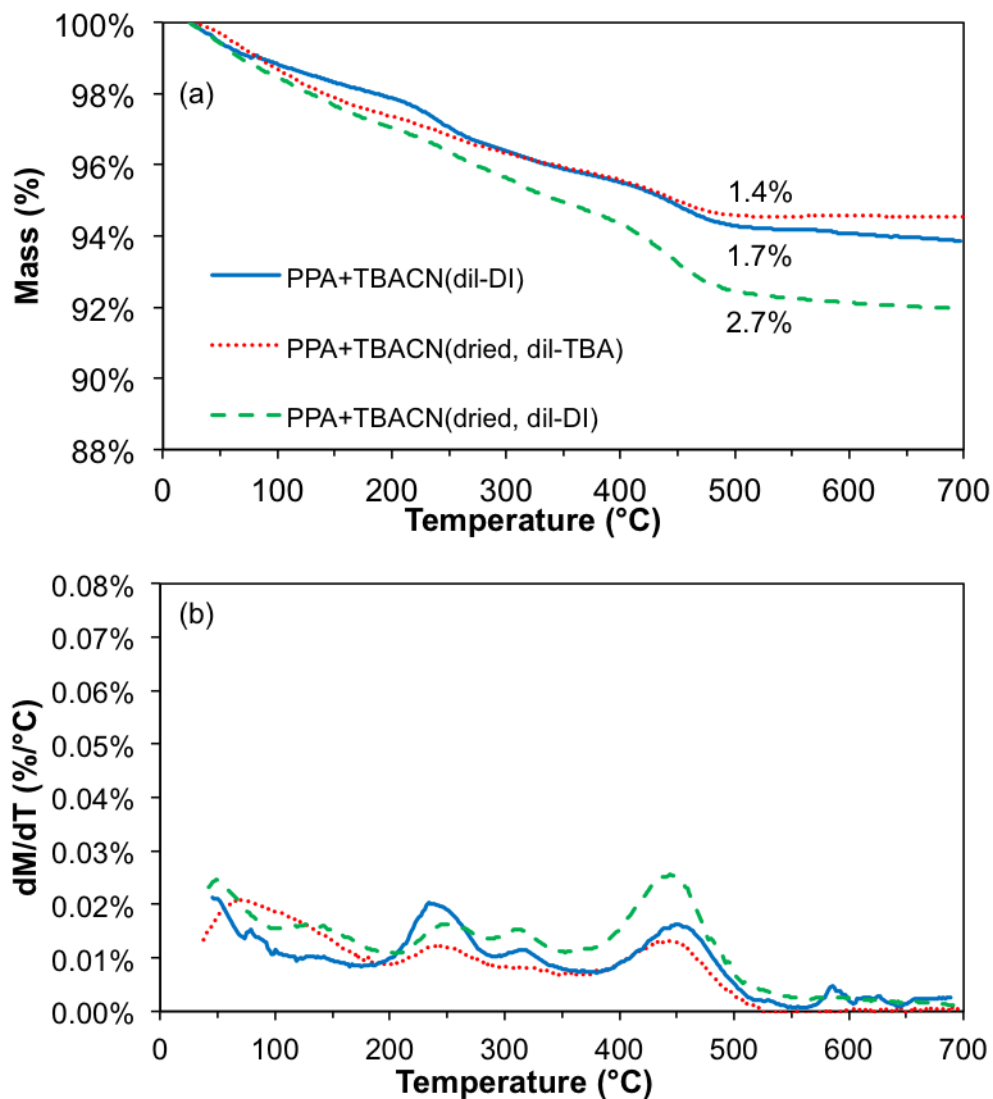
Figure 2.14. TGA characterization of mass percentage (a) and its derivative (b) as functions of temperature for PPA+TBACN products prepared using TBACN suspensions processed in various ways: PPA added to TBACN diluted 1:1 in DI water [PPA+TBACN(dil-DI)]; PPA added to TBACN dried and re-dispersed in DI water [PPA+TBACN(dried, dil-DI)]; and PPA added to TBACN dried and re-dispersed in TBA solution [PPA+TBACN(dried, dil-TBA)]. The starting suspensions all had the same TBACN wt%, PPA added at 3:1 PPA:CN ratio, and then refluxed in light. Numbers in (a) indicate mass percentage decreases from 350°C to 550°C.
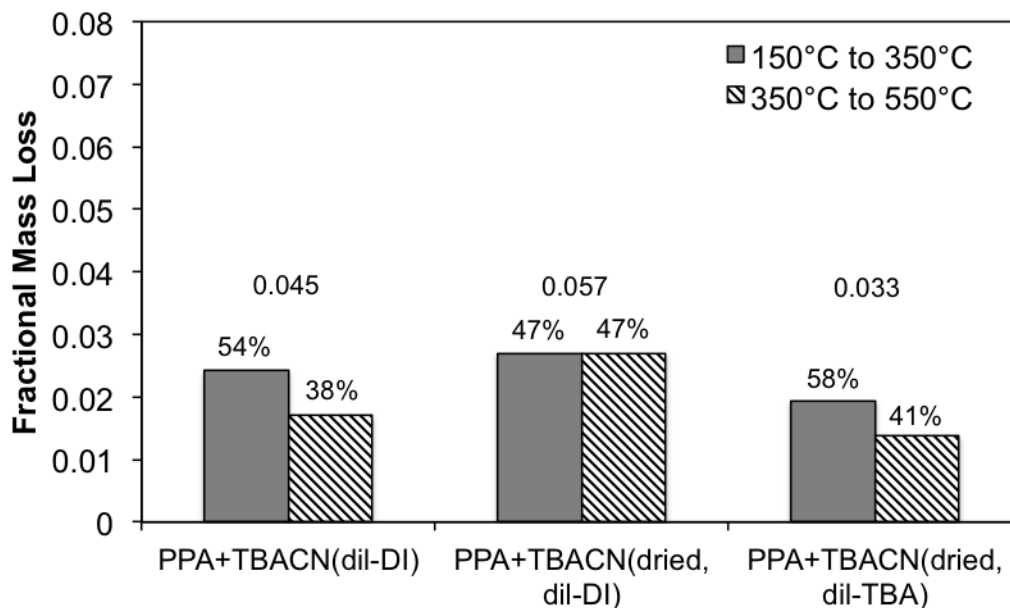
Figure 2.15. Fractional mass losses measured by TGA for PPA+TBACN products prepared using aqueous TBACN suspensions processed in various ways: PPA added to TBACN diluted 1:1 in DI water [PPA+TBACN(dil-DI)]; PPA added to TBACN dried and re-dispersed in DI water [PPA+TBACN(dried, dil-DI)]; and PPA added to TBACN dried and re-dispersed in TBA solution [PPA+TBACN(dried, dil-TBA)]. The starting suspensions all had the same TBACN wt%, PPA added at 3:1 PPA:CN ratio, and were refluxed in light. The decimal values are the fractional mass losses over 150-700°C; the percentages of the 150-700°C mass loss in the 150-350°C and 350-550°C ranges are shown above each bar.

2.3.2.4. PPA Grafting Modes

Phenylphosphonic acid has three functional groups (two P-OH and one P=O) available for covalent bonding with CN, with a total of five possible grafting modes (two monodentate, two bidentate, and one tridentate) [89, 108-114]. ^{31}P MAS NMR, FT-IR, and XPS spectra can aid in identifying the dominant grafting modes for different experimental conditions.

PPA and HCN. The FT-IR spectrum for pure PPA (Figure 2.16) agrees with those previously published [115, 116]; band assignments may be found within these references. The FT-IR spectrum for as-prepared HCN has a shoulder at 779 cm^{-1} identified [103] as the bridging Nb-O-Nb stretching vibration; split peaks at 904 and 942 cm^{-1} associated with the terminal Nb-O stretching vibration [103]; and the H-O-H bending vibration at 1635 cm^{-1}. The only significant overlap of PPA and CN bands lies in the 900-950 cm^{-1} range, where two of PPA's P-O stretching vibrations [116] overlap with the aforementioned CN terminal Nb-O stretching vibration [103]. Figure 2.16 also shows the spectra for three PPA+CN products; Table 2.3 lists the tentative band assignments based on the relevant literature.

PPA+HCN. The PPA+HCN product has the same bands as HCN, except that the HCN peak at 904 cm^{-1} appears as a shoulder in PPA+HCN. This may be due to an overlapping peak at 940 cm^{-1} usually ascribed to a P-O stretch [115, 116]. PPA+HCN has distinctive peaks at 1153 cm^{-1} (probably P-C stretch), 1439 cm^{-1} (aromatic C-C), 1597 cm^{-1} (weak, aromatic C-C), and 3059 cm^{-1} (aromatic C-H stretch, not shown), all indicative of PPA grafting. This spectrum also shows a strong, broad band in the 1200-1250 cm^{-1} range due to the P=O stretch (refs. in Table 2.3). The survival of this group

50

tells us that PPA grafting in PPA+HCN primarily involves PPA's P-OH groups. The PPA+HCN spectrum also shows a broad band in the 975-1100 cm^{-1} range normally associated with a variety of P-O stretching vibrations (refs. in Table 2.3). The lack of distinct peaks in this range probably indicates a distribution of Nb-O-P grafts, as one might expect for PPA grafting on edges and faces of unexfoliated HCN particles.

The ^{31}P MAS NMR spectrum for PPA+HCN (Figure 2.5b) can be deconvoluted into three overlapping peaks centered at 17.7, 11.5, and 4.6 ppm. Increasing upfield shifts (to lower ppm values) are consistent with stronger binding or grafting modes [108]. Thus these three peaks could represent mono-, bi-, and tridentate PPA grafting; as observed for PPA grafting onto amorphous zirconia and titania [23, 24, 88, 89, 107, 111]. The occurrence of bidentate grafting with P=O surviving might be expected at the edges of CN platelets where "broken" niobate octahedra expose Nb-(OH)$_2$ sites available for PPA grafting via condensation with P-OH groups. The availability of Nb-(OH)$_2$ sites also facilitates the formation of tridentate-grafted PPA, which does not seem to occur much for PPA grafting onto TBACN face surfaces.

PPA+TBACN. For the products of PPA grafting onto exfoliated TBACN, the FT-IR spectra have the same vibrational bands for grafting in light or darkness (Figure 2.16), and for various suspension processing conditions (Figure 2.17). All of the PPA+TBACN spectra inherit the 779 and 942 cm^{-1} bands from HCN. The HCN 904 cm^{-1} band, however, is either weak or absent, perhaps due to reaction of PPA with terminal Nb-O groups. The 904 cm^{-1} band may also be hidden by the superposition of the HCN 942 cm^{-1} band and the P-OH bands at 930 and 945 cm^{-1}, inherited from PPA. This would suggest that residual P-OH groups survive after mono- or bidentate PPA grafting.
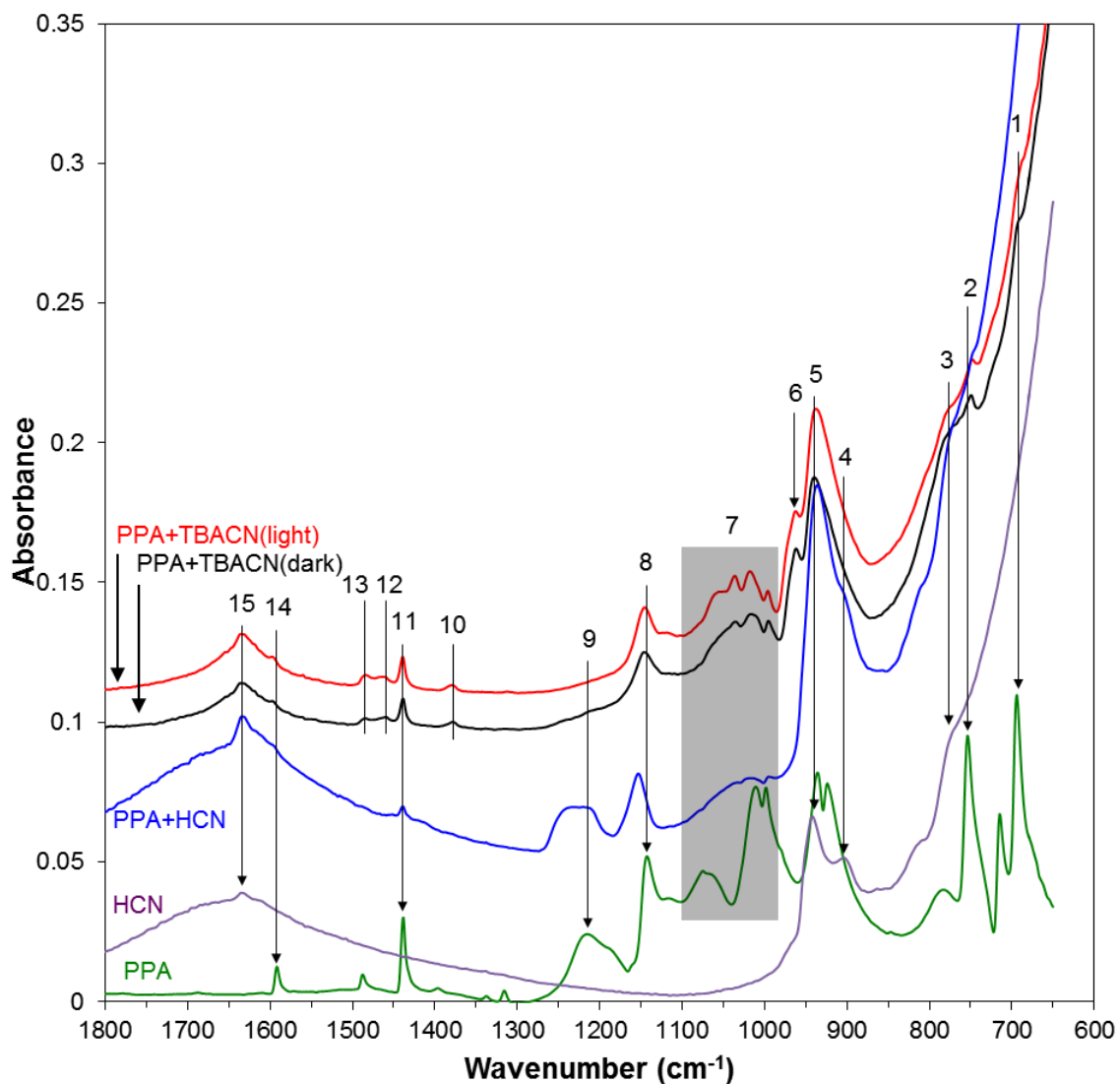
Figure 2.16. FT-IR spectra for (bottom to top): PPA; HCN; PPA+HCN refluxed in DI water and in light; PPA+TBACN refluxed in darkness; and PPA+TBACN refluxed in light. Spectra are shifted vertically; and the PPA spectrum rescaled, for visual clarity. Table 2.3 lists band (peak) assignments.
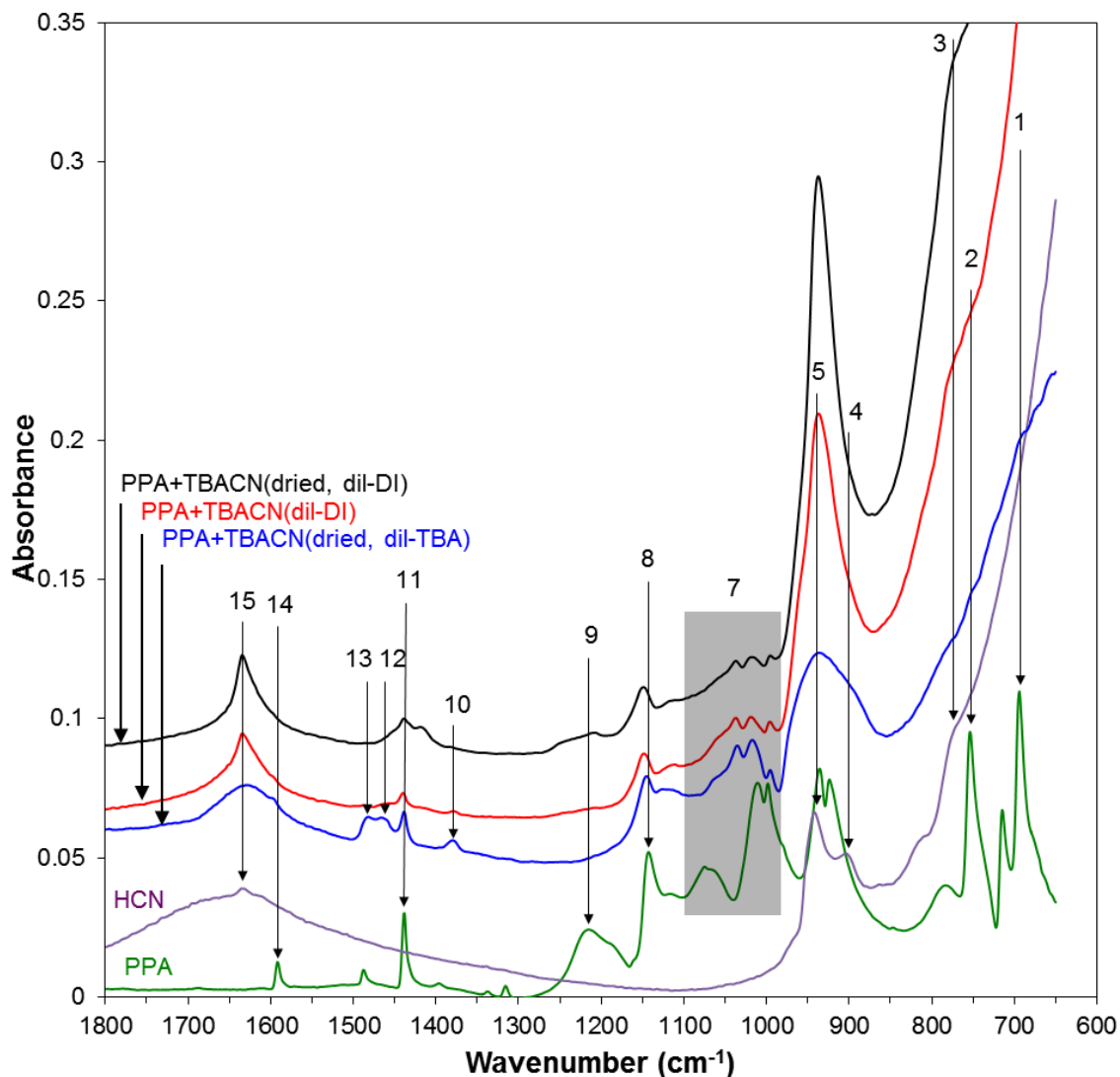
Figure 2.17. FT-IR spectra for (bottom to top): PPA; HCN; PPA+TBACN dried and re-dispersed in TBA solution [PPA+TBACN(dried, dil-TBA)]; PPA+TBACN diluted 1:1 in DI water [PPA+TBACN(dil-DI)]; and PPA+TBACN dried and re-dispersed in DI water [PPA+TBACN(dried, dil-DI)]. The starting suspensions all had the same TBACN wt%, PPA added at 3:1 PPA:CN ratio, and were refluxed in light. Spectra are shifted vertically; and the PPA spectrum rescaled, for visual clarity. Table 2.3 lists band (peak) assignments.

Table 2.3. Band assignments for numbered peaks in the FT-IR spectra shown in Figures 2.16, 2.17, 2.25, and 2.28.

| No.	σ (cm^{-1})	Source	Mode (a)	References
1	691 (sh)	PPA	C-H oop	[37, 58, 115, 117, 118]
2	748	PPA	C-H oop	[37, 58, 117, 118]
3	779 (sh)	HCN	Nb-O bridge	[103]
4	904	HCN	Nb-O term.	[103]
5	942	HCN	Nb-O term.	[103]
6	962	PPA+HCN	Nb-O-P	this work
7	975-1100	PPA	P-O	[20, 22, 23, 31, 58, 115, 116, 117, 119, 120]
8	1145, 1153	PPA	P-C	[22, 23, 116, 120]
9	1220	PPA	P=O	[20, 22, 23, 31, 58, 115, 116, 119, 121]
10	1379	TBA$^+$	aliph. C-H	[96]
11	1439	PPA	arom. C-C	[115, 116, 117, 118]
12	1462	TBA$^+$	aliph. C-H	[96]
13	1484	TBA$^+$	aliph. C-H	[96]
14	1597	PPA	arom. C-C	[116]
15	1636	H$_2$O	H-O-H bend	[96, 103]

(a) Abbreviations: oop = out-of-plane bending; sh = shoulder; term. = terminal; aliph. = aliphatic; arom. = aromatic.

The PPA+TBACN spectra exhibit various vibrational bands (C-H, C-C, P-C) expected due to the presence of grafted PPA. We see almost no absorbance due to the P=O band (1200-1250 cm^{-1}) in the PPA+TBACN spectra, indicating the primary role of P=O in the grafting of PPA onto TBACN [20, 22, 23, 58, 121]. In the 975-1100 cm^{-1} range, PPA has a series of distinctive P-O bands (refs. in Table 2.3). In PPA+TBACN, this wavenumber range has several distinct, overlapping peaks (996, 1018, 1036, 1052 cm^{-1}) also attributed to various P-O vibrations, including those of PO$_3^{2-}$ and HPO$_3^{1-}$ [115]. The presence of P-OH and Nb-O-P vibrational bands is also likely, but we cannot make definitive assignments for these bands. Lastly, the spectra in Figure 2.16 for PPA+TBACN products have a distinct peak at 962 cm^{-1} (peak 6) that does not appear in the spectra for PPA, HCN, or PPA+HCN. Shimada et al. [58] ascribed a band at ~950 cm^{-1} to P-OH, but it seems more likely due to Nb-O-C in their starting material,

lanthanum niobate with interlayer-grafted decanol. In PPA+TBACN, the absence of the terminal Nb-O band at 904 cm^{-1} and appearance of the 962 cm^{-1} peak suggests that the latter may be a stretching vibration of Nb-O-P.

^{31}P MAS NMR spectra for PPA+TBACN products (Figures 2.5 and 2.12) show that experimental conditions influence PPA grafting modes. For PPA grafting on TBACN in the light (Figure 2.5c), the NMR spectrum may be deconvoluted into two peaks, one smaller and one larger centered at 16.4 and 10.7 ppm, respectively. These peaks likely correspond to mono- and bidentate grafting modes involving P=O (primarily) and some P-OH groups. Although the FT-IR band(s) for residual P-OH groups cannot be conclusively identified, locations at 945 cm^{-1} and in the 975-1100 cm^{-1} range seem plausible. The blend of mono- and bidentate grafting can be rationalized in two ways. As mentioned earlier, PPA initially grafted in bidentate mode may, upon prolonged exposure to light during reflux, undergo TBACN-catalyzed photo-degradation, resulting in reversion of some bidentate grafts to monodentate form. Alternately, over time, photo-degradation of adsorbed TBA$^+$ could free some space on the TBACN surface, permitting additional PPA grafting in the monodentate mode via P=O reaction with niobate Lewis acid sites.

For PPA grafted onto TBACN in the darkness (Figure 2.5d), the peak in the NMR spectrum may be deconvoluted into two closely overlapping peaks (13.1 and 10.8 ppm). The overall upfield shift suggests primarily bidentate grafting, and the two peaks could correspond to different bidentate modes (bridged and chelated, *vide infra*). The bidentate-chelating mode may be somewhat more prevalent in this case due to the steric hindrance of adsorbed TBA$^+$.

The PPA graft density may also be a relevant factor. For the PPA+TBACN(light, dark) products, the PPA:CN molar ratios are greater than 0.5 (Table 2.2), which is half of the maximum ratio assuming 100% bidentate grafting (PPA:CN = 1.0). PPA+TBACN products prepared in diluted TBACN suspensions have lower PPA graft densities (PPA:CN ratios between 0.24 and 0.35, Table 2.2) due to the lower PPA concentration and driving force for grafting. The ^{31}P MAS NMR spectra for these products (Figure 2.12) have one main peak centered in the 11.1-11.6 ppm range, associated (as argued above) with the bidentate grafting mode. These spectra also appear to have small secondary peaks centered in the 3-5 ppm range, possibly consistent with the tridentate grafting mode. The lower graft density may make it easier for bidentate-grafted PPA molecules to find an open neighboring site for a third covalent bond. However, the large majority of the PPA molecules appear to be grafted in the bidentate mode.

The complexity of the FT-IR band structures in the 975-1100 cm^{-1} range and the overlap of PPA and HCN bands (Figure 2.16) make it difficult to conclusively assign any band to P-OH in the FT-IR spectra of the PPA+TBACN products. On the other hand, XPS O1s spectra (Figures 2.18-2.20) provide strong qualitative evidence for the presence of surviving P-OH groups in the PPA+TBACN products. Specifically, deconvolution of the XPS O1s spectrum for PPA (Figure 2.18) gives two peaks at 531.1 and 532.5 eV with a 1:2 area ratio, consistent with P=O and P-OH, respectively [112, 122-125]. The O1s spectrum for HCN (Figure 2.18), similar to that found previously [126], can be deconvoluted into two peaks at 530.0 and 531.4 eV, which we ascribe to bridging Nb-O-Nb and terminal Nb-OH. The P-OH peak from PPA (532.5 eV) does not appear in the HCN spectrum, but it does appear in the O1s spectra of all the PPA+TBACN products

56

(Figures 2.19 and 2.20). This shows that at least some P-OH groups survive the grafting process. Variations in PPA grafted amounts and sampling depth preclude a more quantitative analysis based on peak areas. Nonetheless, the XPS O1s results support our argument that PPA grafts onto the face surfaces of TBA-exfoliated CN platelets primarily in the bidentate mode.
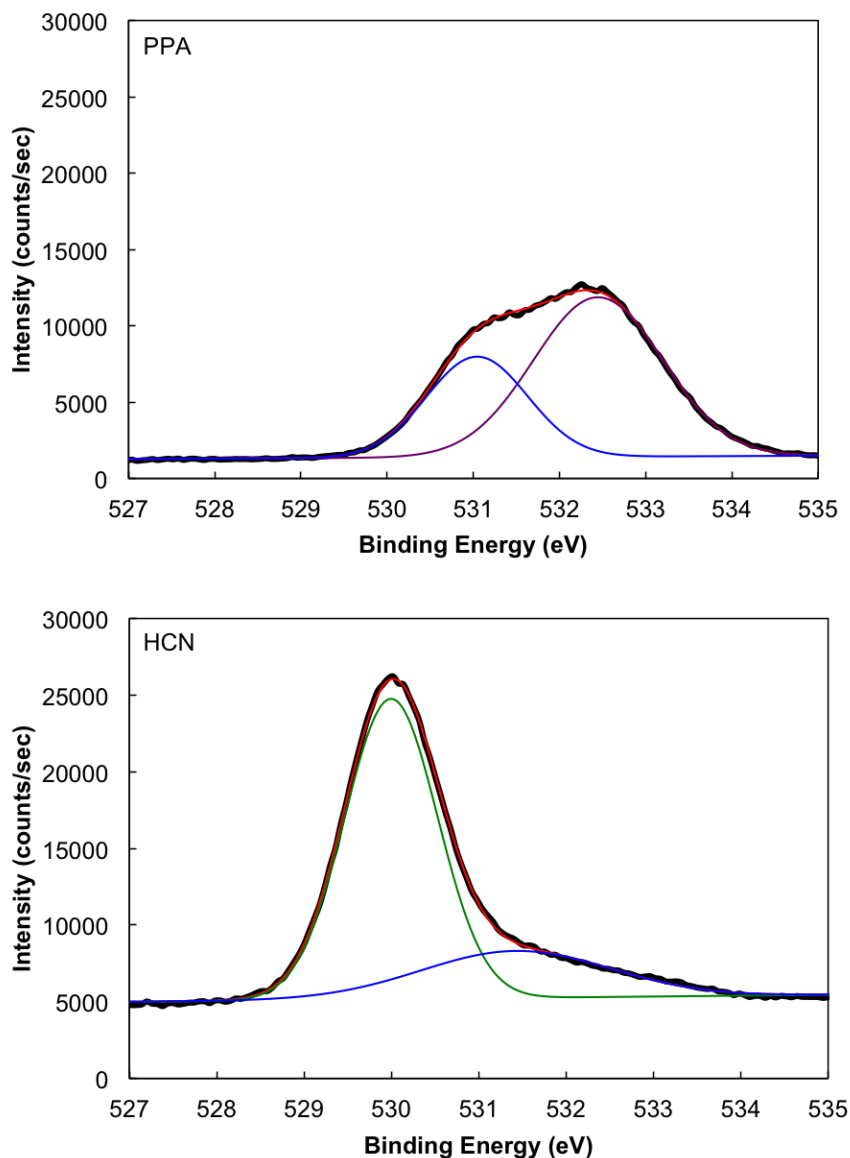
Figure 2.18. XPS O1s spectra for PPA (top) and as-prepared HCN (bottom).
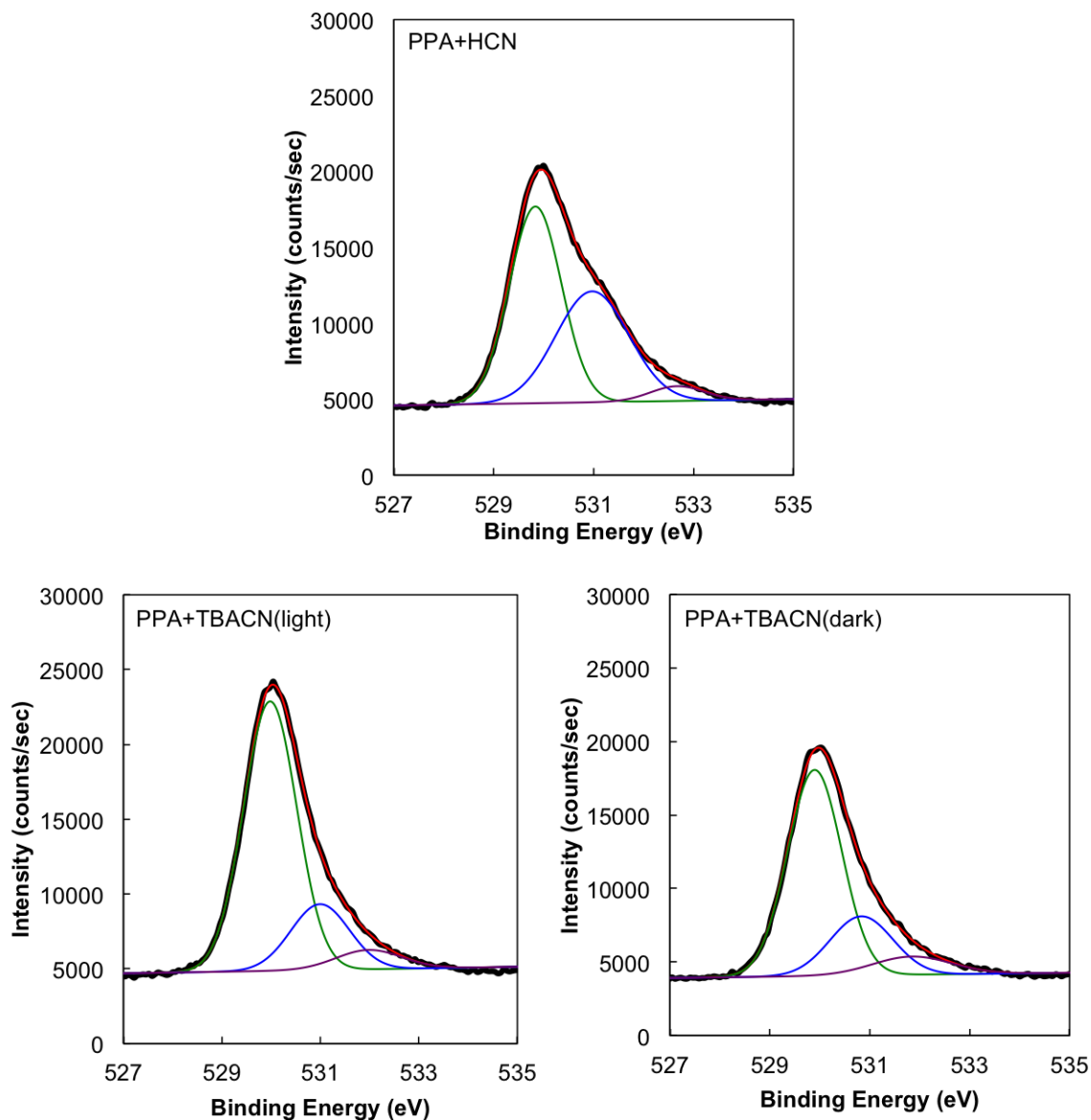
Figure 2.19. XPS O1s spectra for: PPA+HCN; PPA+TBACN(light); and PPA+TBACN(dark), as indicated in each plot.
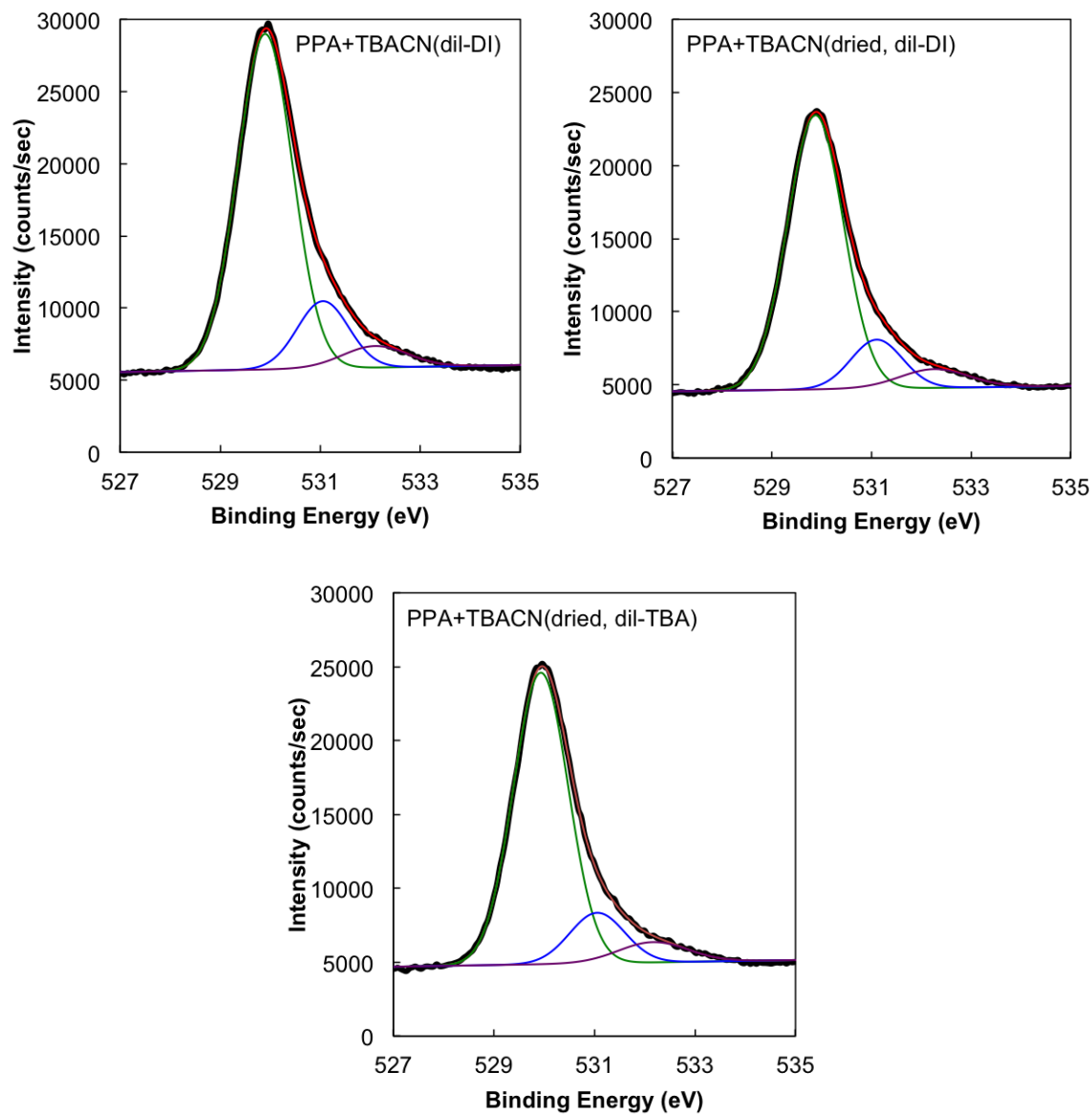
Figure 2.20. XPS O1s spectra for: PPA+TBACN diluted 1:1 in DI water [PPA+TBACN(dil-DI)]; PPA+TBACN dried and re-dispersed in DI water [PPA+TBACN(dried, dil-DI)]; and PPA+TBACN dried and re-dispersed in TBA solution [PPA+TBACN(dried, dil-TBA)].

Figure 2.21 illustrates a proposed mechanism, consistent with the results presented, for grafting of PPA (and possibly other organophosphonic acids) onto the face surfaces of crystalline, protonated calcium niobate (HCN) layers. Grafting begins with the coordination of the PPA's phosphoryl oxygen with a surface Nb atom, a Lewis acid site, accompanied by cleavage of a Nb-O-Nb bridging bond in the HCN lattice. Similar reactions have been previously proposed for cleavage of Si-O [17], Al-O [22], Ti-O [23], and other kinds of metal-oxygen bonds in metal oxides [114]. Initial monodentate grafting is then followed by secondary heterocondensation between P-OH and apical Nb-OH groups, producing bidentate grafts with either bridging or chelating modes. Geometric considerations favor both bidentate modes. Based on PPA bond distances and angles derived from molecular simulations [93], the distance between O atoms in O=P-O-H is about 2.62 Å. Considering the surface atoms in a layer of HCN (Figure 2.22), the Nb atoms reside in a square array with an Nb-O-Nb distance of 3.855 Å [105] and a diagonal distance of 5.452 Å. Thus the HCN surface can readily accommodate PPA grafting in the bidentate-bridging mode with Nb-O-P-O-Nb spanning either the side or diagonal of the square Nb atom array, depending on the Nb-O-P bond angles. The bidentate-chelating mode may form when the graft density is high because it does not require an adjacent apical Nb-OH site.

Geometric considerations do not appear to favor additional heterocondensation reactions of bidentate-grafted PPA to produce tridentate grafts. The geometry of the octahedral niobate lattice would require considerable deformation of (approximately) tetrahedral PPA to form the third leg of a tridentate graft. Evidence of surviving P-OH

groups from XPS O1s spectra (and possibly FT-IR spectra) appear to rule out extensive tridentate grafting.

In summary, the proposed mechanism in Figure 2.21 accounts for the primary role of P=O in grafting, as indicated by the absence of P=O groups in the FT-IR spectra of all PPA+TBACN products. The mechanism also illustrates how secondary heterocondensation may produce two kinds of bidentate grafts, depending on the availability of adjacent sites. The coordination of Nb remains at six in this mechanism, avoiding a concern about seven-fold coordination raised in the one previous study of PPA interlayer grafting on a niobate [58].
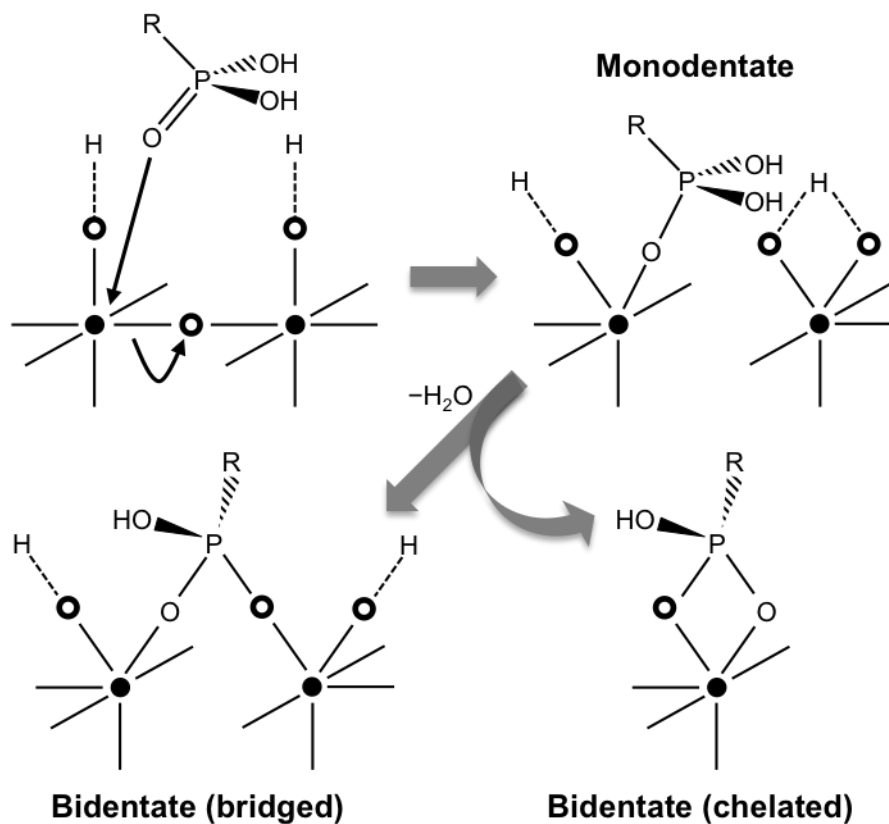
Figure 2.21. Schematic illustration of a proposed mechanism for organophosphonic acid grafting onto the surface of HCN. Filled and open circles denote Nb and O atoms respectively in the crystal structure of HCN layers; only surface Nb atoms are shown, and most O atoms in the HCN lattice are omitted for clarity.
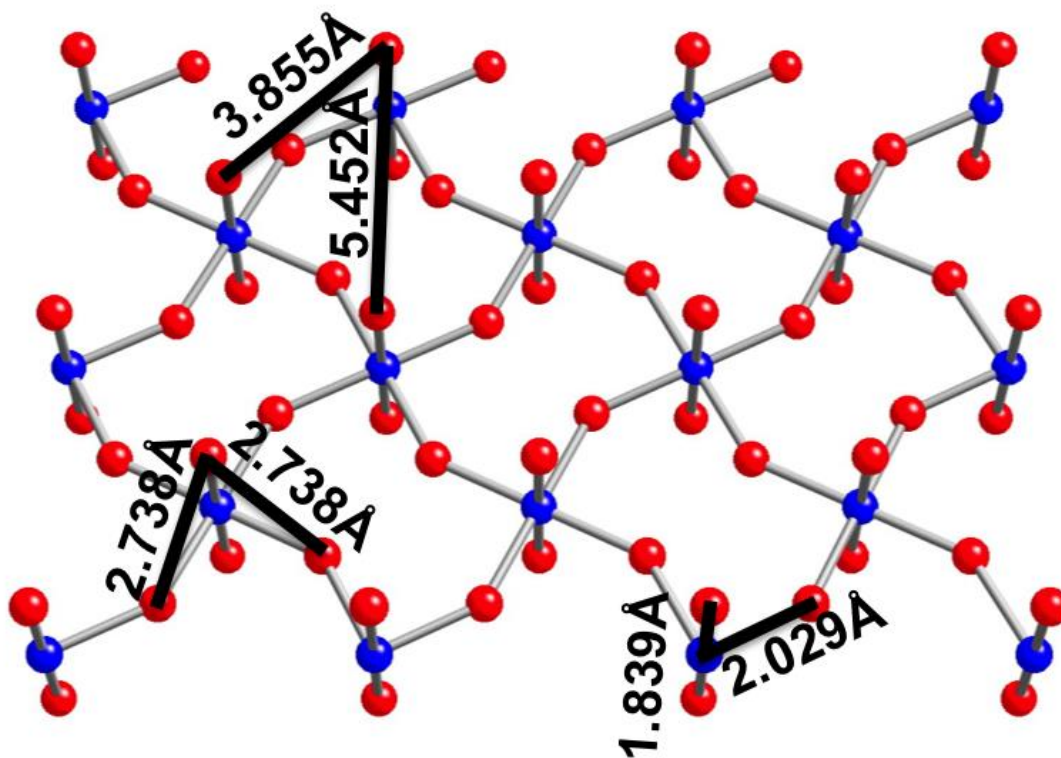
Figure 2.22. Perspective view of the HCN surface showing the top layer of Nb and O atoms (blue and red, respectively). The Nb atoms reside on a square lattice with Nb-O-Nb distance of 3.855 Å; this is also the distance between adjacent apical O atoms. The diagonal distance between two Nb atoms in the square array is 5.452 Å. Other selected Nb-O and O-O distances are indicated on the diagram.

2.3.3. PPA Grafting in HCN and TBACN Alcoholic Suspensions

This section explores PPA grafting onto HCN and TBACN in alcohol-based suspensions, specifically ethanol and *n*-propanol at 95% and 99% (balance water).

PPA+HCN. PPA grafting on unexfoliated HCN in ethanol and *n*-propanol was examined. Figure 2.23 shows the ^{31}P MAS NMR spectra for the washed, dried products of refluxing PPA with as-prepared HCN dispersed in these alcohols. For 95% ethanol (Figure 2.23a), peaks that indicate PPA grafting do not appear, perhaps due to the limited sample amount. For 99% *n*-propanol (Figure 2.23b), a small monomodal peak centered at 13 ppm appears, an upfield shift of about 8.4 ppm relative to the signature PPA peak at 21.4 ppm (Figure 2.5a). The presence of a weak peak indicates at least a small amount of PPA grafting. The signature peak of PPA does not appear in Figure 2.23, indicating the absence of non-grafted PPA, which was presumably washed out of the product in the cleaning stage. XPS results (Table 2.2) indicate the presence of P in these samples. Both NMR spectra (Figure 2.23) show peak(s) at about -12 ppm, consistent with non-grafted polyphosphate or polyphosphonate species [22, 23, 104, 106]. This could be rationalized in terms of PPA-PPA condensation to form polyphosphate due to prolonged reflux, or attack of HCN by PPA to form niobium phenylphosphonate [23, 89, 107].
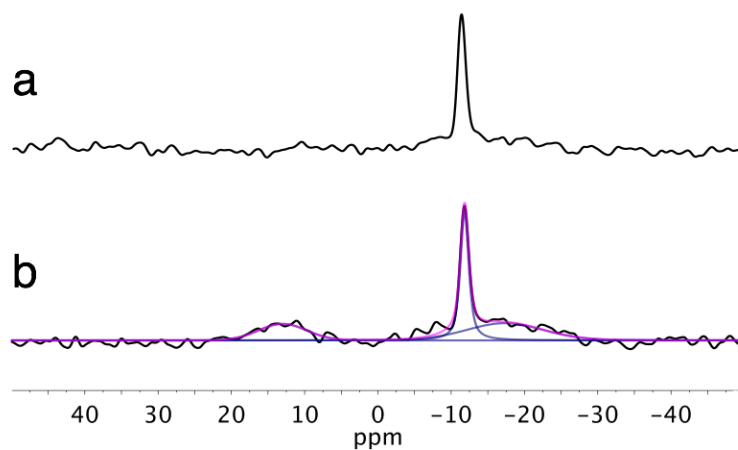
Figure 2.23. ^{31}P MAS NMR spectra for: (a) PPA+HCN refluxed in 95% ethanol, and (b) PPA+HCN refluxed in 99% *n*-propanol. Suspensions were refluxed in light. PPA was added to CN in a 3:1 molar ratio.

Figure 2.24a shows TGA results for PPA+HCN in 95% ethanol or 99% *n*-propanol. The total mass loss and loss rate curves are almost the same as those of as-prepared HCN (Figure 2.1a). Compared to PPA+HCN grafting in DI water (Figure 2.8a), the mass losses in the 350-550°C range for PPA+HCN in 95% ethanol or 99% *n*-propanol (Figure 2.24a) are nearly zero. Apparently PPA surface grafting to non-exfoliated HCN is not as favorable, perhaps because PPA and HCN are not well-dispersed in alcohols based on visual observation and DLS results in Table 2.1.

Figure 2.24b shows XRD patterns for the washed, dried PPA+HCN alcohol products, along with the pattern for as-prepared HCN. The patterns for PPA+HCN refluxed in alcohols show a small peak consistent with the starting HCN, but with lower intensity. There are no XRD peaks at lower angles. This shows that PPA does not uniformly penetrate and expand the HCN interlayer space, as previously found for PPA grafting onto a layered niobate that had been "pre-expanded" by grafted decanol [58]. Thus the XRD patterns do not provide any conclusive information on whether or not PPA grafts onto HCN face surfaces in alcoholic suspensions. The FT-IR spectra for these products (Figure 2.25) do not indicate the presence of grafted PPA in these samples.

In summary, these results support the conclusion that only small amounts of PPA graft onto HCN in ethanol or *n*-propanol suspensions. The location of PPA grafting is inconclusive.
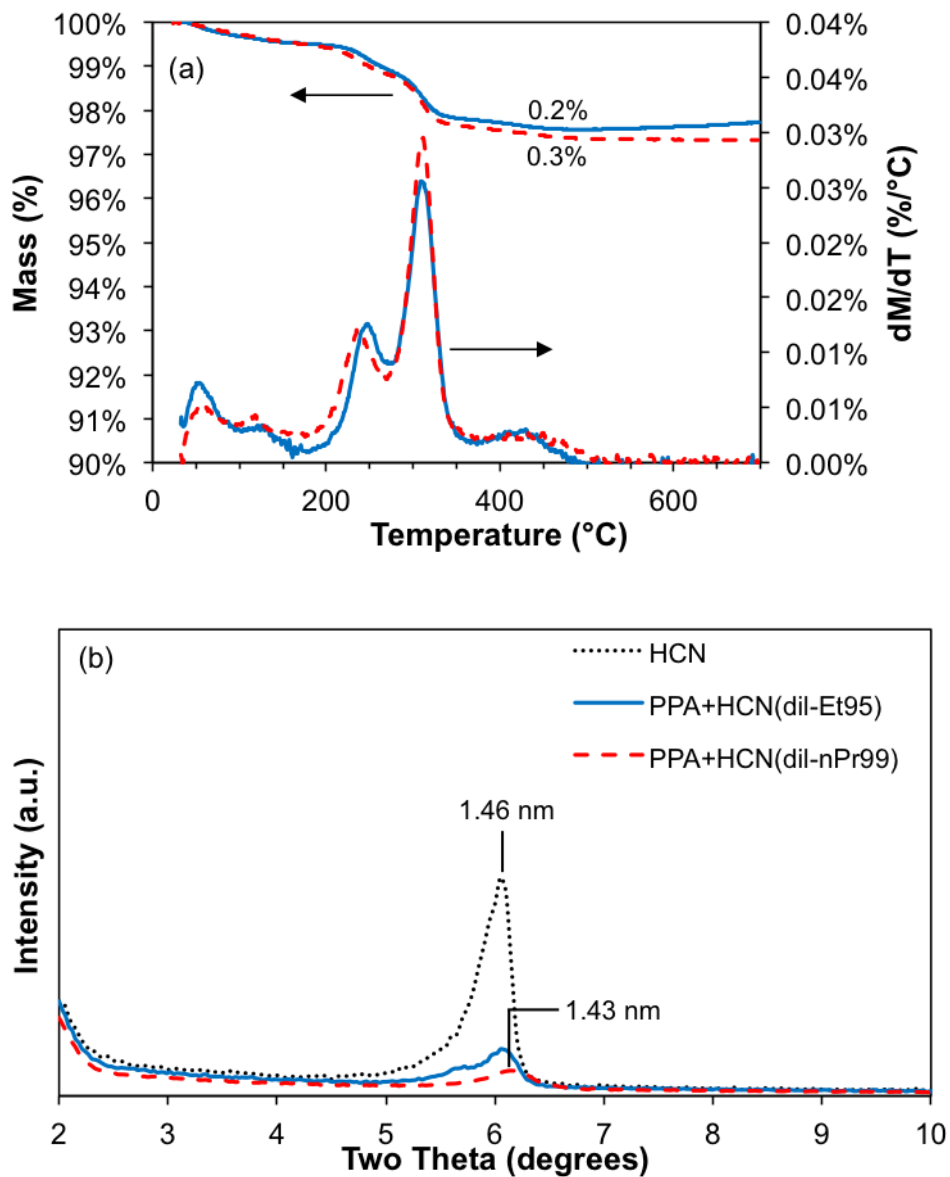
Figure 2.24. Characterization of PPA+HCN refluxed in 95% ethanol [PPA+HCN(dil-Et95)] and 99% *n*-propanol [PPA+HCN(dil-nPr99)]: (a) mass percentage and its derivative as functions of temperature from TGA, and (b) XRD patterns over the low-angle range. Suspensions were refluxed in light. Numbers in (a) indicate mass percentage decreases from 350°C to 550°C.
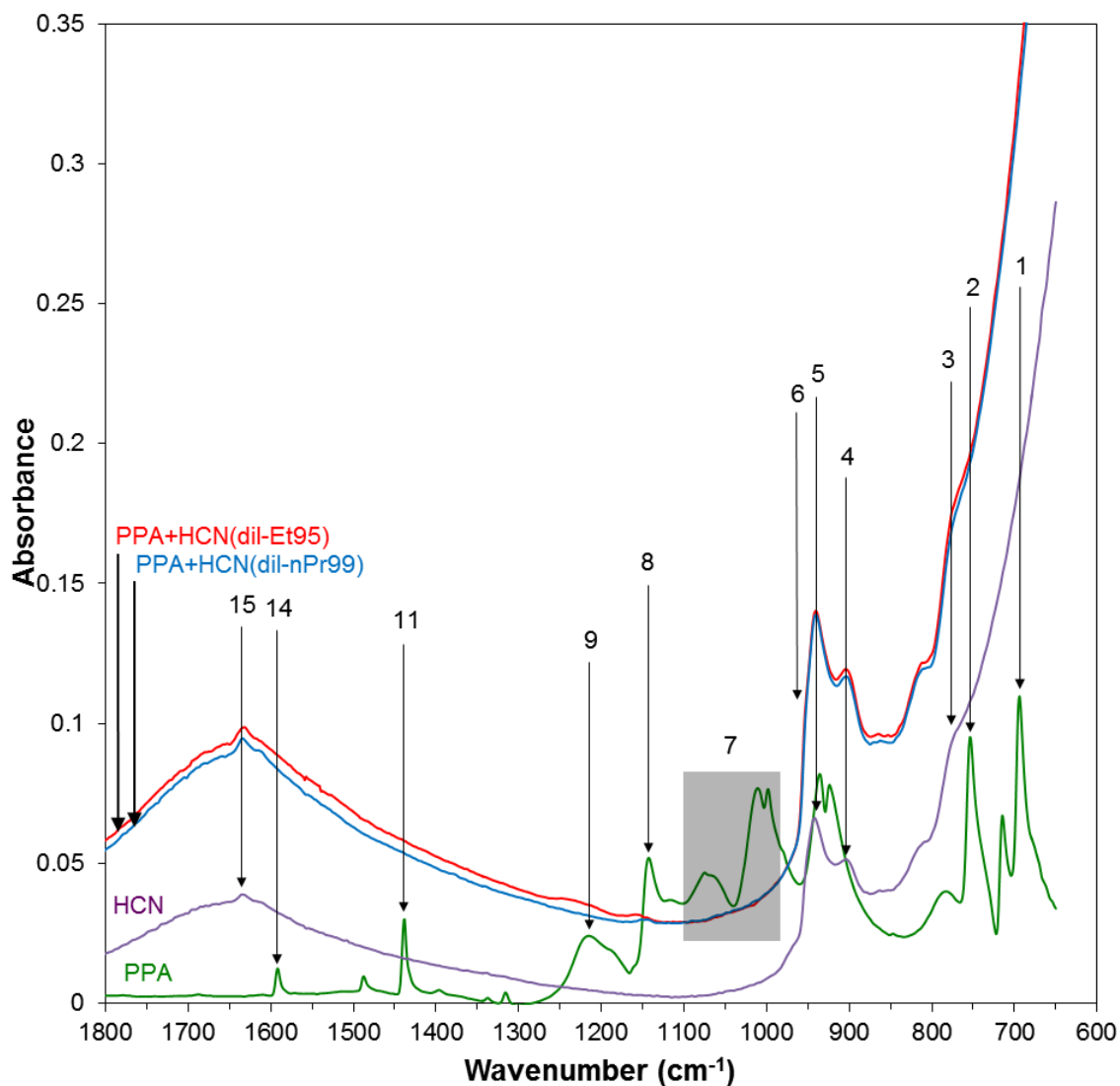
Figure 2.25. FT-IR spectra for (bottom to top): PPA; HCN; PPA+HCN dispersed in 99% *n*-propanol [PPA+HCN(dil-nPr99)]; and PPA+HCN dispersed in 95% ethanol [PPA+HCN(dil-Et95)]. Suspensions were refluxed in light. Peak assignments are described in Table 2.3. Spectra are shifted vertically; and the PPA spectrum rescaled, for visual clarity.

PPA+TBACN. DLS (Table 2.1) shows that direct dilution of TBACN suspension to 5.0×10^{-5} g/mL in 95% ethanol [TBACN(dil-Et95)] results in a stable alcoholic suspension of exfoliated TBACN platelets. However, drying TBACN and re-dispersing in alcohols results in particle sizes larger than that of exfoliated platelets. This shows that dried TBACN does not re-exfoliate in alcohols, but instead incompletely disperses as disordered aggregates, resembling TBACN dried and re-dispersed in DI water [TBACN(dried, dil-DI)].

Figure 2.26 shows ^{31}P MAS NMR spectra for the washed, dried products of PPA added to TBACN that was dried and re-dispersed in alcohols. For grafting in ethanol (95% and 99%, Figure 2.26a and b, respectively), the spectra of the PPA+TBACN products have monomodal peaks centered between 14-16 ppm, an upfield shift of ~6-7 ppm relative to PPA. This demonstrates that PPA grafts onto TBACN dispersed in ethanol. The spectra do not manifest peaks at 21 ppm indicative of non-grafted PPA, signifying that all of the detected PPA has been grafted. XPS results (Table 2.2) imply that the PPA grafted amounts on TBACN in ethanol are about 65% less than in aqueous TBACN suspensions. The XRD patterns (Figure 2.27) for these samples have small peaks at angles corresponding to a d-spacing of about 1.5 nm, probably due to residual, non-exfoliated HCN. Otherwise, the absence of any distinctive peaks is consistent with dried aggregates lacking any turbostratic ordering.

The magnitude of the upfield shifts of the peaks in the ^{31}P MAS NMR spectra suggest that PPA grafting on TBACN in ethanol produces primarily monodentate grafted PPA [23, 89, 107, 121]. The FT-IR spectra for these products (Figure 2.28) do not show any indication of bands at 1220 cm^{-1}, indicating that P=O groups do not survive the

69

grafting process. The spectra show distinct shoulders near 962 cm^{-1}, consistent, in our view, with the formation of Nb-O-P linkages. However, the survival of P-OH groups cannot be definitively established either by FT-IR or XPS O1s spectra. Still, PPA grafting onto TBACN in ethanol appears to follow at least the first step of the mechanism proposed in Figure 2.21.

For PPA grafting onto TBACN in *n*-propanol, the ^{31}P MAS NMR spectra (Figure 2.26c and d) also indicate PPA grafting, although the grafted amounts (from XPS, Table 2.2) are smaller than in aqueous TBACN suspensions. For grafting in 95% *n*-propanol (Figure 2.26c), the dominant peak at ~11 ppm suggests that PPA grafts onto TBACN primarily in the bidentate mode. A small peak near 4 ppm may indicate some tridentate grafting, or perhaps just noise in the data. For grafting in 99% *n*-propanol (Figure 2.26d), the NMR spectrum can be deconvoluted into two peaks at 16.5 and 11 ppm. This suggests the presence of both monodentate and bidentate grafting modes. The FT-IR spectra (Figure 2.28) for the products refluxed in *n*-propanol are similar to those for ethanol: no band for P=O survives the grafting process. Thus, PPA grafts onto TBACN (in *n*-propanol) via the P=O group, consistent with the first reaction in Figure 2.21.

All of the ^{31}P MAS NMR spectra in Figure 2.26 could have overlapping peaks that could not be deconvoluted due to the low grafted amounts and weak NMR signals. Thus, all of the PPA+TBACN products refluxed in alcohols could have a mixture of PPA grafting modes that may not be apparent in Figure 2.26. The peaks at about -11 ppm in Figure 2.26b and c are again consistent with PPA undergoing a reaction other than with TBACN. This reaction may produce polyphosphate or polyphosphonate species [22, 23, 104, 106], or precipitated calcium phenylphosphonate [23, 89, 94, 95, 107].
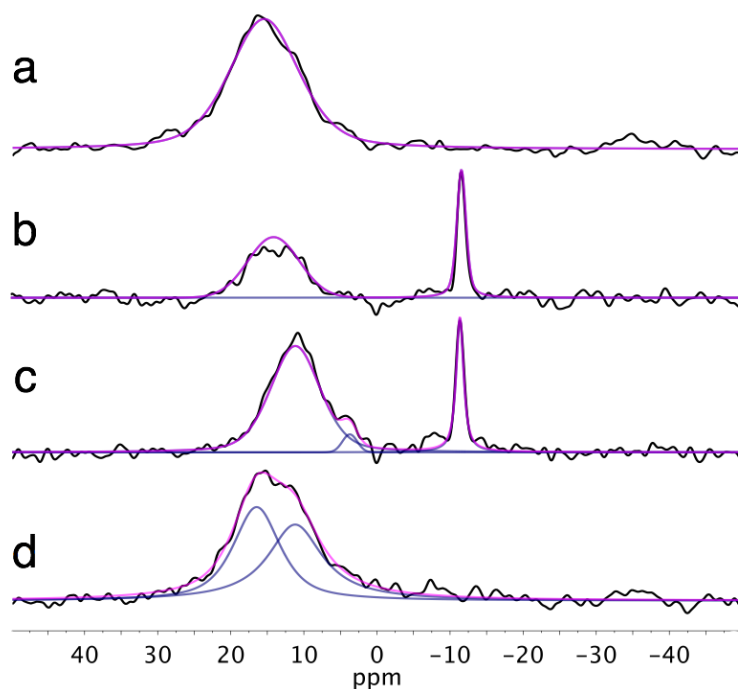
Figure 2.26. ^{31}P MAS NMR spectra with peak fitting for PPA+TBACN products prepared using TBACN suspensions dried and re-dispersed in alcohol solvents: (a) PPA+TBACN dried and re-dispersed in 95% ethanol [PPA+TBACN(dried, dil-Et95)]; (b) PPA+TBACN dried and re-dispersed in 99% ethanol [PPA+TBACN(dried, dil-Et99)]; (c) PPA+TBACN dried and re-dispersed in 95% *n*-propanol [PPA+TBACN(dried, dil-nPr95)]; and (d) PPA+TBACN dried and re-dispersed in 99% *n*-propanol [PPA+TBACN(dried, dil-nPr99)]. The resulting suspensions all had the same TBACN wt% and 3:1 PPA:CN ratio, and all were refluxed in light.
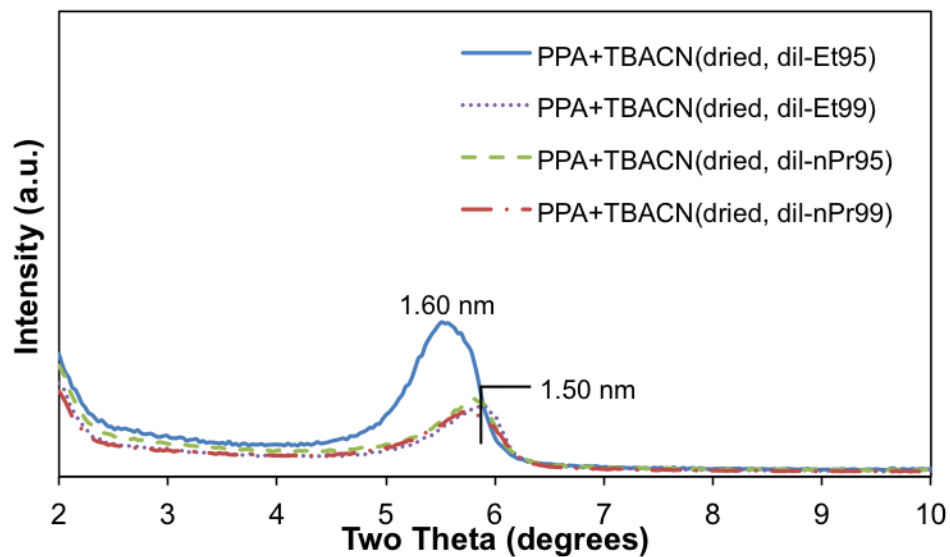
Figure 2.27. XRD patterns for PPA+TBACN products prepared using TBACN suspensions dried and re-dispersed in alcohol solvents: PPA+TBACN dried and re-dispersed in 95% ethanol [PPA+TBACN(dried, dil-Et95)]; PPA+TBACN dried and re-dispersed in 99% ethanol [PPA+TBACN(dried, dil-Et99)]; PPA+TBACN dried and re-dispersed in 95% *n*-propanol [PPA+TBACN(dried, dil-nPr95)]; and PPA+TBACN dried and re-dispersed in 99% *n*-propanol [PPA+TBACN(dried, dil-nPr99)]. The resulting suspensions all had the same TBACN wt% and 3:1 PPA:CN ratio, and all were refluxed in light.
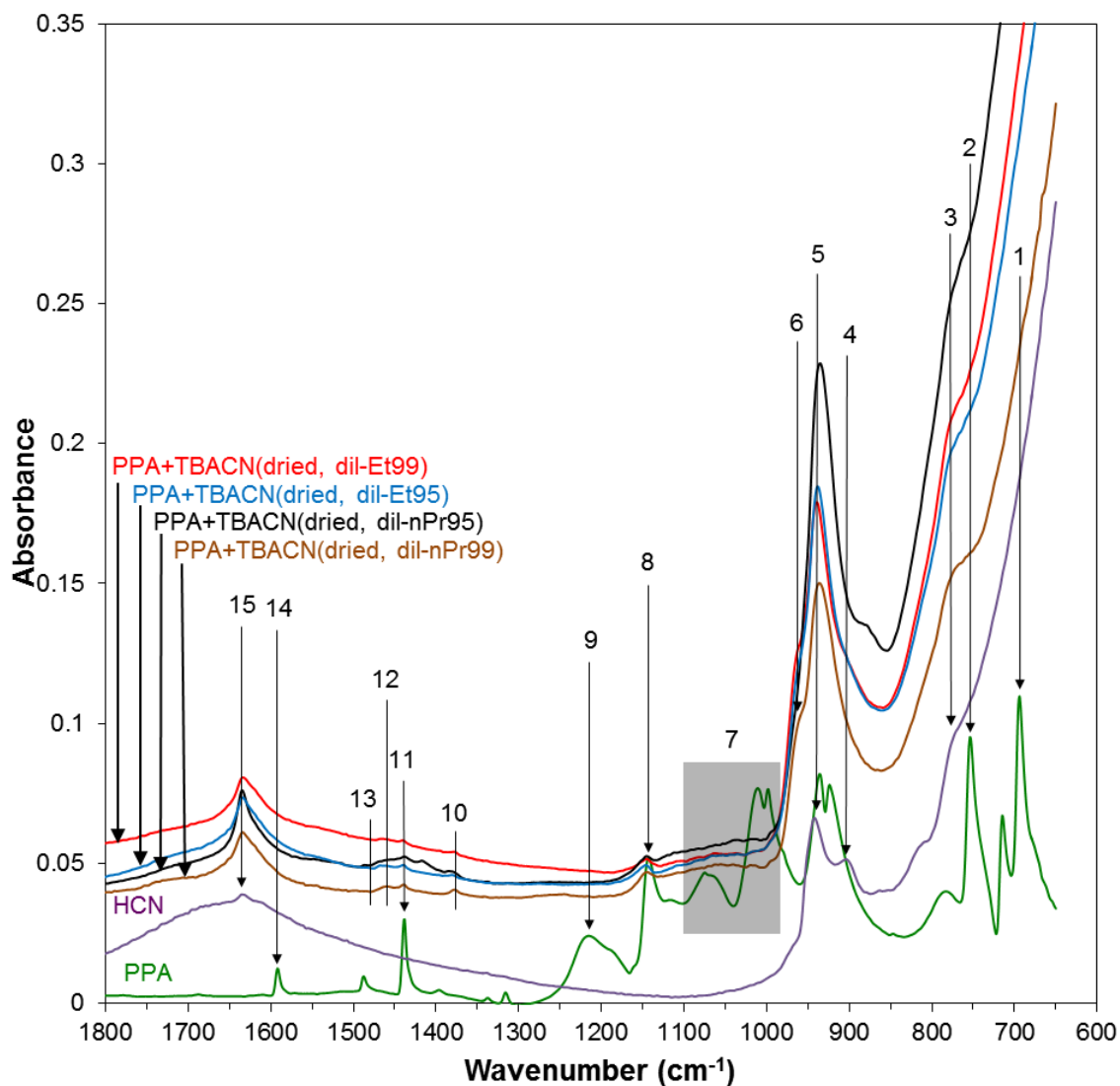
Figure 2.28. FT-IR spectra for (bottom to top): PPA; HCN; PPA+TBACN dried and re-dispersed in 99% *n*-propanol [PPA+TBACN(dried, dil-nPr99)]; PPA+TBACN dried and re-dispersed in 95% *n*-propanol [PPA+TBACN(dried, dil-nPr95)]; PPA+TBACN dried and re-dispersed in 95% ethanol [PPA+TBACN(dried, dil-Et95)]; and PPA+TBACN dried and re-dispersed in 99% ethanol [PPA+TBACN(dried, dil-Et99)]. Peak assignments are described in Table 2.3. Spectra are shifted vertically; and the PPA spectrum rescaled, for visual clarity.
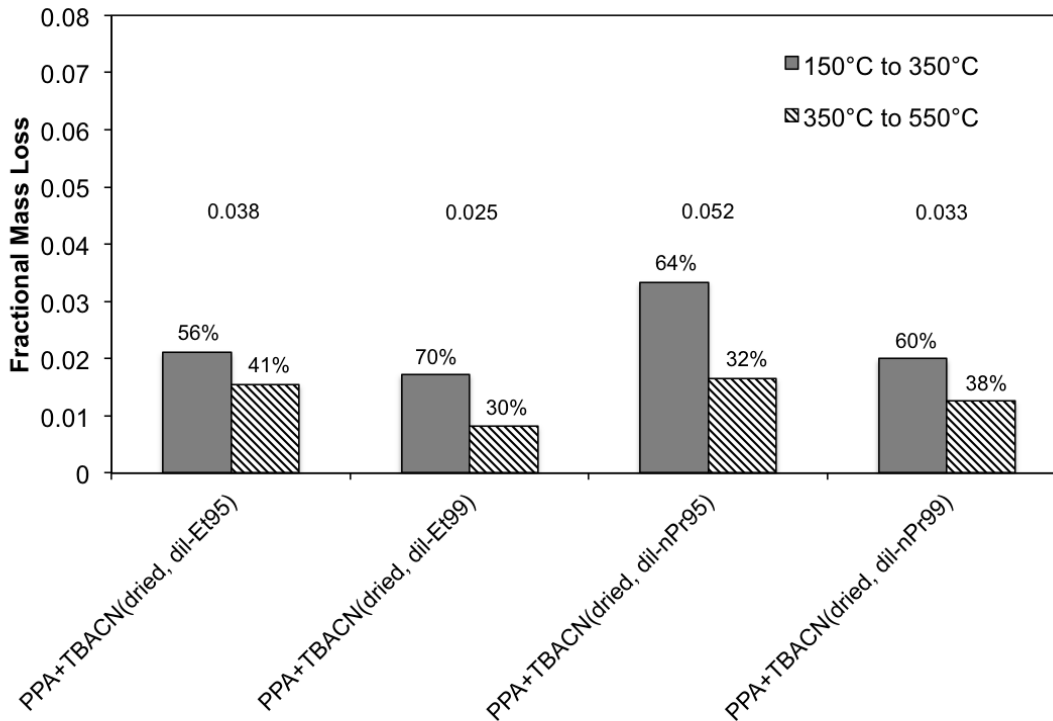
Figure 2.29. Fractional mass losses measured by TGA for PPA+TBACN products prepared using alcoholic TBACN suspensions: PPA+TBACN dried and re-dispersed in 95% ethanol [PPA+TBACN(dried, dil-Et95)]; PPA+TBACN dried and re-dispersed in 99% ethanol [PPA+TBACN(dried, dil-Et99)]; PPA+TBACN dried and re-dispersed in 95% *n*-propanol [PPA+TBACN(dried, dil-nPr95)]; and PPA+TBACN dried and re-dispersed in 99% *n*-propanol [PPA+TBACN(dried, dil-nPr99)]. The resulting suspensions all had the same TBACN wt% and 3:1 PPA:CN ratio, and all were refluxed in light. The decimal values are the fractional mass losses over 150-700°C; the percentages of the 150-700°C mass loss in the 150-350°C and 350-550°C ranges are shown above each bar.

2.4. Conclusions

This work shows that phenylphosphonate (PPA) can be covalently grafted onto protonated calcium niobate (HCN). PPA grafts onto the face surfaces of TBA-exfoliated HCN (TBACN) dispersed in deionized water, TBA solution, ethanol, and *n*-propanol. However, PPA does not penetrate and graft in HCN's interlayer spaces, but grafts only onto the exterior surfaces of unexfoliated HCN. This work contrasts with other recent reports of interlayer PPA grafting onto niobate sheets that were "pre-expanded" by interlayer grafted decanol [58, 127]. We believe that this is the first report of organic molecule grafting, and certainly organophosphonic acid grafting, onto the face surfaces of exfoliated, niobate-based platelets. Kimura et al. [127] recently reported interlayer PPA grafting on layered hexaniobates, followed by exfoliation in organic solvents. The present work represents the first report of organic molecule grafting onto layered niobate perovskites in aqueous suspensions.

Various characterization results confirm not only the grafting of PPA on exfoliated TBACN, but also quantify the PPA grafted amount and identify the grafting mode (mono-, bi-, and tridentate). The PPA grafting location and grafted amount depends on the exfoliation/aggregation state of TBACN, suspension processing conditions, and solvent composition. Due to the photocatalytic properties of the layered calcium niobate perovskite, the state of light/darkness probably plays some role in the grafting process. In the starting TBACN suspensions, adsorbed TBA^+ cations undergo photo-degradation under reflux conditions in light, but not in darkness. PPA seems to graft onto TBACN primarily in the bidentate mode, but prolonged exposure in light may result in some PPA degradation and/or reversion of some bidentate grafts to the

monodentate form. A mechanism proposed for PPA grafting onto HCN and TBACN seems to account for all experimental observations.

The demonstration of PPA grafting onto exfoliated, TBA-exchanged HCN in aqueous and organic solvents may be the first step towards the synthesis of more sophisticated organo-functional niobate platelets. For example, grafting phosphonate-based initiators or chain transfer agents, followed by surface-initiated polymerization, could lead to polymer-grafted platelets (PGPs). Ultimately, PGPs could be used as building blocks for fabrication of polymer nanocomposites with tailored end-use performance for automotive, aerospace, and energy applications.

Chapter 3:   Effect of Interfacial Pretreatment on the Properties of Montmorillonite/Poly(vinyl alcohol) Nanocomposites

Unlike calcium niobate, montmorillonite (MMT) was shown in Chapter 1 to be able to readily disperse in aqueous suspensions without needing additional help. Thus, MMT can be straightforwardly incorporated into polymer nanocomposites (PNCs) consisting of poly(vinyl alcohol) (PVOH) matrix utilizing the solution blending technique. Previous research discovered, however, that the properties of the resulting PNCs are not as "ideal" as one would expect. It is believed that this is due to bridging between polymer chains adsorbed on the surface of neighboring MMT platelets producing aggregates. Chapter 3 explores the effect of "pretreating" the MMT surface with a small amount of a low-weight, compatible polymer before adding in the polymer matrix to counter polymer bridging. Characterization results compare two pretreatment methods with untreated MMT and the corresponding neat polymer matrix.

3.1. Introduction

PNCs are increasingly utilized in automotive, aerospace, energy, and flame retardant applications. PNCs may offer significant performance advantages over traditional polymer composites, including: (1) enhanced physical properties; (2) ability

to tailor material properties for new applications; (3) improved performance/weight ratio achieved by reduction of filler loadings from 15-40 vol% to as little as 1-5%; and, (4) improved processing performance.

Advances in the fundamental understanding of the role of the filler-polymer interface (really an "interphase") have driven growth in PNC applications. As discussed in many reviews of PNC research [128-145], the interphase has distinct properties that are amplified by the high interfacial area/volume ratio achieved when the filler particles have nanoscale dimensions. The properties of the interphase also control the dispersion state of the nanoparticles in the polymer. Poor nanoparticle dispersion reduces interfacial area and thus the contribution of the interphase to the composite properties. Consequently, achieving enhanced nanocomposite properties and performance depends critically on maximizing nanoparticle dispersion in the polymer.

The challenge lies in overcoming attractive particle-particle interactions responsible for filler aggregation. Considerable research has focused on the design of filler-polymer interphases to maximize nanoparticle dispersion in polymers [140-141, 146-153]. For example, early work on clay/polymer PNCs utilized cation exchange treatment of clay minerals with alkylammonium salts to make the clay platelets more hydrophobic and (in principle) more compatible with polymers [128-132, 134, 139, 143-144]. More recent work explores covalent grafting of polymers on particles for tailoring interphase properties and particle dispersion [146, 149-153]. Work to date has primarily emphasized tailoring the interphase to control nanoparticle dispersion in polymers. Less attention has been given to evaluating the "direct" contribution of the particle-polymer interphase to PNC properties [148, 154].

Consider, for example, the well-studied PNC consisting of exfoliated montmorillonite (MMT) platelets dispersed in poly(vinyl alcohol) (PVOH) [155-164]. Using a suitable cleaning protocol [165], aqueous suspensions of fully-exfoliated MMT can be prepared without the need for dispersants. PVOH is water-soluble and readily adsorbs onto MMT [166-172]. These facts suggest that MMT and PVOH are naturally compatible. Using the solution-blending method [155-158, 160-164], one should be able to prepare "model" or "ideal" nanocomposites consisting of fully-exfoliated MMT platelets randomly dispersed in a PVOH matrix.

In many cases, the barrier properties of "ideal" MMT/PVOH PNCs fall short of what one might expect based on the "tortuous path" model [173-176]. For example, values of water vapor permeability [155] and diffusivity [160] in MMT/PVOH composites (with MMT loadings up to 6 wt%) were found to be about 60% lower than those in pure PVOH. Yeh et al. [158] observed that water vapor and oxygen permeabilities in MMT/PVOH PNCs initially decreased with increasing MMT loading, but then increased significantly above 5 wt% MMT. Grunlan et al. [161] found the opposite trend: depending on relative humidity, oxygen permeability in MMT/PVOH initially increased with MMT loading, reaching a maximum at about 3 wt%, before decreasing at higher loadings. These observations are not only inconsistent, but also disagree with predictions of various tortuous path models, all of which predict sharp, monotonic decreases in gas permeability with increasing platelet loading. These gas permeation studies reveal that our idealized picture of internal structure in exfoliated PNCs must not be complete.

At least two factors may complicate our picture of how structure develops in MMT/PVOH nanocomposites during solution blending and densification of the parent solutions. First, the dissolved PVOH may induce MMT inter-platelet attraction, either through bridging adsorption [166, 168, 171-172, 177-180] or depletion flocculation [168, 177, 180-181]. Second, PVOH may undergo gelation or de-mixing during densification, opening up the possibility of MMT partitioning into a preferred phase [182-184]. These factors have not been considered in previous studies of MMT/PVOH nanocomposites.

We have found that exfoliated MMT platelets tend to re-stack or aggregate at some point during the solution blending and densification processes that transform MMT and PVOH solutions into a solid MMT/PVOH nanocomposite. The objective of this work is to explore the role of MMT platelet interactions on platelet dispersion in MMT/PVOH nanocomposites prepared by solution blending. The first part of this work demonstrates that MMT platelet re-stacking takes place during the solution blending process. The second part investigates a novel concept, MMT surface "pretreatment" by adsorption of low molecular weight homopolymer (PVOH) or block copolymer (F108 Pluronic[®]) from a dilute solution. This pretreatment may prevent bridging flocculation by blocking the MMT surface before solution blending with the PVOH matrix polymer. We assess the impact of MMT pretreatment on platelet dispersion as well as the thermal, mechanical, and gas barrier performance of MMT/PVOH nanocomposites.

3.2. Experimental

3.2.1. Preparation of MMT Suspensions

Stock suspensions of fully-exfoliated MMT (Cloisite Na$^+$, Southern Clay Products, Inc.) were prepared following our published procedure [165]. Typically, the as-received MMT powder is dispersed at 1.0 wt% in deionized (DI) water, mixed at room temperature for at least 12 h, sonicated for 30 min (Fischer-Scientific FS-28), centrifuged at 4000 rpm (2000 g) for 60 min (fixed-angle Eppendorf 5403 centrifuge), followed by careful decanting of the supernatant suspension. The product suspension typically contains about 0.75 wt% MMT (batch-to-batch values ranging from 0.60 to 0.90 wt%) as measured by dry weight analysis. Our previous AFM study [165] shows that the MMT platelets in these suspensions are essentially fully exfoliated; histograms of MMT platelet thickness and aspect ratio (Figures 3.2 and 3.3) can be found in the Results and Discussion, section 3.4.1. [185].

The stock MMT suspension is used to prepare two kinds of pretreated MMT platelet suspensions as well as PVOH nanocomposite films. To prepare MMT pretreated with low molecular weight PVOH (11-31 kDa, 98-99% hydrolyzed, Alfa Aesar, used as received; denoted below as PV$_{11}$), stock MMT suspension is added drop wise to an aqueous solution of PV$_{11}$ with heating (~90°C) and mixing for at least 60 min. The MMT suspension should be added to the PVOH solution, rather than vice-versa, to minimize bridging flocculation. The PV$_{11}$ solution concentration and the volume of added MMT suspension are adjusted so that the mixture contains 0.50 wt% PV$_{11}$, and that the total solids content (i.e., polymer + MMT) is 64.3% PV$_{11}$ and 35.7% MMT by weight. The latter figure must be taken into account when the PV$_{11}$-treated MMT

81

(denoted henceforth as PV$_{11}$MMT) is solution-blended with additional matrix PVOH to prepare nanocomposites with precisely 10.0 wt% MMT loading.

For the second pretreated MMT suspension, we add MMT suspension drop wise to an aqueous solution of F108 Pluronic®, a triblock copolymer surfactant (14,600 Da, BASF, used as received) with at least 60 min mixing at room temperature. Both the central poly(propylene oxide) block (DP=44) [186] and the two poly(ethylene oxide) end blocks (DP=141) [187] may adsorb on the MMT surface. The MMT suspension and F108 solution volumes are adjusted so that the mixture has a total solids content of 75% MMT and 25% F108 by weight, with a 0.10 wt% F108 concentration. The F108-treated MMT is denoted henceforth as F-MMT.

3.2.2. *Preparation of MMT/PVOH Nanocomposite Films*

MMT/PVOH nanocomposite films were prepared using low, medium, and high molecular weight PVOH: PV$_{11}$, PV$_{95}$ (95 kDa, 95% hydrolyzed, Acros Organics, used as received), and PV$_{205}$ (205 kDa, 99+% hydrolyzed, Sigma Aldrich, used as received). Aqueous PVOH solutions are prepared by dissolution of PVOH powders in DI water with mixing at 90°C for at least 60 min. To prepare nanocomposites with 10 wt% non-pretreated MMT, an appropriate volume of stock MMT suspension is added drop wise to the warm PVOH solutions so that the final, blended suspension contains an overall PVOH concentration of 5.0 wt% and (on a solids-only basis) 10.0 wt% MMT and 90.0 wt% PVOH.

Solution blending of pretreated MMT suspensions ($PV_{11}MMT$ or F-MMT) with PVOH solutions proceeds in the same way. Suspensions of pretreated MMT were used as prepared, so one must account for the pretreatment polymer content in the blending process. The volume and concentration of PVOH solution must be adjusted so that the total polymer content (PVOH matrix plus PVOH or F108 carried by the pretreated MMT) is precisely 90 wt% in the final composites. The starting PVOH solution also has a lower initial concentration so that the final blended suspension has a total polymer concentration of about 2.0 wt%. Sample "recipes" are provided in Appendix A.

Solution casting or drawdown coating was used to make nanocomposite films. Solution cast films were prepared by depositing a known mass of blended suspension onto an aluminum pan and drying in air in an oven at either 40°C or 120°C (annealing). For drawdown coating, typically 3 to 5 mL of blend suspension was deposited onto a Mylar® sheet (supported by a balanced glass plate underneath) and drawn down using a doctor blade. A Microm II film applicator (Gardco) was configured with a doctor blade gap distance set to 1 mil (25.4 µm) in order to control the thickness of the final film. Sliding the blade slowly forms a wet film coating. The plate is then carefully covered with a shield to minimize settling of dust particles onto the wet film. The drawn films were dried at room temperature for one day, gently peeled from the Mylar sheet, dried overnight in a vacuum oven at 60°C, and then stored in a sealed desiccator. The final films typically have a thickness of 20 to 30 µm as measured using a micrometer [Mitutoyo Digimatic Micrometer MDC-MX, model 293-831].

3.3. Characterization Methods

Transmission Electron Microscopy (TEM)

Electron microscopy employed a Hitachi H-8000 transmission electron microscope (TEM). To prepare a specimen for TEM observation, it was first trimmed to the shape of the cross-section of a BEEM® conical embedding capsule. After placing the film sample in the capsule center (with the film tip aligned with the capsule tip, tip pointing down), a premixed epoxy resin was slowly poured in to embed the sample. The capsule was closed and the epoxy cured at 80°C for 24 h. After curing, the tip of the formed epoxy block was trimmed to expose the sample tip. The tip was then sectioned into several ~100 nm thin slices using an Ultra 35° diamond knife at room temperature. The floating slices were collected from water using carbon coated steel grids, air dried, then observed by TEM under an accelerating voltage of 200 KeV.

X-Ray Diffraction (XRD)

X-ray diffraction (XRD) utilized a Rigaku Ultima IV diffractometer (Cu Kα radiation, λ=1.5418Å). Small angle measurements used an incidence angle (ω) of 0.5°, divergence slit (DS) set at 0.1 mm, and scanned over a 2θ range of 0.2° to 10°. For wide angle scans (2θ from 2° to 50°), the DS was set at 0.2 mm. For both angular ranges, scans used a step size of 0.05° and a scan speed of 2 degrees/min. XRD samples were prepared by drawdown coating of films directly onto transparent glass slides with drying at room temperature.

Dynamic Light Scattering (DLS)

DLS measurements employed two instruments: DynaPro Titan (Wyatt Instruments) and Zetasizer Nano ZS ZEN3600 (Malvern Instruments). Both instruments have a temperature-control system to monitor the size of MMT nanoplatelets in dilute suspensions from samples taken throughout the film-making process. This information can determine the state of the MMT dispersion by evaluating for the extent of aggregation within the PVOH matrix. All DLS measurements start by sizing at 25°C a standard of 0.24 μm polystyrene latex uniform microspheres (Bangs Laboratories, Inc.) diluted in DI water to a solids weight fraction of either $\sim 5.0 \times 10^{-5}$ (Malvern) or $\sim 5.0 \times 10^{-6}$ (Wyatt) as a preliminary check. The DLS results for both instruments are in reasonably good agreement with the nominal listed size.

Similarly, MMT suspensions or dissolved MMT/PVOH films were also diluted in DI water to the same respective weight fraction corresponding to the instrument used. These values were chosen as a benchmark at 25°C between a too concentrated polystyrene standard and a too dilute MMT suspension of known sizes to equate for accurate and consistent DLS measurements. Temperature control was set to keep the viscosity of the water constant, while the beam intensity was also individually controlled depending on the instrument. Samples of aqueous MMT suspensions were diluted with DI water to a weight fraction of about 5.0×10^{-6} (Wyatt). Samples of cast films were dissolved in DI water and characterized by DLS (Malvern) to provide an indirect measure of MMT aggregation. Film samples were dissolved via mixing for at least 24 h in DI water at temperatures ranging from room temperature up to 70°C. The MMT weight fraction was approximately 5.0×10^{-5} in these samples.

Because DLS theory for platelet-shape particles is not well understood, a quadratic cumulants method with an intensity autocorrelation function was used to "fit" the MMT as polydisperse spheres. This determines the z-average translational diffusion coefficient, which is then used in the Stokes-Einstein equation to compute the equivalent "hydrodynamic diameter" of the MMT nanoplatelets.

Thermal Properties

Differential scanning calorimetry (DSC) and thermogravimetric analysis (TGA) were used to evaluate the thermal properties of nanocomposite films. For DSC (Q2000, TA Instruments), approximately 5 mg of sample (cast film dried at 40°C) was tightly packed into a Tzero aluminum pan (TA Instruments) and then sealed. Two identical heating/cooling cycles (40-240°C, 10°C/min scan rate) were conducted under nitrogen purge. For TGA (Q5000, TA Instruments), approximately 8-10 mg of sample (cast film dried at 40°C) was placed onto a high-temperature platinum pan (TA Instruments) and heated in air to 800°C at a scan rate of 10°C/min.

Mechanical Properties

Dynamic Mechanical Analysis (DMA) was used to characterize nanocomposite mechanical properties (RSA-III, TA Instruments). Samples of drawn films were cut into strips (47-49 mm length, 6-7 mm width, 20-30 μm thickness) and then dried in a vacuum oven at 60°C for 24 h. Specimens were carefully mounted in the tensile testing fixture followed by zeroing the pre-tension, heated to 140°C, and held at that temperature for 5

min. Complex tensile modulus was measured during a temperature sweep from 140°C to -80°C (-3°C/min ramp rate, 1.0 Hz frequency, 0.05% strain amplitude). At least three specimens of each nanocomposite were tested.

Gas Permeability

The gas barrier properties of nanocomposite polymer films were measured using a custom-built gas permeation system (Figure 3.1). The main components of the permeation system are a continuous-flow permeation cell, a variable leak valve, and a quadrupole mass spectrometer (SRS100, Stanford Research Systems). After drying in a vacuum oven at 60°C for at least 24 h, a drawn film was masked on both sides using heavy-duty aluminum foil sealed with high vacuum grease, leaving exposed a circular area of about 5 cm^2. The masked film was seated and sealed in the permeation cell. One side was exposed to the test gas, water vapor at 36.5°C at >97% relative humidity. A carrier gas (N$_2$) flowed at a controlled mass flow rate over the other side, carrying the permeate gas into the mass spectrometer for measurement of the permeate concentration. A mass balance yields the water vapor transmission rate (WVTR). For each nanocomposite, WVTR was measured for at least three replicate film specimens.
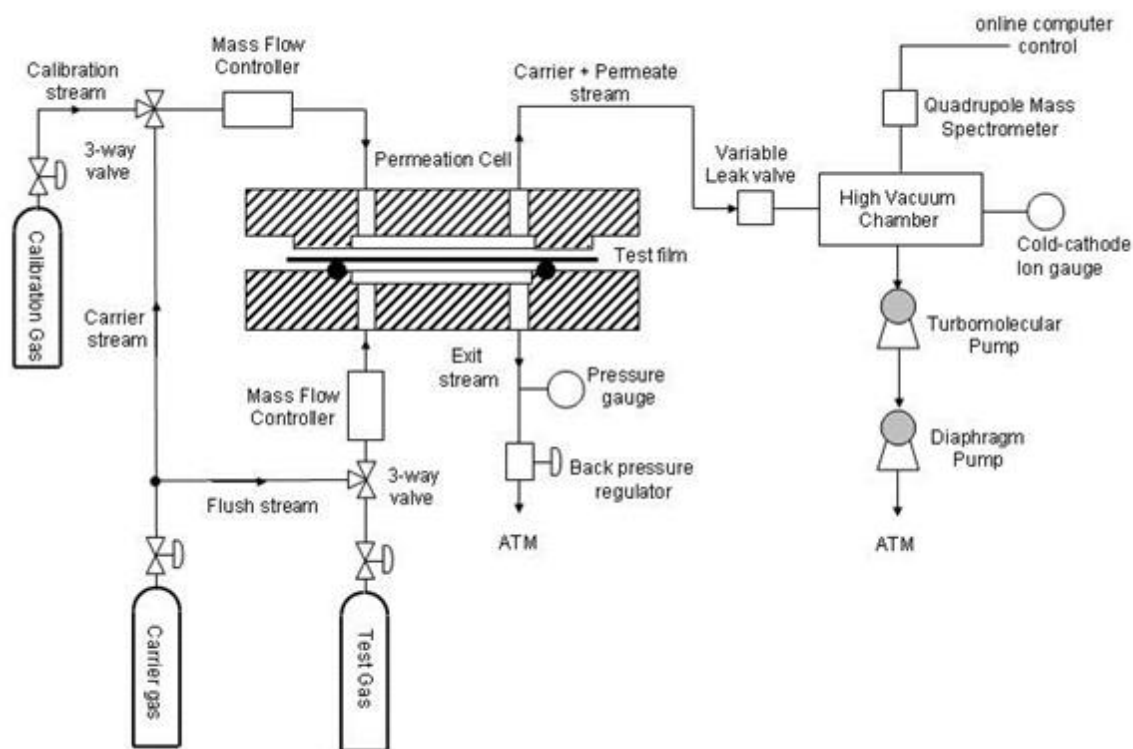
Figure 3.1. Schematic diagram depicting our custom-built equipment for measuring gas permeation through polymer films.

Referring to Figure 3.1, film samples are mounted in the permeation cell consisting of two metal halves sealed by an O-ring and clamped tightly by nuts and bolts. Each metal half has a shallow circular cavity in its center. Two chambers are formed after a test film is mounted between the two metal halves. During operation, one of the chambers is supplied with the test gas, while the carrier gas continuously sweeps the other. Both the test gas pressure and the carrier gas flow rate are precisely controlled. The permeant, i.e., the test gas that has permeated through the test film, is fully mixed

into the carrier gas stream leaving the permeation cell. The gas permeation rate $J(t)$ is given by:

$$J(t) = C(t) \cdot q / A \qquad (1)$$

where $C(t)$ is the concentration of the test gas in the effluent carrier gas stream at any instant t, q is the carrier gas flow rate, and A is the permeation area.

A small amount of the effluent carrier gas stream is leaked into the high vacuum chamber at a controlled rate with the aid of a variable leak valve, while the rest is vented. Determination of $C(t)$ is made viable by exploiting the fact that under high vacuum, the characteristic mass-to-charge (m/z) peak generated by the mass spectrometer for a gas species changes linearly with the change of its partial pressure. The instrument's sensitivity factor for a gas g, denoted as S_g, is defined as:

$$S_g = \frac{I_g}{p_g} \qquad (2)$$

where I_g denotes the principal mass-to-charge peak and p_g denotes the partial pressure. This sensitivity factor is fairly constant when the total vacuum pressure is below 10^{-5} torr. Dalton's law relates the partial pressure to concentration, assuming that the vacuum environment is dominated by the carrier gas. The total vacuum pressure is referenced from a cold-cathode ionic gauge also attached to the high vacuum chamber. Combining (1) and (2), the gas permeation rate is given by:

$$J_g(t) = \frac{q}{A} \frac{I_g(t)/S_g}{p_{vac}} \qquad (3)$$

where p_{vac} is the total vacuum pressure. By definition, the permeability of a film is:

89

$$P_g = \frac{J_g \cdot l}{\Delta p_g} \tag{4}$$

where J_g is the steady-state permeation rate, l is the film thickness, and Δp_g is the applied partial pressure difference across the film.

The permeation apparatus described here was tested for the case of carbon dioxide permeation. The specimen films were one-mil thick Mylar® PET supplied by Eastman Chemical Company. The carrier gas was 99.9995% pure argon and the test gas was 99.5% pure carbon dioxide, both from National Welders. Three measurements were made using the specimens from the same film. The relative standard deviation among the measurements was $\leq 2\%$. The permeability results were then compared with measurements obtained on a MOCON® instrument. The differences were found to be within 6% of the MOCON® measurement.

In this work, the carrier gas was nitrogen and the test gas was either oxygen or water vapor. The sensitivity factor for oxygen was determined by calibration using a certified gas mixture of 2000 ppm oxygen in carbon dioxide. For comparison purposes, all permeation tests for a given test gas (oxygen or water vapor) were performed under the same conditions. Specifically, for oxygen permeation tests, the vacuum pressure was approximately 2.5×10^{-6} mbar, the applied oxygen pressure difference was 1 atmosphere, and temperature was ambient (23~25°C). All films for oxygen permeation testing were dried in vacuum at ~80°C for ≥ 24 hours and conditioned in argon overnight prior to testing. TGA results indicated that the films were $\geq 99\%$ dry after vacuum-drying.

For water permeation tests, the sensitivity of the instrument to water was calibrated using a humidified stream of saturated nitrogen gas. The principal mass-to-charge ion peak of water at m/z = 18 was monitored during the tests. The vacuum pressure was approximately 1.0×10^{-6} mbar, the water partial pressure difference was 6150 Pa, and temperature was fixed at 25°C.

3.4. Results and Discussion

3.4.1. "Ideal" MMT/PVOH Nanocomposites

Previous research [165] has established purification procedures (described above) that produce suspensions of almost completely exfoliated montmorillonite (MMT) platelets, as verified by AFM (Figures 3.2 and 3.3). Our previous research [185] describes the use of AFM for quantitative analysis of the size distribution of exfoliated MMT platelets. For every individual "particle" in each AFM image, we can measure the vertical dimension relative to the background at every point on each particle. The average value of the vertical dimension is the mean thickness of that particle. Based on the typical lateral dimensions seen in the AFM images (10's to 100's of nm) and the median thickness of 1.20 nm, these particles are clearly platelets. The median thickness of 1.20 nm is consistent with the expected thickness of hydrated MMT platelets.

About 83% of the particles seen in the AFM images have mean thicknesses between 0.9 nm and 1.5 nm: these are pristine single platelets. If one defines exfoliation as the production of pristine single platelets, then we would say that this sample is 83% exfoliated. About 15% of the particles have mean thicknesses between 1.6 and 2.5 nm.

91

Typically, these are single platelets with all or part of a second platelet on top (see inset of Figure 3.2). Even pristine single platelets are often observed to have small fragments somewhere on their top surface. If the second platelet fragment is large, it may cover most of the surface of the platelet underneath. This can be called a duplex stack (two platelets). Strictly speaking, these platelets are not exfoliated. However, we can say that 98% of the MMT particles in this sample are exfoliated into either single platelets or duplex stacks. We do not see a significant incidence of duplex stacks that appear to be created due to the random deposition of one pristine single platelet overlapping part of another single platelet.
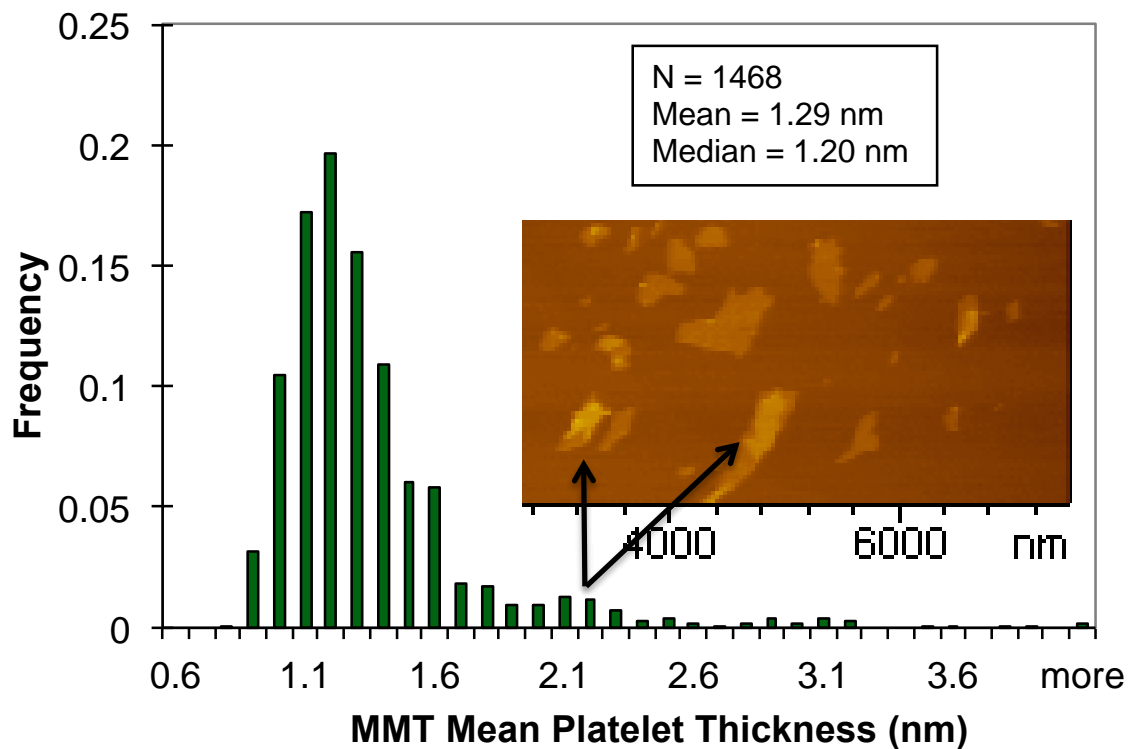
Figure 3.2. Histogram of mean MMT platelet thicknesses based on N=1468 particles from 39 different AFM images [185]. The inset shows a part of one AFM image showing mostly pristine single platelets; the arrows point to two particles that are probably unexfoliated duplex stacks.

For every individual particle in each AFM image, image analysis gives us the lateral area in nm^2 [185]. We compute a characteristic lateral length for each particle as the square root of the measured area. The particle's aspect ratio equals the characteristic lateral length divided by the mean thickness of that individual particle. In this way, we can measure the exact aspect ratio of every particle in an AFM image. The aspect ratios of N=1468 particles are compiled in the histogram of Figure 3.3. The mean and median aspect ratios are 159 and 142, respectively. Multiplying these values by the median

platelet thickness (1.20 nm) gives an "average" platelet length between 191 and 170 nm. The measured aspect ratio distribution may be used in conjunction with a recent version of the tortuous path model [176] to estimate the gas barrier performance of PNC films containing platelets with considerable size polydispersity.
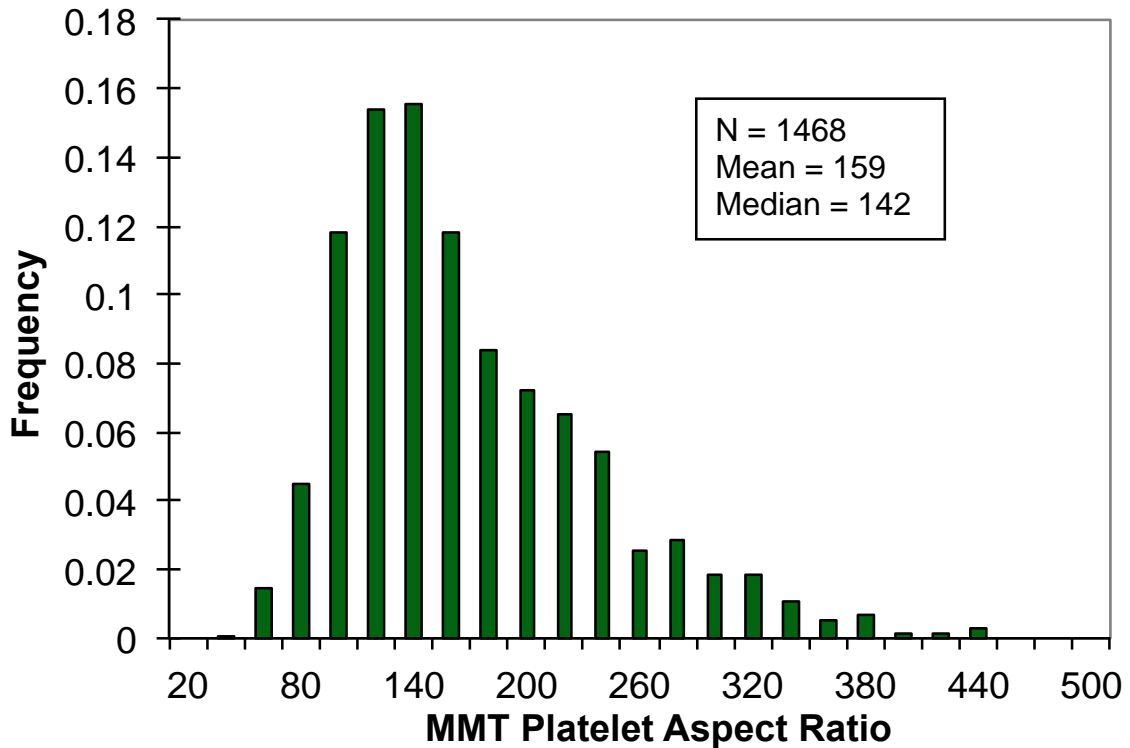
Figure 3.3. Histogram of MMT platelet aspect ratio based on N=1468 particles from 39 different AFM images [185].

This work began with two initial hypotheses. The first was that "ideal" MMT/PVOH nanocomposites prepared from suspensions of fully exfoliated MMT platelets should exhibit superior gas barrier performance compared to that reported previously [155, 158, 160-161]. Second, by properly accounting for platelet polydispersity, the tortuous path model [176] should be able to rationalize the measured gas barrier performance of our supposedly "ideal" MMT/PVOH nanocomposites.

To this end, we prepared a series of MMT/PVOH nanocomposite films with varying MMT loadings and measured their oxygen permeabilities. Figure 3.4 plots this data in terms of the O_2 barrier factor (the O_2 permeability of pure PVOH divided by that of a MMT/PVOH nanocomposite), along with predictions of the tortuous path model [176] based on the MMT platelets' measured aspect ratio distribution (Figure 3.3). The O_2 barrier factor rises monotonically with MMT loading but falls substantially below the prediction of the tortuous path model for fully exfoliated platelets (curve denoted by n=1). If we use the same aspect ratio distribution but assume that the dispersed particles are aggregated platelet "stacks" with an average of four platelets each (curve denoted as n=4), the model prediction rationalizes the barrier data up to 5 wt% MMT, but significantly over-predicts barrier performance at higher MMT loadings.
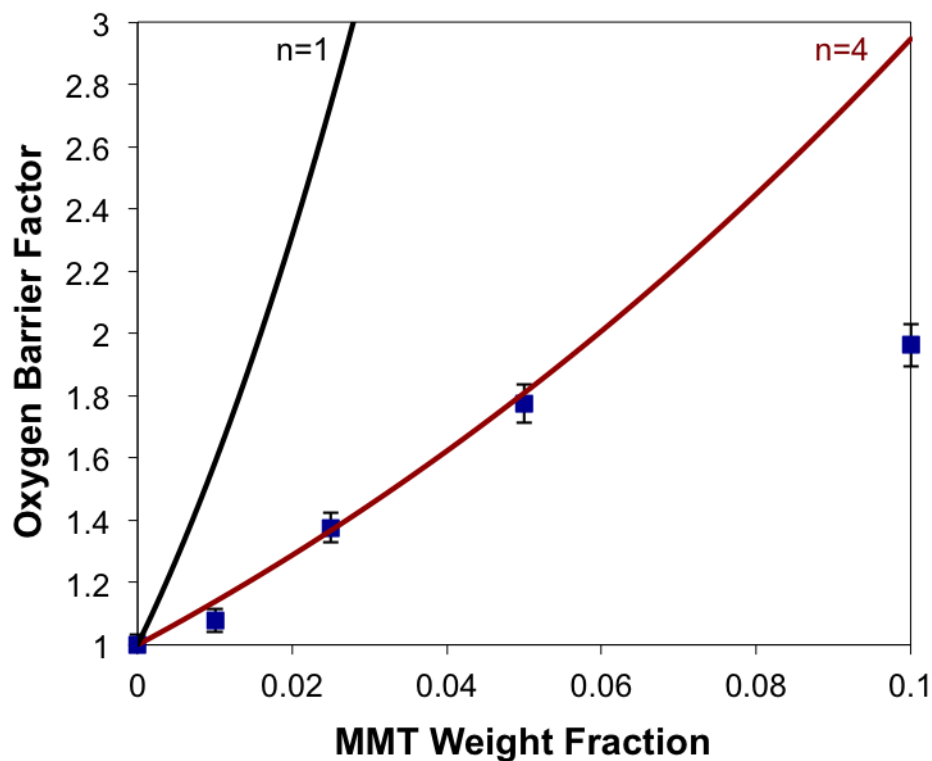
Figure 3.4. Oxygen barrier factor (symbols) for MMT/PVOH nanocomposites as a function of MMT loading (95 kDa PVOH matrix). The solid curves are calculated via the tortuous path model for polydisperse platelets [176] based on the aspect ratio distribution measured for this MMT by AFM (Figure 3.3). Labels denote calculations assuming full exfoliation (n=1) and partial aggregation into stacks containing an average of four platelets (n=4).

The O_2 barrier data and comparisons with model predictions essentially invalidate both of our initial hypotheses. Although the increase in O_2 barrier with MMT loading agrees with expectations, measured barrier performance is not superior to that observed previously. Moreover, the differences between measured and predicted barrier performance indicate flaws in the assumptions of the tortuous path model, flaws in our concept of "ideal" MMT/PVOH nanocomposites (i.e., that we could prepare fully-

exfoliated PNCs by blending verified, fully-exfoliated platelet suspensions with solutions of compatible polymer), or both.

TEM images give qualitative indications of non-idealities in structure that arise during solution blending, solvent evaporation, and film densification. Away from the surfaces of a 10 wt% MMT/PVOH composite film, we observe regions of what appear to be face-aggregated platelets in addition to regions of well-dispersed, individual platelets (Figure 3.5a). Other TEM images (Figure 3.6) show similar regions in both 1 wt% and 10 wt% MMT/PVOH composites. This shows that although MMT platelets are fully exfoliated in the starting stock suspension, they undergo at least partial aggregation during solution blending, solvent evaporation, and film densification. Near the film surface, we observe what appears to be a wrinkled region of layered, consolidated platelets (Figures 3.5b and 3.7). The wrinkling could be caused by stresses generated either during densification or microtoming. Regardless, the observed platelet consolidation should not occur if the densification process only involves water removal from a uniform mixture of PVOH and exfoliated MMT platelets. Both platelet aggregation and surface consolidation provide evidence for some kind of platelet-platelet attraction that arises during solution blending, solvent evaporation, and film densification.
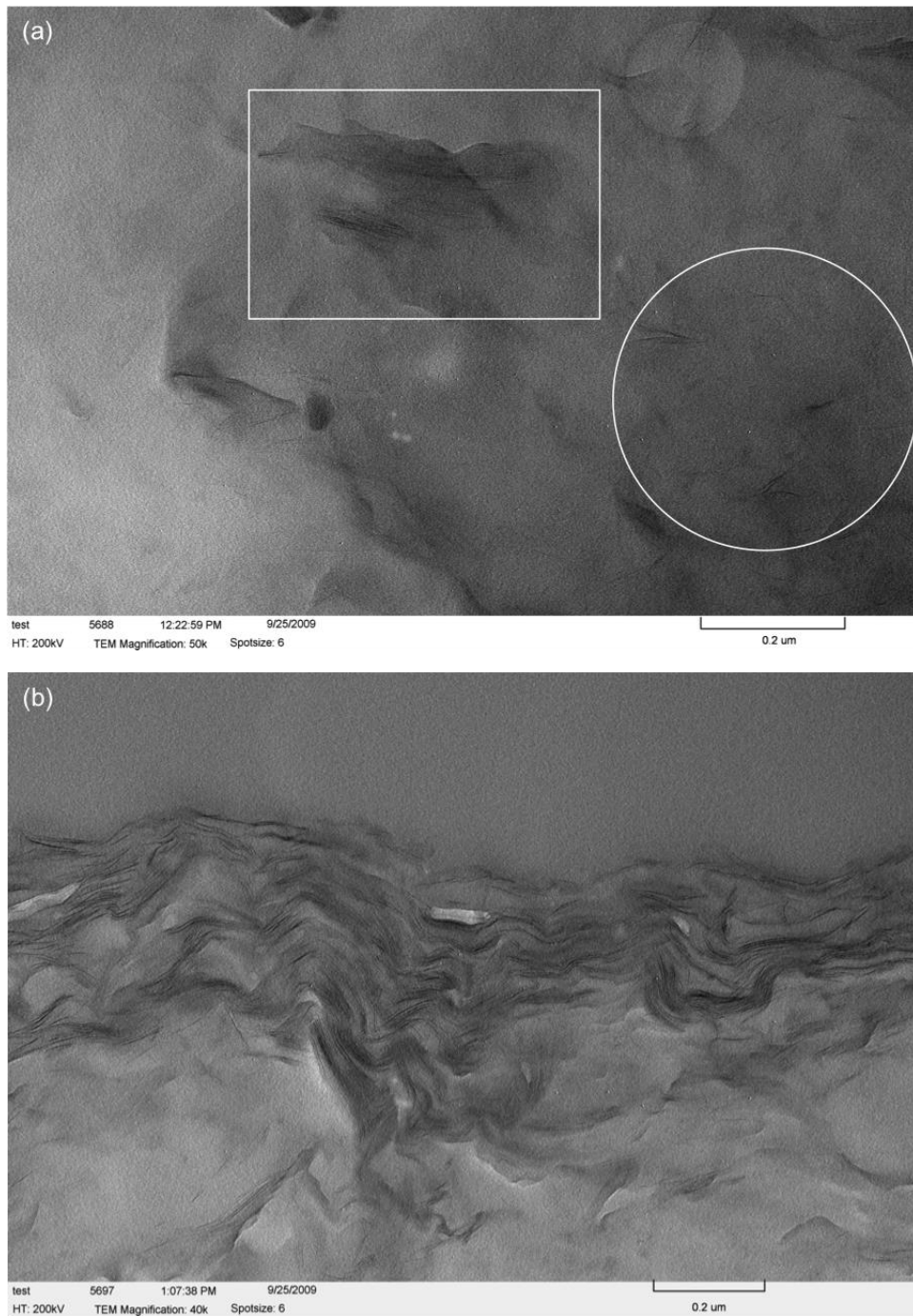
Figure 3.5. TEM images of a 10 wt% MMT/PV$_{95}$ nanocomposite. (a) Interior region with indicated areas containing well-dispersed platelets (circle) and face-aggregated platelets (rectangle). (b) Surface region showing a wrinkled "skin" of consolidated platelets.

Figure 3.6. TEM images of interior regions in MMT/PVOH nanocomposites (see below).

test 5705 2:20:15 PM 9/25/2009
HT: 200kV TEM Magnification: 9k Spotsize: 6 1 um
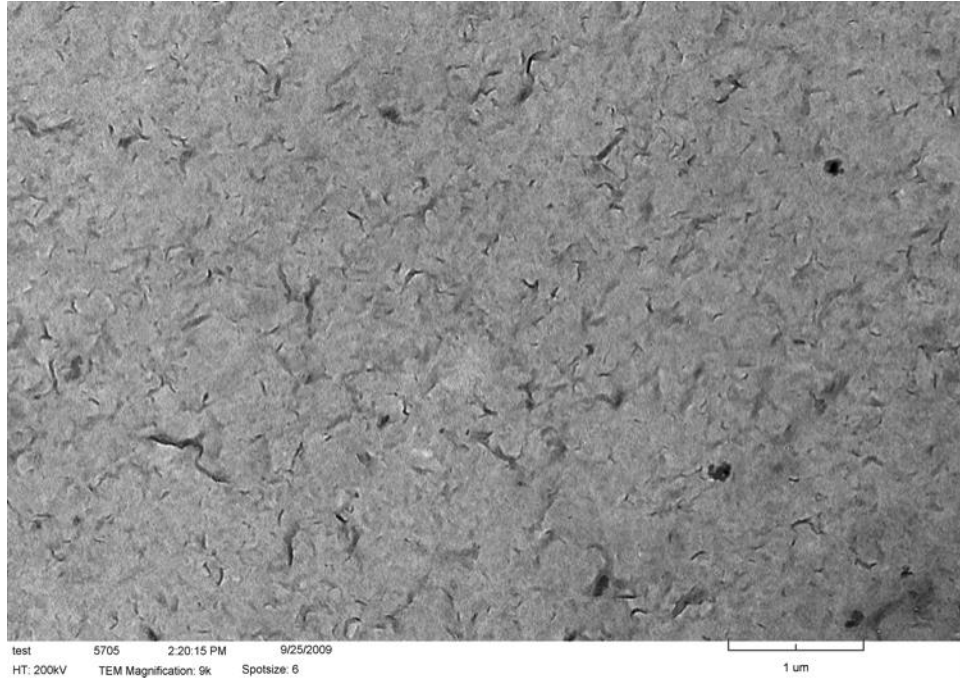
(a) Low magnification image for 1 wt% MMT/PVOH (092509-PVOH-1wt%MMT#2E.tif).

(b) High magnification image for 1 wt% MMT/PVOH (092509-PVOH-1wt%MMT#5E.tif).
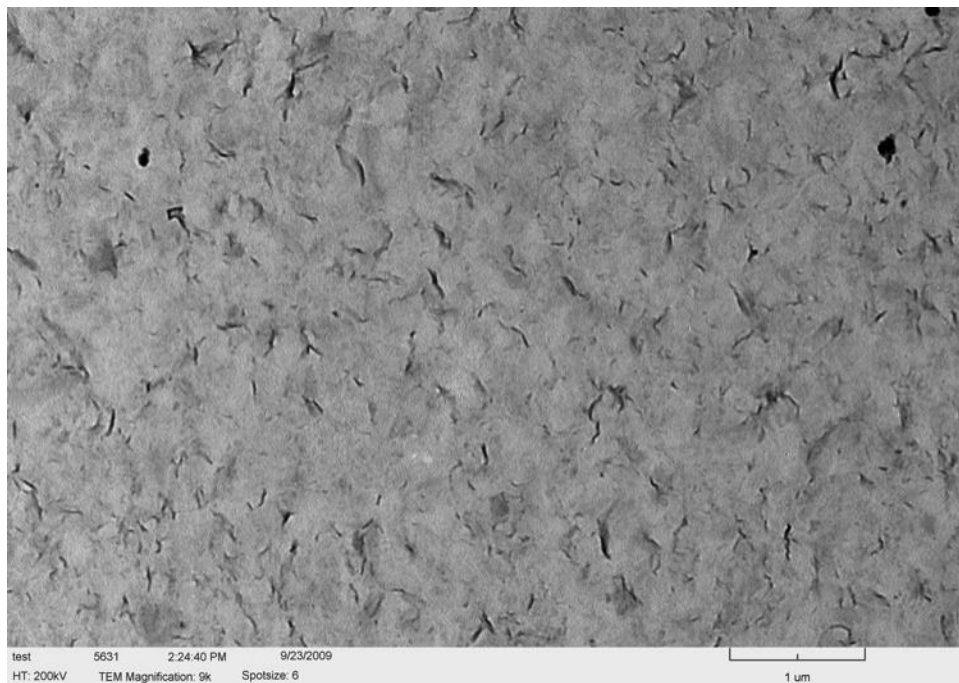
(c) Low magnification image for 10 wt% MMT/PVOH (092309-PVOH10wt%MMT_9K#4.tif).
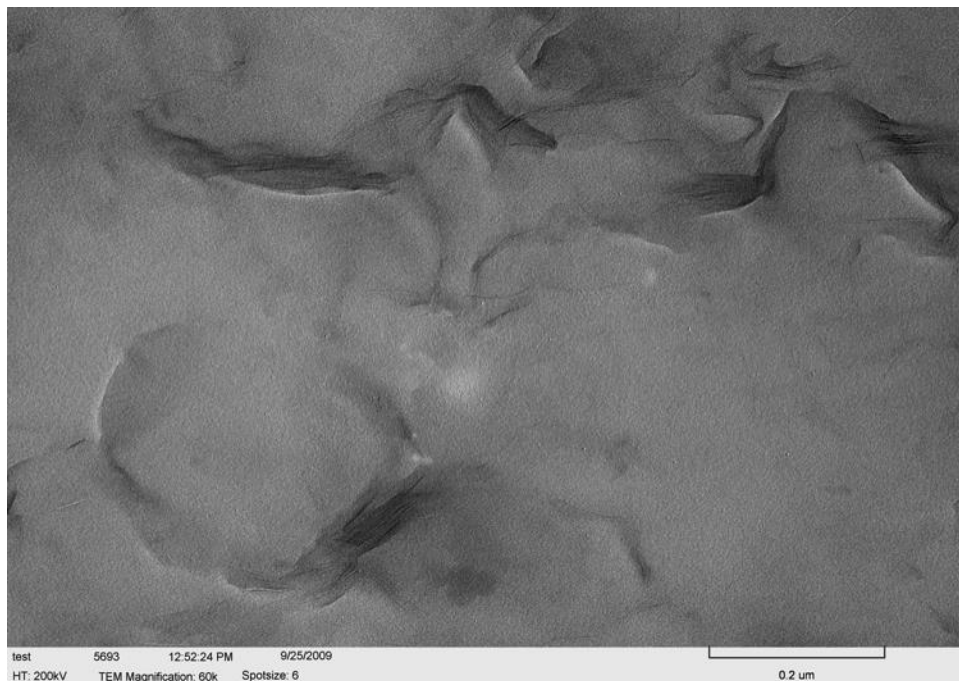
(d) High magnification image for 10 wt% MMT/PVOH (092509-PVOH-10wt%MMT#5.tif).

Figure 3.7. TEM images of surface regions in MMT/PVOH nanocomposites (see below).
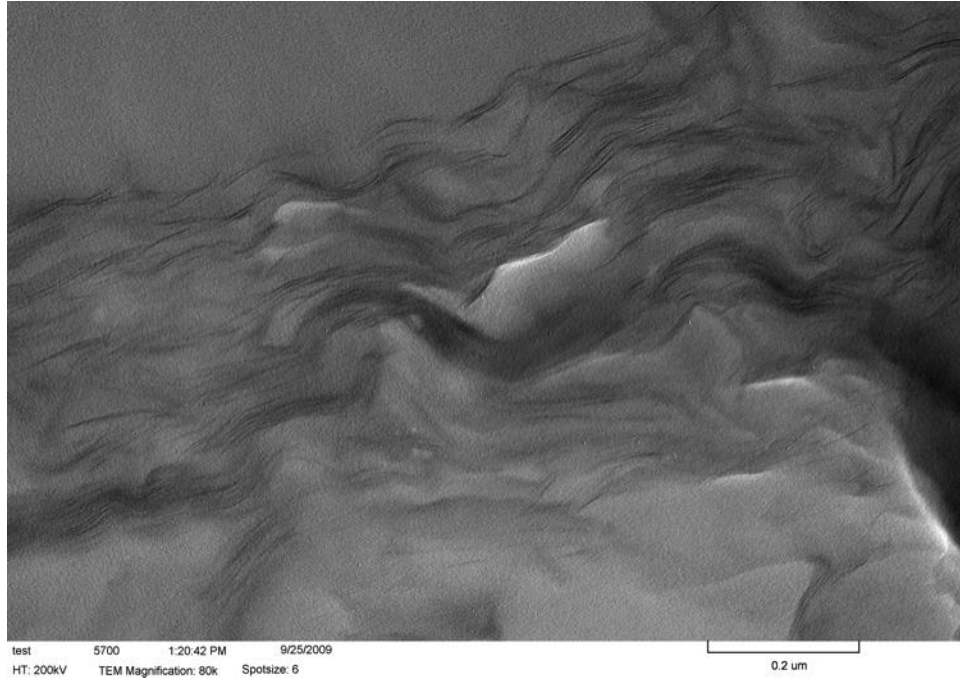
(a) Low magnification image for 10 wt% MMT/PVOH (092509-PVOH-10wt%MMT-80kX).
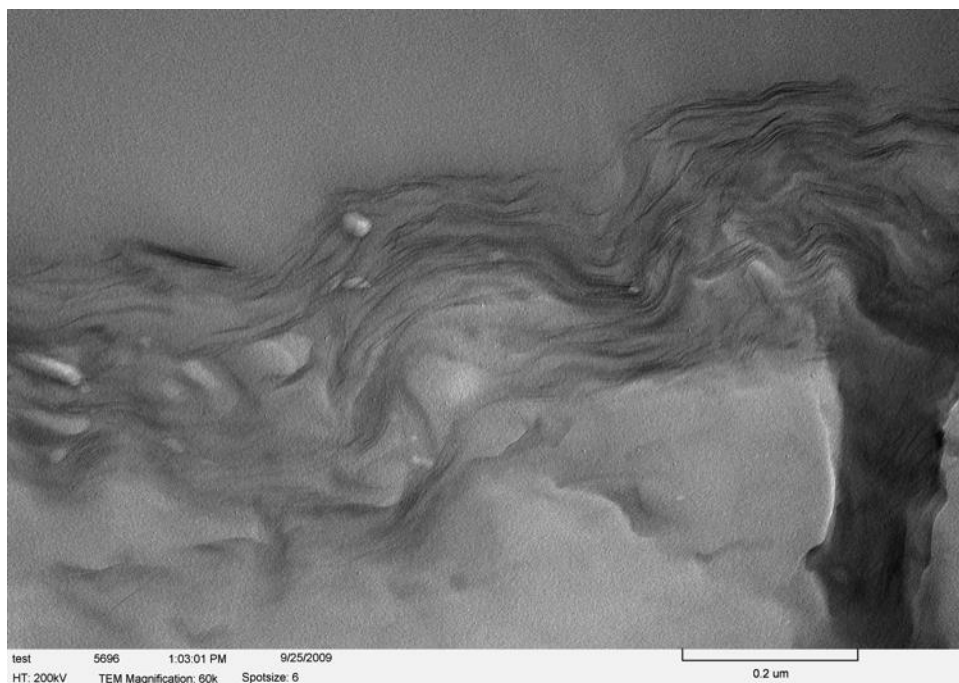
(b) Medium magnification image for 10 wt% MMT/PVOH (092509-PVOH-10wt%MMT#6E).
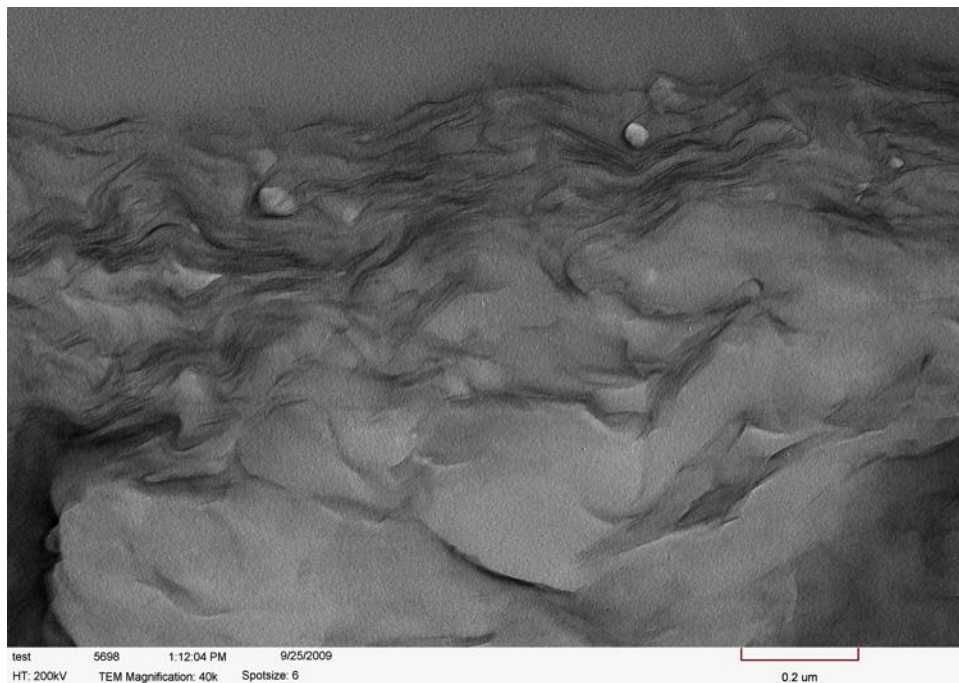
(c) High magnification image for 10 wt% MMT/PVOH (092509-PVOH-10wt%MMT#8E).

PVOH readily adsorbs onto MMT in water [166-172]. This suggests that PVOH-mediated bridging attraction might lead to MMT aggregation during the solution blending process. Dynamic light scattering data provide some evidence for this. For diluted MMT stock suspensions (MMT, Figure 3.8), the measured particle size is about 186 ± 9 nm, independent of the MMT concentration after dilution. This DLS particle size agrees well with the platelets' characteristic lateral dimension as measured by AFM (Figure 3.3). MMT stock suspension was then mixed with PV_{205} solution to produce a blend suspension (MMT+PV_{205}, Figure 3.8) containing about 0.28 wt% MMT and 5.0 wt% PVOH. After dilution to the indicated MMT concentrations, the particle size measured by DLS ranged from 284 to 368 nm (average 317 ± 38 nm) with larger polydispersity indices. The greater particle size (compared to the starting MMT) results from a combination of PVOH adsorption and platelet aggregation due to polymer bridging.
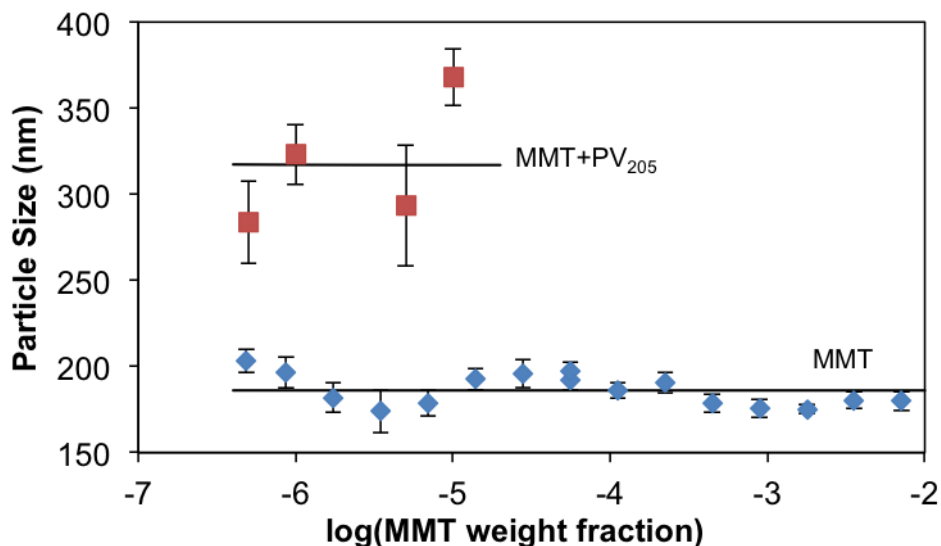
Figure 3.8. MMT particle size as measured by DLS. MMT: MMT stock suspension diluted to the indicated MMT weight fraction. MMT+PV$_{205}$: MMT stock suspension mixed with PV$_{205}$ solution to produce a blend suspension containing 0.28 wt% MMT and 5.0 wt% PV$_{205}$, and then diluted to the indicated MMT weight fraction.

3.4.2. MMT Platelet Pretreatment

The previous results lead to the third hypothesis investigated in this work: that initially coating MMT platelets with a protective layer of polymer may reduce bridging attraction between platelets, promote better platelet dispersion, and improve the properties of MMT/PVOH nanocomposites. We refer to this preliminary coating as "pretreatment", considering that the platelets will subsequently undergo blending with PVOH matrix polymer and then densification to form MMT/PVOH nanocomposites.

To test this hypothesis, we seek a pretreatment polymer that readily adsorbs onto MMT, has good compatibility with the PVOH matrix, and does not itself produce

bridging aggregation. High molecular weight PVOH (such as PV_{205}) should adsorb strongly and provide a thick steric barrier, but it also may promote bridging aggregation (Figure 3.8). For this reason, we focused on two lower molecular weight pretreatments: PV_{11} and F108 Pluronic$^{®}$, a PEO-PPO-PEO triblock copolymer. The polymer concentration used in pretreatment should maximize adsorption and thus the effectiveness of the steric barrier. On the other hand, if the pretreatment polymer concentration is too high, then its concentration in the final polymer nanocomposite will be too high, as well (see Appendix A for details).

MMT was pretreated with PV_{11} by adding MMT stock suspension to PV_{11} solutions, producing PV_{11}MMT suspensions with varying PV_{11} concentration. The MMT particle size was measured by DLS after dilution with DI water (Figure 3.9). For the pretreatment suspension containing 0.1 wt% PV_{11}, the large apparent particle size clearly indicates MMT aggregation. In this case, PV_{11} acts as a flocculent: the low concentration results in only partial coverage of the MMT surface, enabling PV_{11} bridging that leads to MMT aggregation. For PV_{11}MMT suspensions with 0.25 wt% and higher PV_{11} concentrations, the MMT particle size is consistently about 25% higher than that in the MMT stock suspension. As in the case of MMT+PV_{205} (Figure 3.8), the larger effective particle size may be due to a combination of PV_{11} adsorption (producing larger hydrodynamic drag on the diffusing PV_{11}MMT platelets) as well as low levels of MMT aggregation. However, the higher PV_{11} concentrations clearly do not result in large-scale MMT flocculation.
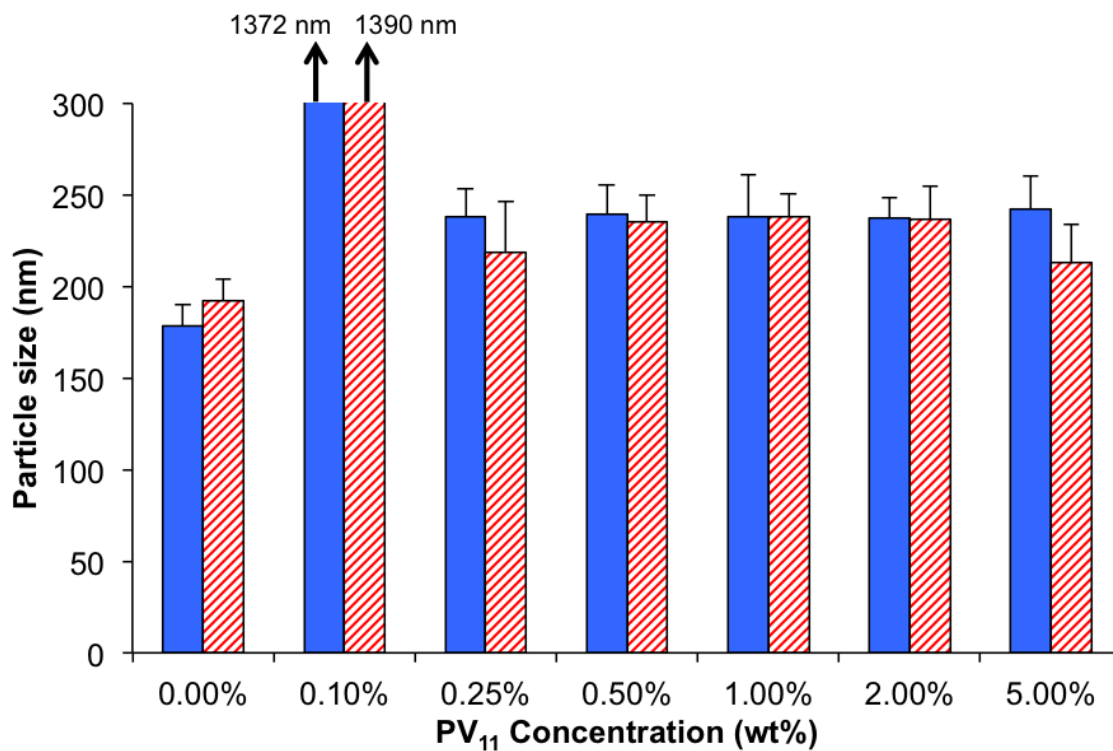
Figure 3.9. MMT particle size, as measured by DLS, in suspensions containing various concentrations of PV_{11}. Suspensions were diluted with DI water to MMT weight fractions of 1.0×10^{-5} (solid bars) or 5.0×10^{-6} (hatched bars).

Among the PV_{11} solutions listed in Figure 3.9, the pretreatment suspension containing 0.50 wt% PV_{11} was selected for preparing nanocomposites in subsequent solution blending. Depending on the MMT weight fraction in the starting MMT stock suspension, this pretreatment suspension typically contained 30-40 wt% MMT (on a solids basis) with the balance as PV_{11}. These quantities must be taken into account in subsequent solution blending to achieve the target MMT loading (10.0 wt%) in the final composite (see Appendix A for details).

In addition to PV_{11}, PV_{95} and PV_{205} as well as F108 Pluronic$^{®}$ were also explored for pretreating the MMT surface. DLS characterization was used to measure MMT particle size in these pretreatment suspensions (Figure 3.10). For MMT pretreated with F108 at concentrations of 0.1% and 0.5% (F-MMT), the measured MMT particle sizes were approximately 150 nm, essentially identical to that of the MMT stock suspension. This indicates that F108 pretreatment does not lead to MMT aggregation. We elected to use 0.1% F108 for pretreatment to avoid any complications due to micelle formation [188]. For the MMT pretreated with 0.5% PV_{95} or PV_{205}, DLS results gave an average particle size of 235 nm. This suggests that these higher molecular weight polymers produced some polymer bridging that resulted in some MMT aggregation. Because of this, PV_{95} and PV_{205} were not studied further for use in MMT pretreatment.
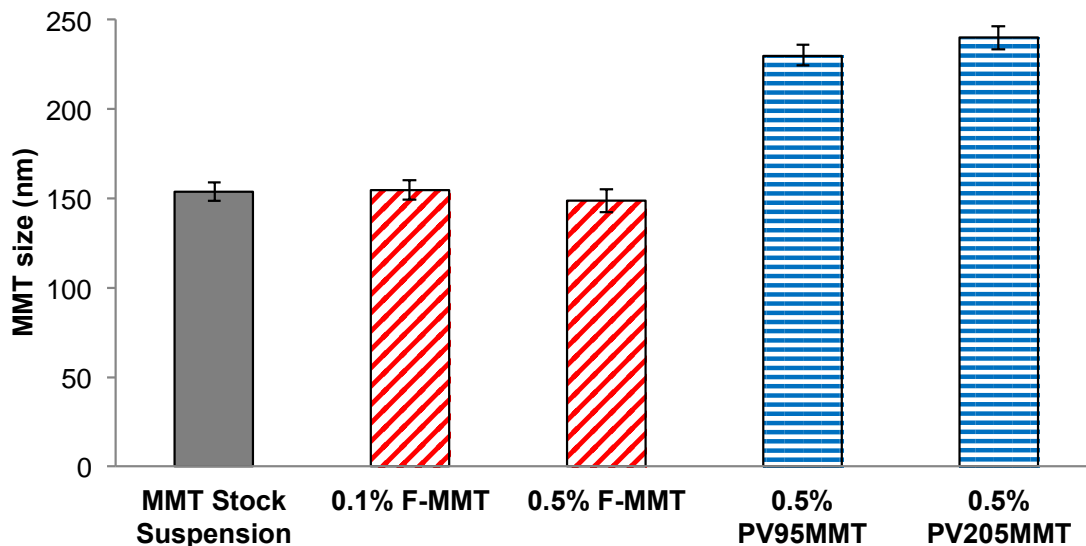
Figure 3.10. MMT particle size as measured by DLS for various pretreatment suspensions, including F108 (F-MMT), PV_{95}, and PV_{205}, at indicated concentrations. Suspensions were diluted with DI water to a MMT weight fraction of 5.0×10^{-6}.

Next, we assess the extent to which pretreatment using PV_{11} or F108 prevents polymer bridging during solution blending. Figure 3.11 shows the effect of solution blending on the apparent size of MMT particles, expressed as percentage change relative to the MMT particle size in the starting stock suspension for each set of experiments. For the pretreatment suspensions, the average particle sizes in PV_{11}MMT and F-MMT are about 30% and 0.5% greater, respectively, than that in MMT stock suspension. This may indicate some bridging aggregation in PV_{11}MMT suspension, which is not observed in F-MMT suspension.

Blending untreated MMT stock suspensions with PVOH solutions results in significant increases in apparent particle size, ranging from 67% for MMT+PV_{11} to 160%

for MMT+PV$_{205}$. This indicates a strong tendency of PVOH to induce bridging aggregation of untreated MMT, which increases with polymer molecular weight. For pretreated PV$_{11}$MMT suspension blended with PVOH solutions, the particle size only increases from 40% to 56% with increasing PVOH molecular weight. Thus, PV$_{11}$ pretreatment seems to reduce the incidence of bridging aggregation during solution blending of PV$_{11}$MMT suspension with PVOH solutions. The dependence on the PVOH molecular weight is weak. Although thermodynamically favored, PV$_{95}$ and PV$_{205}$ do not displace previously-adsorbed PV$_{11}$ from the MMT surface on the time scale of these experiments.
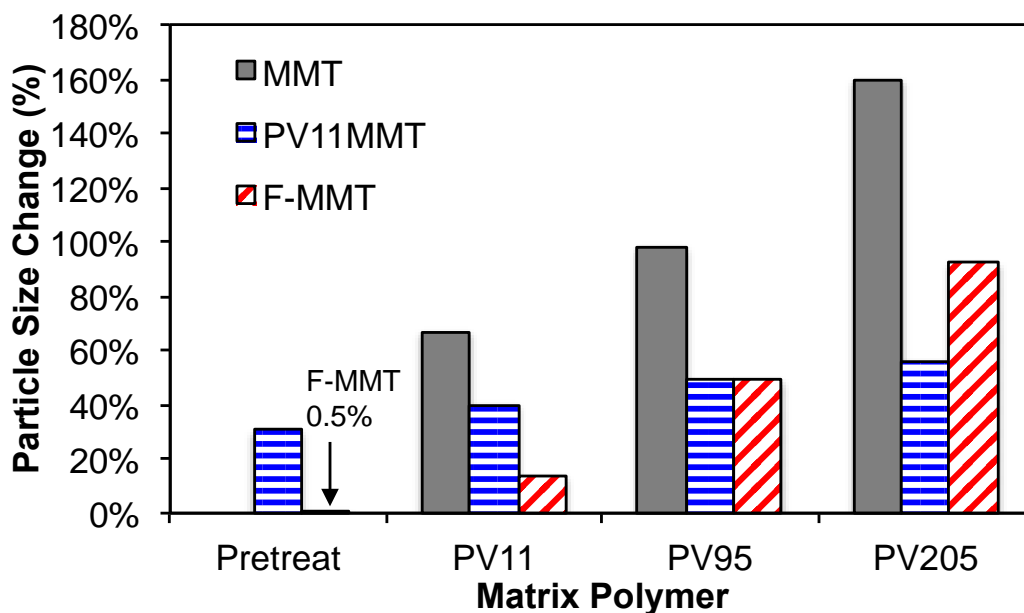
Figure 3.11. Percentage change in apparent particle size (relative to untreated MMT in stock suspension) for particles in pretreatment suspensions ("pretreat") and MMT+PVOH blend suspensions (2 wt% polymer) with various PVOH molecular weights (PV_{11}, PV_{95}, and PV_{205}). The legend indicates results for untreated MMT and pretreated PV_{11}MMT and F-MMT. All samples for DLS were diluted with DI water to an MMT weight fraction of 5.0×10^{-6}.

We observe a similar trend for solution blending of pretreated F-MMT suspension with PVOH solutions, but the molecular weight dependence is more pronounced (14%, 49%, and 92% particle size increase upon blending F-MMT with PV_{11}, PV_{95}, and PV_{205} solutions, respectively). We infer that PV_{11} does not readily displace "pre-adsorbed" F108 from the surfaces of F-MMT platelets. On the other hand, higher molecular weight PV_{205} appears to be more effective at displacing F108 from the F-MMT surface, resulting in a higher incidence of bridging aggregation. Overall, these results suggest that F108 may be preferable for pretreating MMT to prevent bridging if the molecular weight of the

113

PVOH matrix is low. If the molecular weight of the PVOH matrix is high, then PV_{11} is preferable for preventing MMT bridging aggregation during solution blending.

3.4.3. MMT/PVOH Nanocomposite Properties

3.4.3.1. Structural Characterization

XRD measurements provide information on structure within MMT/PVOH nanocomposites, including the effect of MMT on PVOH crystallinity and the incidence of platelet restacking. Figure 3.12 shows XRD patterns for the starting MMT powder, neat PV_{95} film, and various 10 wt% MMT/PV_{95} composites. Plots for neat PV_{11} and PV_{205} films and their MMT nanocomposites are shown in Figures 3.13 and 3.14. The pattern for MMT powder features a prominent (001) peak centered at 7.38°, corresponding to a layer spacing of 1.20 nm, as expected. The pattern for neat PV_{95} film has a broad peak centered at 19.6° that is typically associated with semicrystalline PVOH structure [155, 156, 159, 164]. The patterns for all of the MMT/PVOH nanocomposites (Figure 3.12) are similar. First, none of the composite patterns show evidence of a peak near 7.4° associated with the layered MMT structures, nor any peaks at lower angles due to expanded or restacked MMT platelets. All of the composite patterns display weak peaks centered near 9.3°, which we believe to be associated with surface-induced nucleation of additional PVOH crystallites. This peak has been observed previously [164, 172, 189], but (in one case) misinterpreted in terms of MMT layer expansion [164]. Our observations suggest that composites prepared with pretreated MMT probably have structures similar to that seen in untreated MMT/PVOH composites.
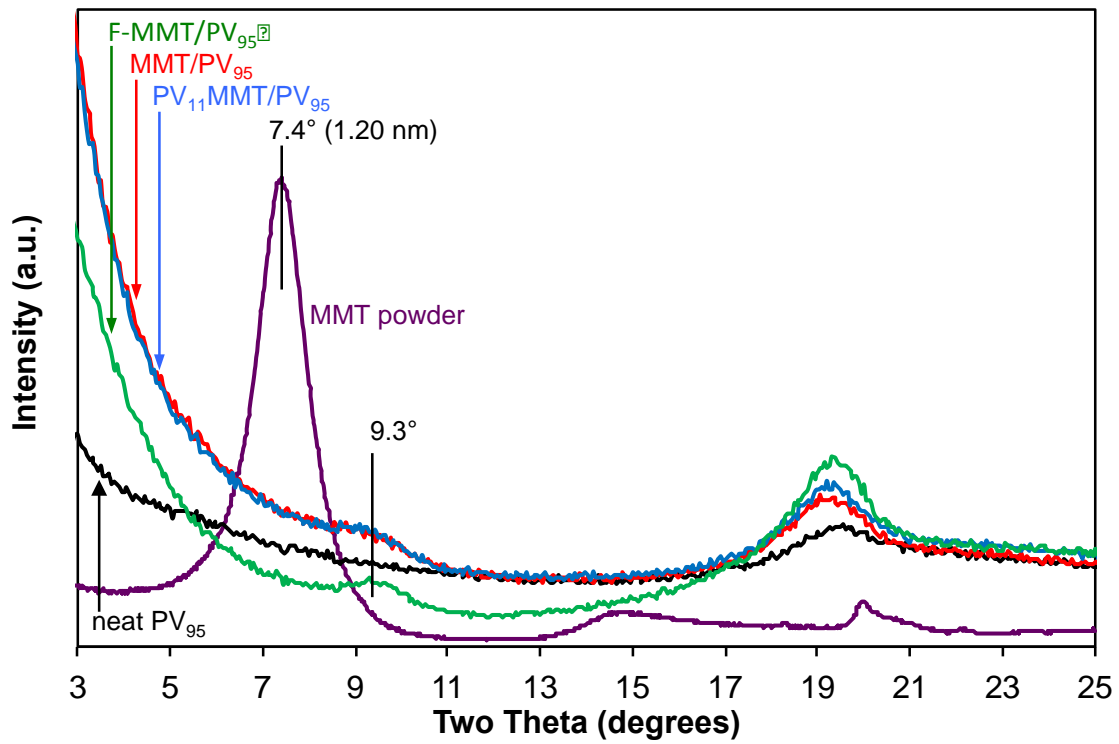
Figure 3.12. XRD patterns for starting MMT powder, neat PV_{95} film, and various 10 wt% MMT/PV_{95} composites as labeled in the plot. The intensity upturn at low angles is due to the underlying glass slide used to mount the polymer films for XRD.
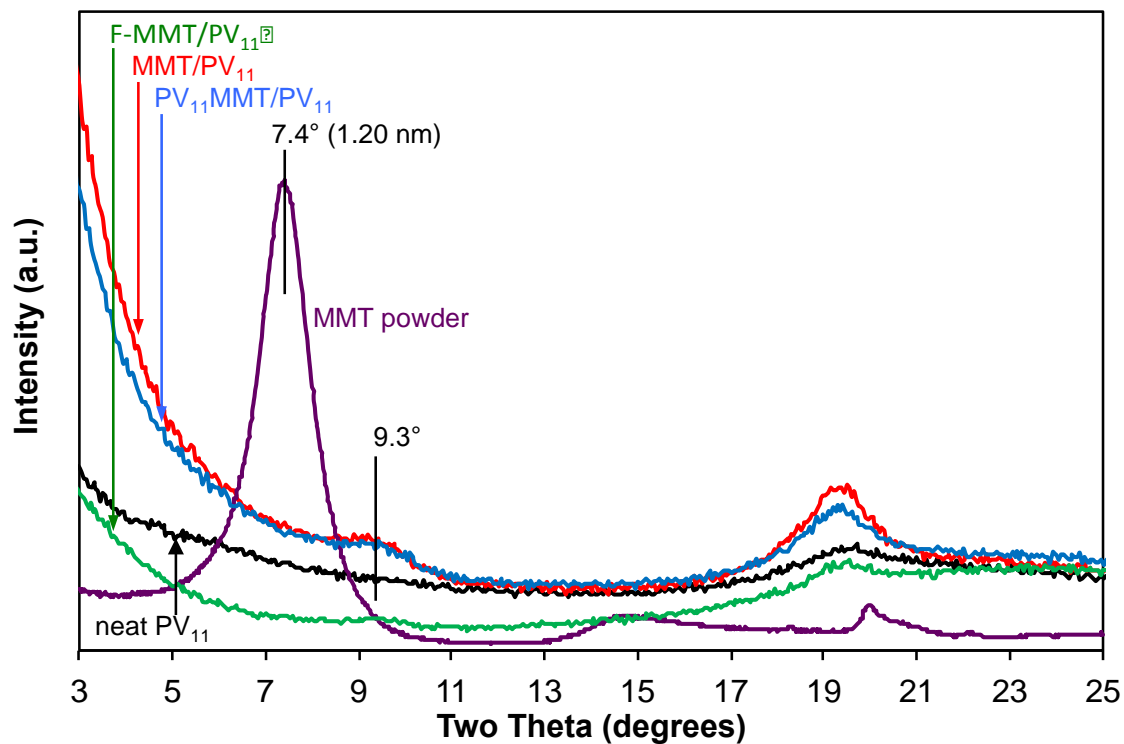
Figure 3.13. XRD patterns for starting MMT powder, neat PV_{11} film, and various 10 wt% MMT/PV_{11} composites as labeled in the plot. The intensity upturn at low angles is due to the underlying glass slide used to mount the polymer films for XRD.
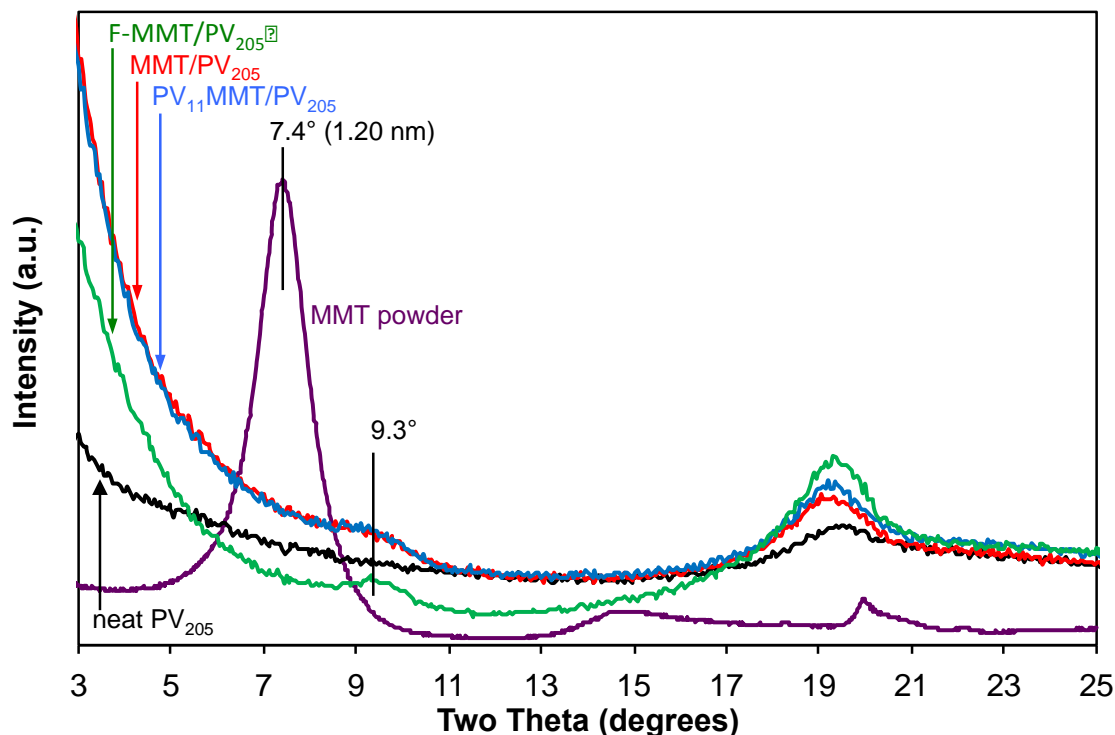
Figure 3.14. XRD patterns for starting MMT powder, neat PV_{205} film, and various 10 wt% MMT/PV_{205} composites as labeled in the plot. The intensity upturn at low angles is due to the underlying glass slide used to mount the polymer films for XRD.

3.4.3.2. Thermal and Mechanical Properties

DSC characterization indicates the effect of MMT surface pretreatment on composite thermal properties. DSC results (Figure 3.15) show that addition of untreated MMT to PVOH nucleates a new crystalline phase with a higher melting temperature than that of the neat polymer [155]. This new crystalline phase forms at the MMT/PVOH interface, accompanied by reduced bulk polymer crystallinity [156]. Our results indicate that MMT surface pretreatment has some effect on nanocomposite crystallinity. For the lowest molecular weight PV_{11} matrix (Figure 3.15a), composites incorporating

117

PV$_{11}$MMT and untreated MMT have essentially the same crystallization curves; this might be expected since the pretreatment and matrix polymers are the same in the PV$_{11}$MMT/PV$_{11}$ composite. The crystallite melting temperatures are about 5°C lower for the F-MMT/PV$_{11}$ composite compared to MMT/PV$_{11}$. It also appears that the F-MMT/PV$_{11}$ composite has more bulk and less interfacial crystallinity than MMT/PV$_{11}$. These observations suggest that adsorbed F108 disrupts the nucleation and growth of interfacial crystallites in the F-MMT/PV$_{11}$ composite.

For composites based on the intermediate molecular weight PV$_{95}$ matrix (Figure 3.15b), MMT pretreatment with PV$_{11}$ or F108 does not change the total amount of crystallinity or the relative amounts of bulk and interfacial crystallites. However, the nature of the pretreatment has an effect on crystallite nucleation. The PV$_{11}$MMT/PV$_{95}$ and F-MMT/PV$_{95}$ composites have crystallization temperatures that are about 5°C higher and 5°C lower, respectively, than those of untreated MMT/PV$_{95}$. As found for the F-MMT/PV$_{11}$ composite, the F108 pretreatment appears to disrupt crystallite nucleation in the F-MMT/PV$_{95}$ composite. In contrast, PV$_{11}$ pretreatment appears to promote PV$_{95}$ crystallite nucleation in the PV$_{11}$MMT/PV$_{95}$ composite.
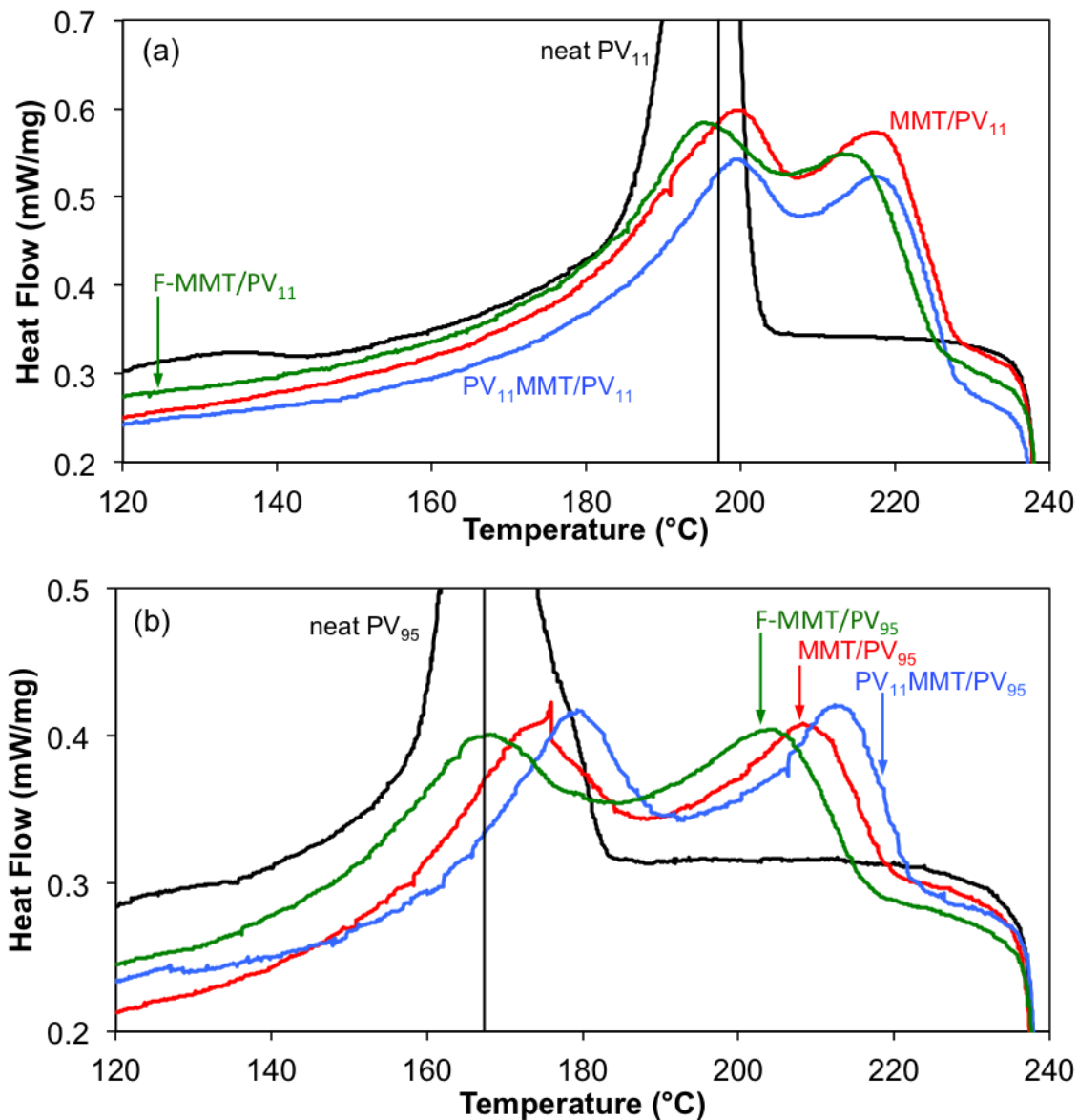
Figure 3.15. Exothermic heat flow during DSC first cooling scans for: (a) neat PV_{11} film and various MMT/PV_{11} composites and (b) neat PV_{95} film and various MMT/PV_{95} composites. The solid vertical lines indicate the locations of maxima in the crystallization peaks for the neat PV_{11} and PV_{95} films.

The highest PVOH molecular weight used in this study, PV_{205}, is less crystalline than PV_{11} and PV_{95}. Blending untreated MMT with PV_{205} appears to reduce the overall crystallinity in the MMT/PV_{205} composite compared to neat PV_{205} film (Figure 3.16), but exotherms associated with both bulk and interfacial crystallization are observed in the DSC cooling curve. Compared with the MMT/PV_{205} composite, those prepared with both PV_{11}MMT and F-MMT appear to have higher levels of interfacial crystallization and suppression of bulk polymer crystallization. Enhancement of interfacial crystallization seems to be greater in the PV_{11}MMT/PV_{205} composite.
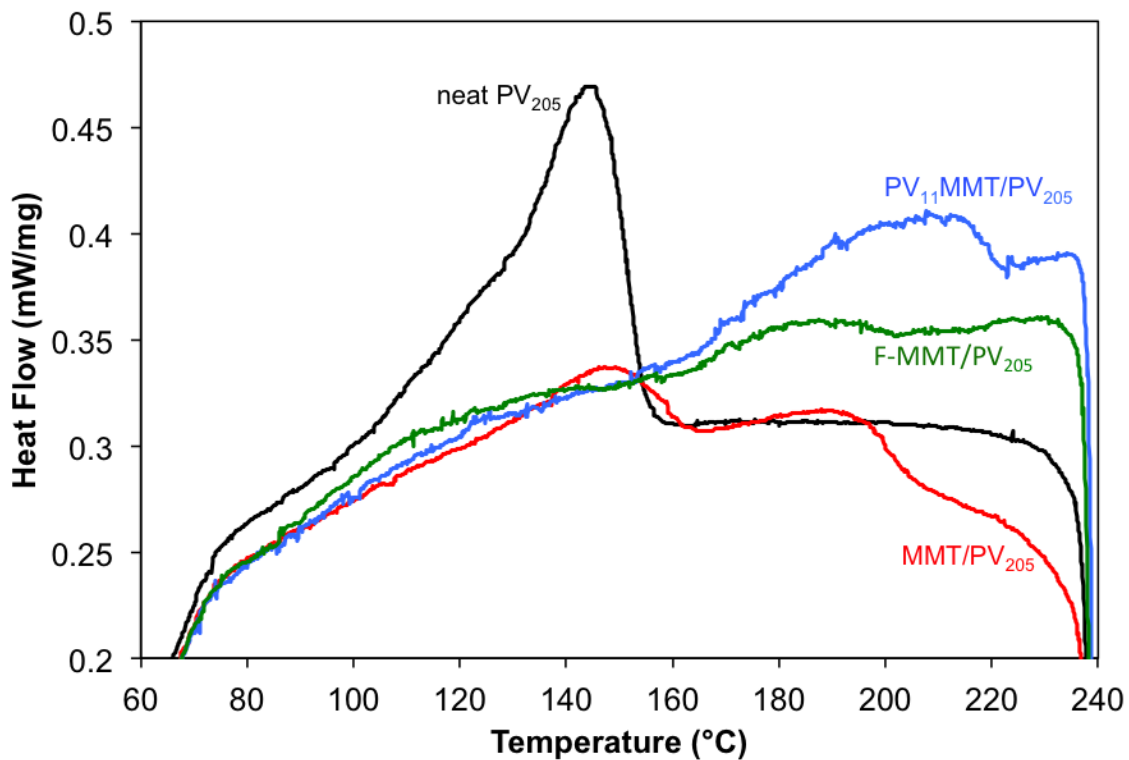
Figure 3.16. Exothermic heat flow during DSC first cooling scans for neat PV_{205} film and various MMT/PV_{205} composites.

The effect of MMT pretreatment on composite thermal stability and decomposition rate has been evaluated by TGA (Figures 3.17-3.19). In all cases, the neat PVOH films and MMT/PVOH composites lose 3-5% of their mass upon heating to 200°C. The composites incorporating $PV_{11}MMT$ appear to have somewhat smaller levels of water loss (Figures 3.17a and 3.18a). However, the differences are not significant; measured mass losses vary ±3% in this temperature range. The rate of mass loss accelerates at about 260°C for neat PV_{11} and all composites based on PV_{11}. Likewise, the rate of mass loss accelerates at about the same temperature (~290°C) for neat PV_{95} and its composites, as well as neat PV_{205} and its composites (~280°C). At higher temperatures, the presence of MMT slows down the thermal decomposition rates of the composites compared to the corresponding neat polymer films: the increasing MMT content creates a barrier that hinders the escape of decomposition products. However, we observe no significant influence of MMT pretreatment on decomposition rate, compared to composites based on untreated MMT. These TGA observations show that MMT pretreatment has little effect on the thermal stability and decomposition rate of MMT/PVOH composites.
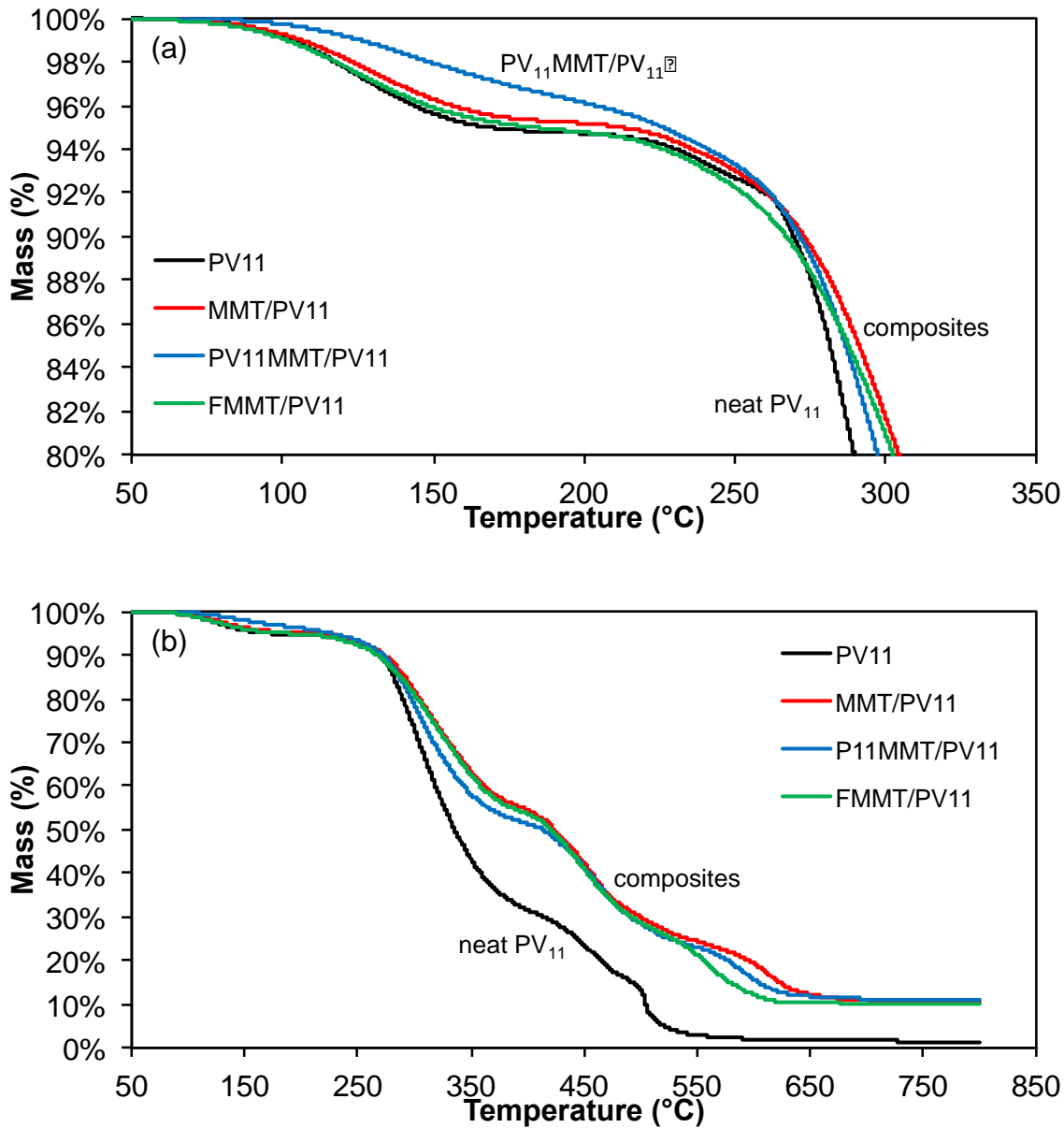
Figure 3.17. TGA mass loss as a function of temperature for neat PV_{11} film and various 10 wt% MMT/PV_{11} composites: (a) low temperature range, (b) full temperature range. In (a), the curve for the $PV_{11}MMT/PV_{11}$ composite is labeled separately but is not believed to differ significantly from the other curves.
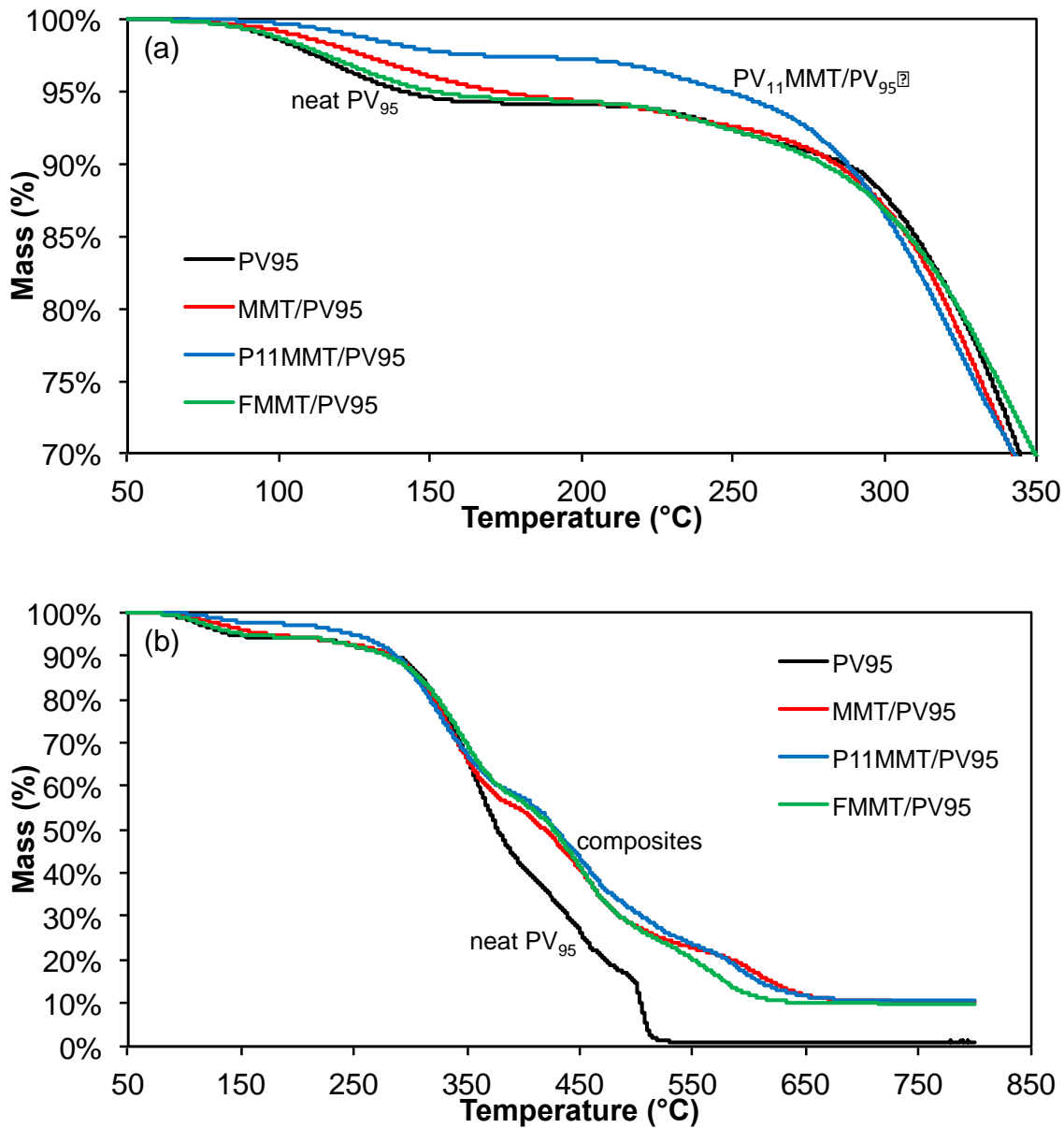
Figure 3.18. TGA mass loss as a function of temperature for neat PV_{95} film and various 10 wt% MMT/PV_{95} composites: (a) low temperature range, (b) full temperature range. In (a), the curve for the $PV_{11}MMT/PV_{95}$ composite is labeled separately but is not believed to differ significantly from the other curves.
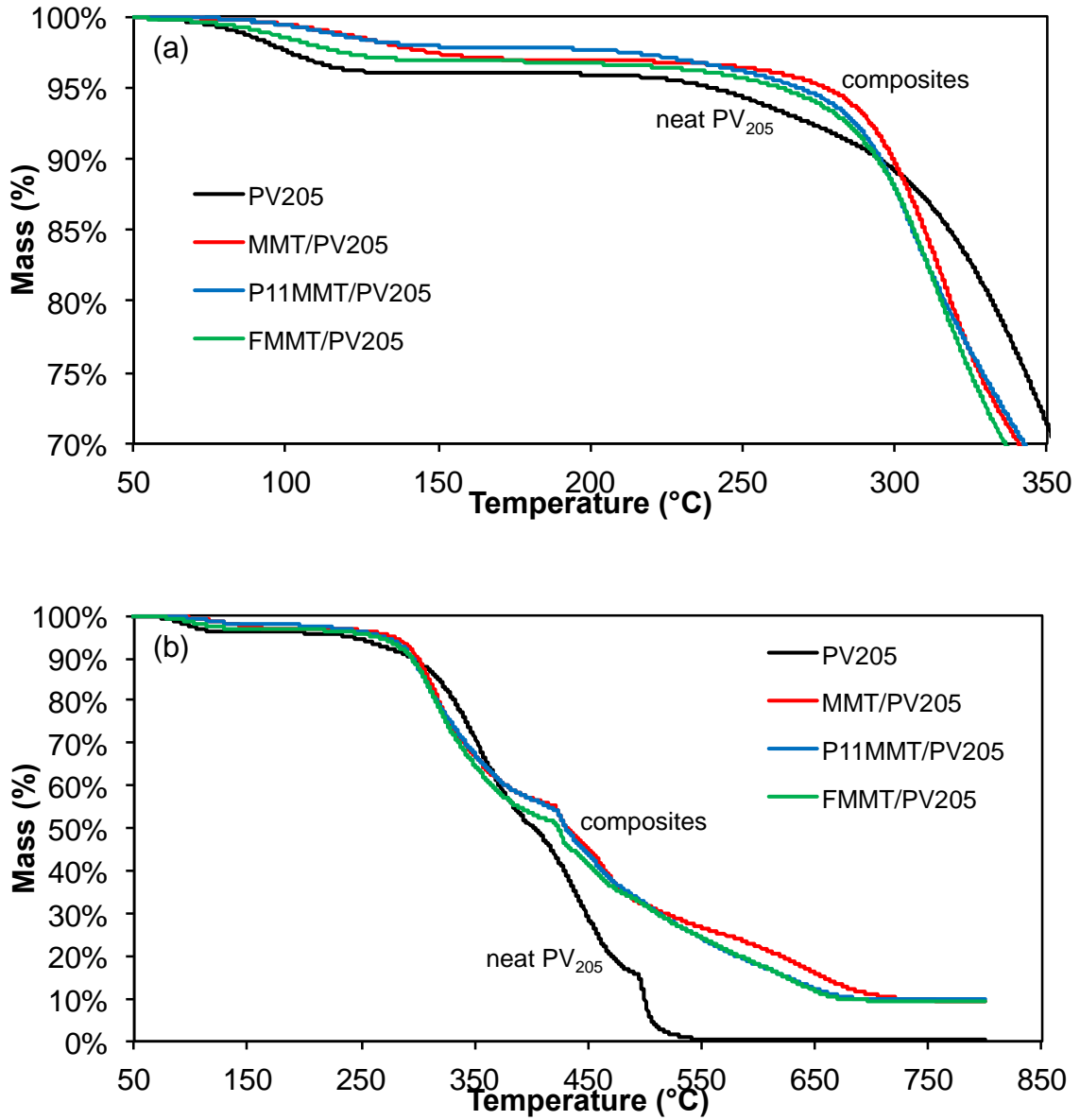
Figure 3.19. TGA mass loss as a function of temperature for neat PV_{205} film and various 10 wt% MMT/PV_{205} composites: (a) low temperature range, (b) full temperature range.

The effect of MMT pretreatment on composite mechanical properties, namely storage modulus and loss tangent, has been evaluated via DMA (Figures 3.20-3.24). For all matrix PVOH molecular weights, blending untreated MMT with PVOH appears to increase storage modulus (E') at all temperatures, relative to the neat polymer (Figures 3.20a and 3.21). Considering values measured at 25°C, average E' values in untreated MMT/PVOH composites are about 13%, 42%, and 41% higher compared to neat films of PV_{11}, PV_{95}, and PV_{205}, respectively (Figure 3.22), but the increases are statistically significant only for PV_{95} and PV_{205}. There are no statistically significant differences among the average E' values for composites incorporating untreated MMT, PV_{11}MMT, and F-MMT for all matrix PVOH molecular weights.
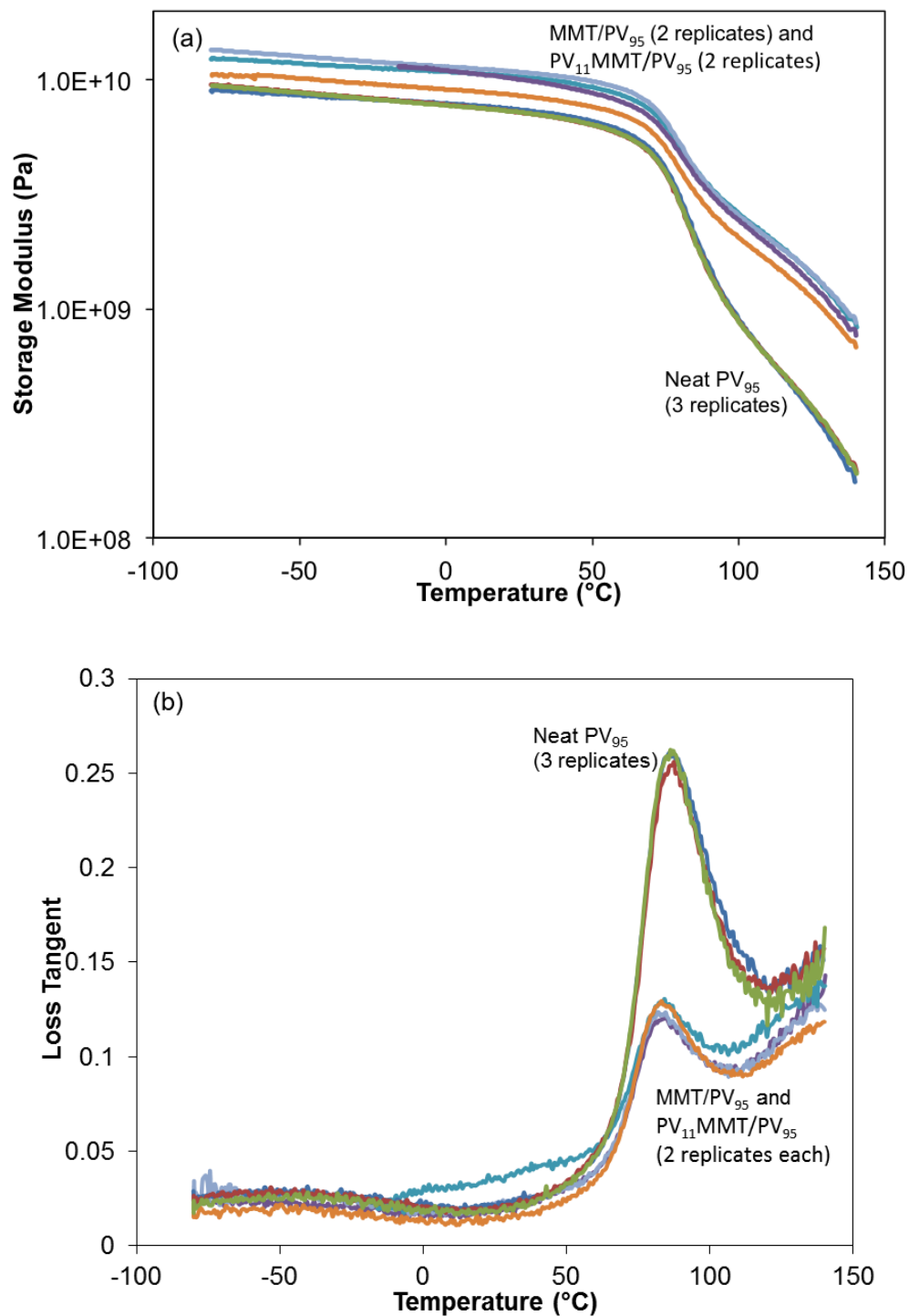
Figure 3.20. Storage modulus (a) and loss tangent (b) as functions of temperature for neat PV$_{95}$ films, untreated MMT/PV$_{95}$ composites, and PV$_{11}$MMT/PV$_{95}$ composites.

126
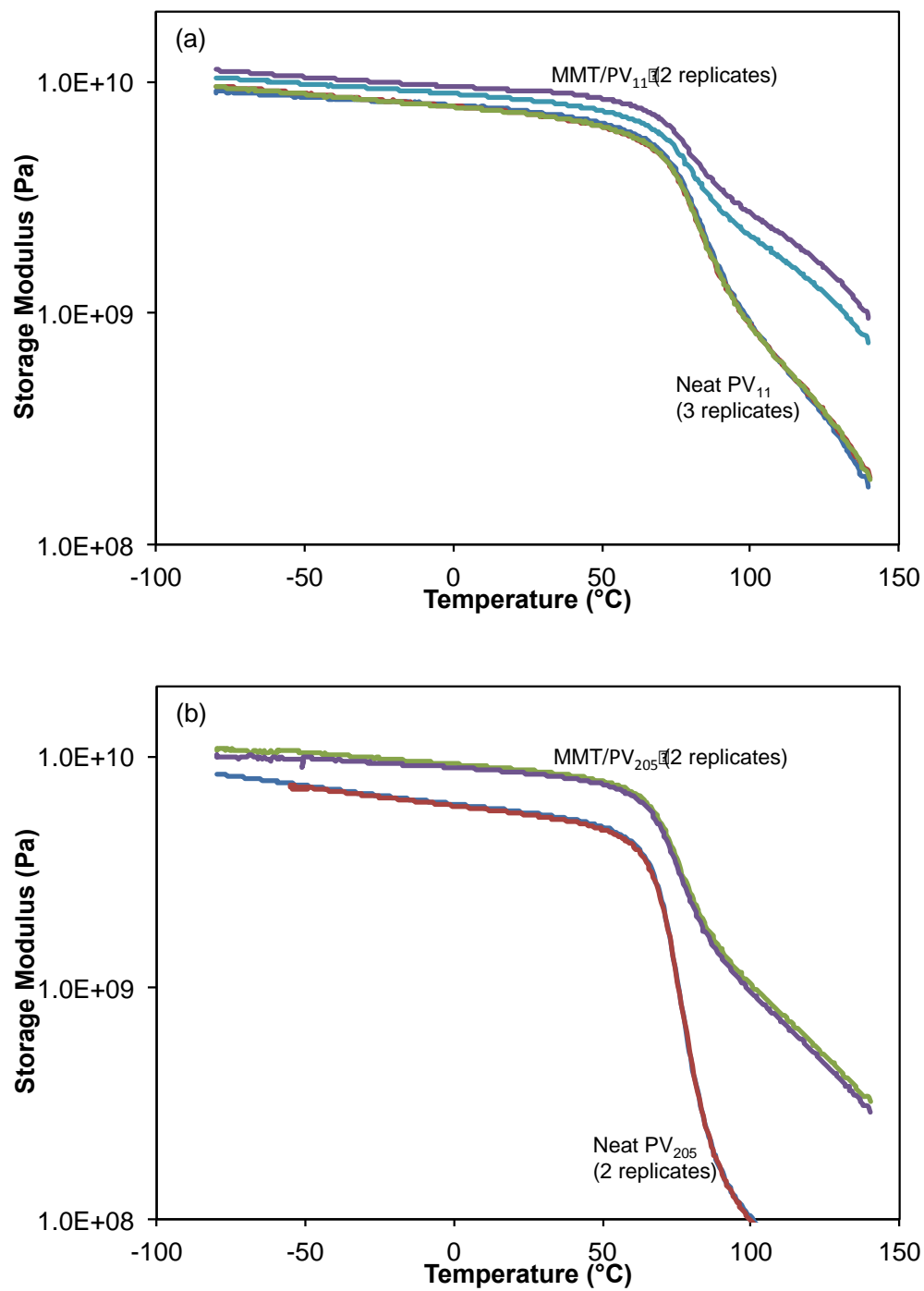
Figure 3.21. Storage modulus as a function of temperature for (a) neat PV_{11} film and untreated MMT/PV_{11} composite, and (b) neat PV_{205} film and untreated MMT/PV_{205} composite.
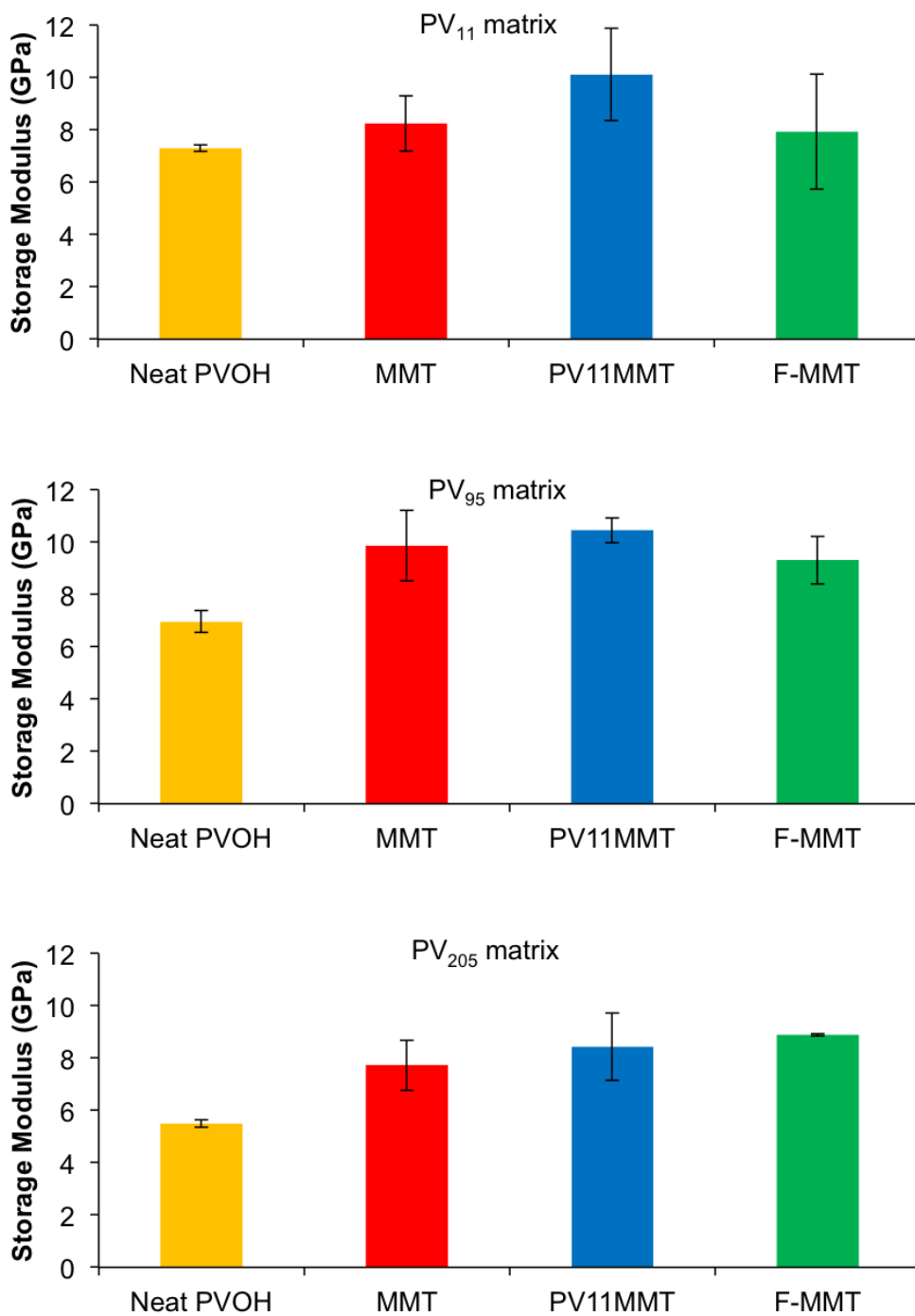
Figure 3.22. Storage modulus at 25°C for neat PVOH films and various MMT/PVOH composites. PVOH matrix molecular weight is indicated at the top of each panel; neat PVOH or filler is indicated below each bar. Error bars are 95% confidence limits based on 3 to 5 replicates.

With regard to loss tangent (Figure 3.20b), blending untreated MMT or $PV_{11}MMT$ with PV_{95} significantly reduces the magnitude of the loss tangent peak and shifts the peak temperature downward by about 4°C, relative to the corresponding neat PV_{95}. Similar trends in loss tangent peak values are observed for neat polymer films and treated/untreated composites based on PV_{11} and PV_{205} (Figures 3.23). Downward shifts of the peak temperature are significant for all fillers for the PV_{11} matrix, and for untreated MMT and $PV_{11}MMT$ for the PV_{95} matrix (Figure 3.24). Aside from these observations, there are no other statistically significant differences among the average loss tangent peak values or the peak temperatures for composites incorporating untreated MMT, $PV_{11}MMT$, and F-MMT (Figures 3.23 and 3.24). Overall, the DMA results indicate that MMT pretreatment has little or no effect on the mechanical properties of MMT/PVOH composites.
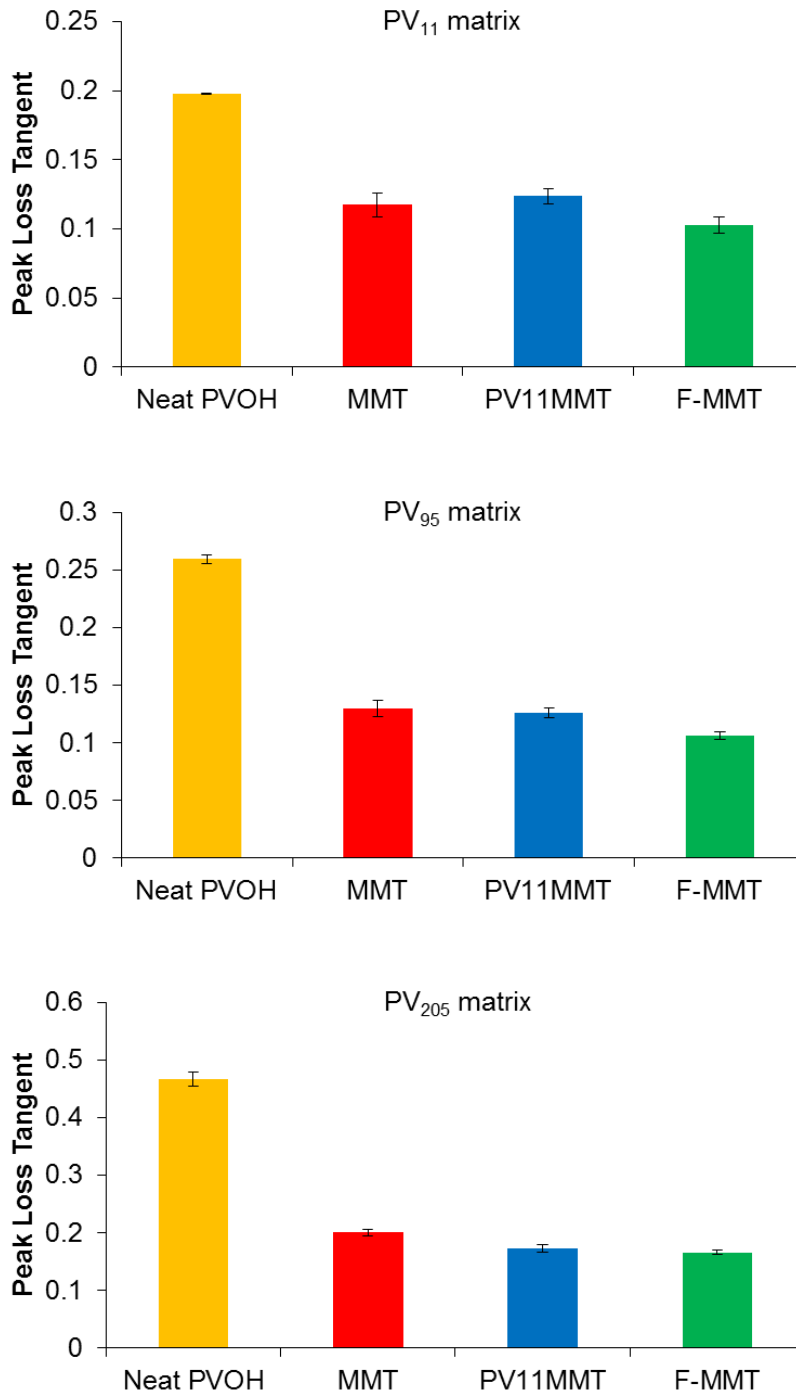
Figure 3.23. Peak loss tangent for neat PVOH films and various MMT/PVOH composites. PVOH matrix molecular weight is indicated at the top of each panel; neat PVOH or filler is indicated below each bar. Error bars are 95% confidence limits based on 3 to 5 replicates.
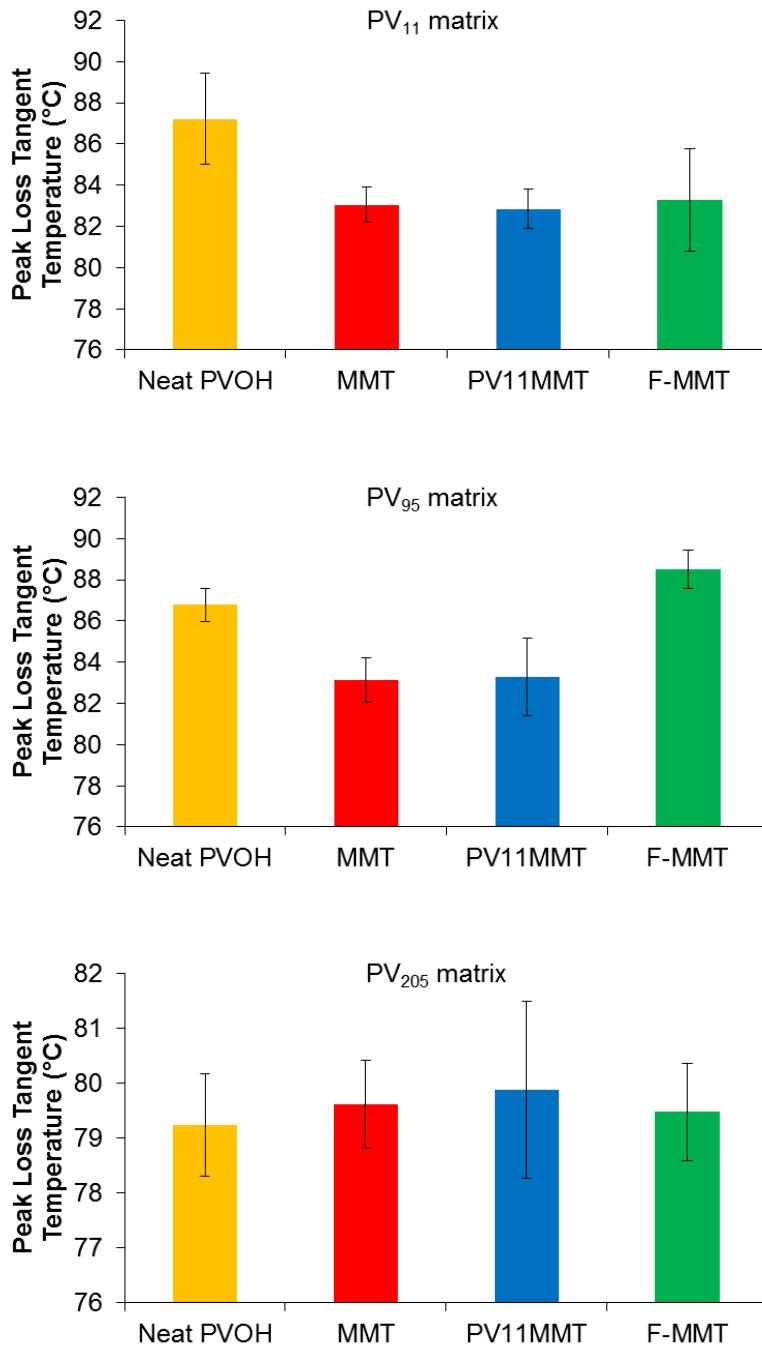
Figure 3.24. Peak loss tangent temperature for neat PVOH films and various MMT/PVOH composites. PVOH matrix molecular weight is indicated at the top of each panel; neat PVOH or filler is indicated below each bar. Error bars are 95% confidence limits based on 3 to 5 replicates.

3.4.3.3. Gas Barrier Performance

The effect of MMT pretreatment on the gas barrier performance of MMT/PVOH nanocomposites was investigated by measurements of water vapor transmission rate (WVTR), expressed in Figure 3.25 as water permeability. Compared to oxygen permeation experiments used in our preliminary work (Figure 3.4), water permeation tests are much faster, more reproducible, and less sensitive to variations in test gas humidity. Water permeation testing employed the same experimental apparatus as described earlier in Section 3.3.

Each group of bars in Figure 3.25 compare water permeabilities through films composed of the same molecular weight of the PVOH matrix (neat films and composites). For all PVOH molecular weights, there is no significant difference (at the 95% confidence level) between the permeabilities of untreated MMT/PVOH composites and the corresponding neat PVOH film. For the low molecular weight PV_{11} matrix, the untreated MMT/PV_{11} composite has higher water permeability than the neat polymer films at the 86% confidence level. We conclude that for MMT/PVOH composite films made by solution blending, addition of 10 wt% untreated MMT does not improve water barrier performance, and may even increase water permeability relative to neat polymer.

Considering composites prepared with pretreated MMT, Figure 3.25 shows that films incorporating either PV_{11}MMT or F-MMT have reduced water permeability values relative to neat PVOH and untreated MMT/PVOH composites. The statistical confidence levels for this observation vary among the data sets. For the lower and intermediate molecular weight PV_{11} and PV_{95} matrix polymers, permeability values for films with pretreated MMT are lower than those for the corresponding neat PVOH and untreated

132

MMT/PVOH composites with greater than 95% confidence levels. The exception among these is F-MMT/PV$_{11}$ compared to neat PV$_{11}$: the former has a lower permeability with 82% confidence.

For the high molecular weight PV$_{205}$ matrix polymer, the trend is the same, but with lower levels of statistical confidence. The average water permeability values of PV$_{11}$MMT/PV$_{205}$ and F-MMT/PV$_{205}$ composite films are lower than that of untreated MMT/PV$_{205}$ with greater than 90% confidence, and lower than that of neat PV$_{205}$ film with 70-80% confidence. For all three PVOH molecular weights, we observe no significant difference in water permeability values between PV$_{11}$MMT and F-MMT composites.

The results for PV$_{11}$MMT-based composites are particularly remarkable. Pretreating MMT with PV$_{11}$, and then blending this suspension with the identical PV$_{11}$ as the polymer matrix, produces a composite film with approximately one-third the water permeability (or three-fold barrier improvement) compared to a composite film prepared simply by blending untreated MMT with PV$_{11}$ matrix. The composite compositions are identical, but the preparation process varies, with profound consequences on a macroscopic property, water permeability.

Moreover, this unambiguously illustrates the distinct influence of polymer/platelet interfacial nanostructure on a macroscale composite property (water permeability). For adsorption of low molecular weight PV$_{11}$ onto MMT from dilute solutions (as in the pretreatment process), PV$_{11}$ molecules adsorb primarily in flattened "train" configurations [178] with most segments contacting the MMT surface. Such adsorbed PV$_{11}$ layers are thin but have high surface coverage; this minimizes bridging aggregation

during pretreatment. In contrast, adsorption of PV$_{11}$ from much higher concentration solutions (as in the blending process) results in more extended "loop" and "tail" configurations that leave more of the MMT surface exposed [178]. If the hydrophilic MMT surface (essentially a defect in the polymer matrix) facilitates water transport in MMT/PVOH composites, then the high MMT surface coverage resulting from PV$_{11}$ pretreatment may be effective in blocking interfacial water transport, thus reducing water permeability relative to that in untreated MMT/PVOH composites.

The overall conclusion is that MMT pretreatment with either PV$_{11}$ or F108 results in composite films with improved water barrier performance compared to composites containing untreated MMT, as well as compared to pure polymer films. This appears to be especially significant for composites made with low to moderate molecular weight PVOH matrices. In general, the results suggest that polymer interfacial nanostructure plays a significant, explicit role in water transport in MMT/PVOH composites.
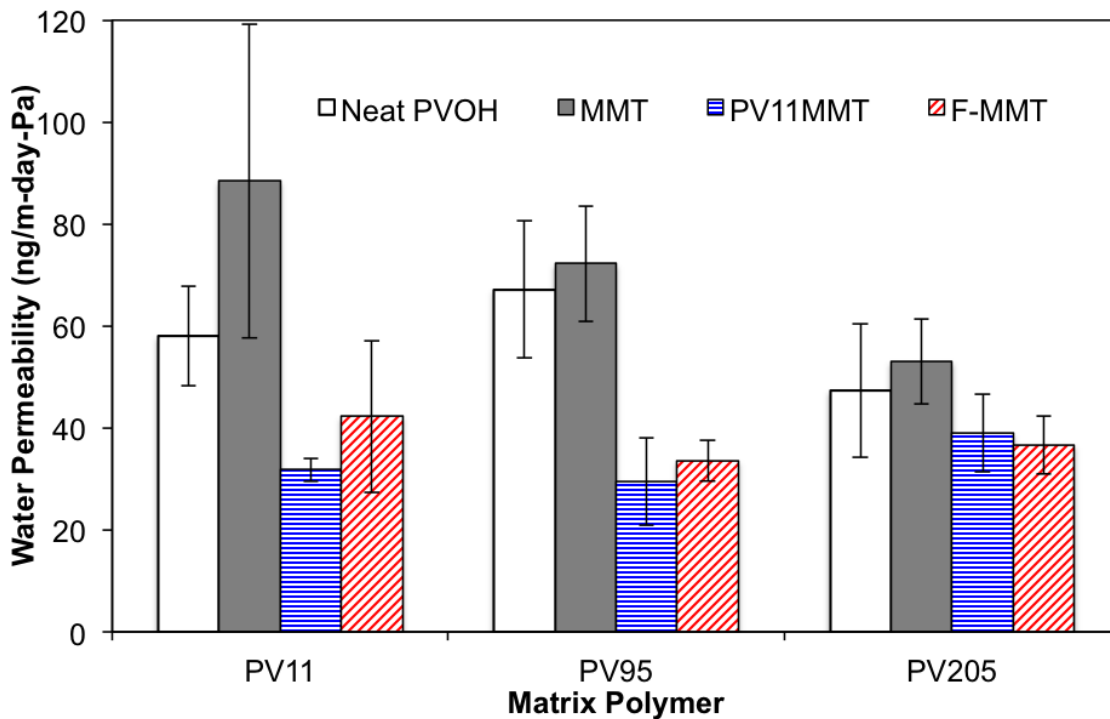
Figure 3.25. Water permeabilities in PVOH and MMT/PVOH films of low, medium, and high molecular weight polymer (PV_{11}, PV_{95}, PV_{205}). Within each group, bars from left to right denote results for neat PVOH and composites incorporating untreated MMT, PV_{11}MMT, and F-MMT. Error bars are 95% confidence limits.

3.4.3.4. Film Dissolution Behavior

Film dissolution behavior was studied by suspending pieces of composite films in DI water with stirring and modest heating, followed by dilution with DI water and DLS measurement of the average particle size. Consider (1) an "ideal" nanocomposite in which the matrix polymer adheres strongly to the filler nanoparticles, and (2) dissolution utilizing excess solvent that readily solubilizes the polymer and forms stable suspensions of re-dispersed filler nanoparticles. The particles released from the dissolved film ought to be somewhat larger than the starting filler nanoparticles, with the incremental size

increase due to the hydrodynamic effect of adsorbed polymer. In practice, the difference between the final and the initial nanoparticle size may be quite large due to incomplete dissolution, i.e., incomplete polymer-particle de-aggregation. Sufficient dilution can eliminate the possibility of large particle aggregates due to depletion flocculation. Assuming that thermodynamics favors complete polymer dissolution and particle re-dispersion, the root cause of incomplete dispersion probably lies in polymer-mediated bridging interactions between particles.

The MMT/PVOH system should be "ideal": PVOH is water-soluble, fully-exfoliated MMT suspensions can be prepared, and PVOH strongly adsorbs onto MMT. DLS results presented earlier (Figure 3.11) show that polymer bridging may occur during solution blending of untreated MMT suspensions with PVOH solutions. However, pretreatment with low molecular weight PVOH (PV_{11}) or F108 mitigates polymer bridging, at least in part, during solution blending. The film dissolution study aims to characterize, at least qualitatively, the effect of MMT pretreatment on polymer bridging during the film densification and drying steps.

To this end, we prepared solution-cast film samples that were dried, re-dissolved in DI water, diluted to a pre-determined MMT weight fraction, and then characterized by DLS. Two drying protocols were investigated. In the first, the cast films were air-dried in an oven at 40°C. The resulting "dried" films still contained significant amounts of residual water, approximately 2 to 4 wt% based on TGA data (Figures 3.17a-3.19a). In the second drying protocol, the cast films were "annealed" by air-drying in an oven at 120°C, reducing the water content of the films to about 1 wt% or less (estimated from TGA data).

136

Figure 3.26a shows DLS particle size measurements for suspensions produced by dissolving MMT/PVOH composite films that had been dried at 40°C. In all cases, the size difference values show that none of the films had undergone complete, "ideal" dissolution into constituent dissolved PVOH and re-suspended MMT particles. Considering the untreated MMT/PVOH composites first, the particle size difference decreases as the molecular weight of the PVOH matrix increases. For the highest molecular weight PV_{205} matrix, the density and thickness of the adsorbed steric barrier may be sufficient to minimize aggregation due to polymer bridging and van der Waals attraction. Film dissolution releases individual MMT platelets and small aggregates that may have been present in the blending suspension; hence the measured size difference is relatively small.

For the untreated MMT/PV_{95} and MMT/PV_{11} composites, the polymer adsorbed amount (molecules per unit MMT surface area) and adsorbed layer thickness decrease with decreasing PVOH molecular weight [178, 190]. Thinner adsorbed polymer layers permit closer interactions among MMT platelets in consolidated films, resulting in increased polymer bridging and van der Waals attraction. Upon immersion in water, the MMT aggregates do not disperse as thoroughly, resulting in measured particle size differences that increase with decreasing PVOH matrix molecular weight (Figure 3.26a).
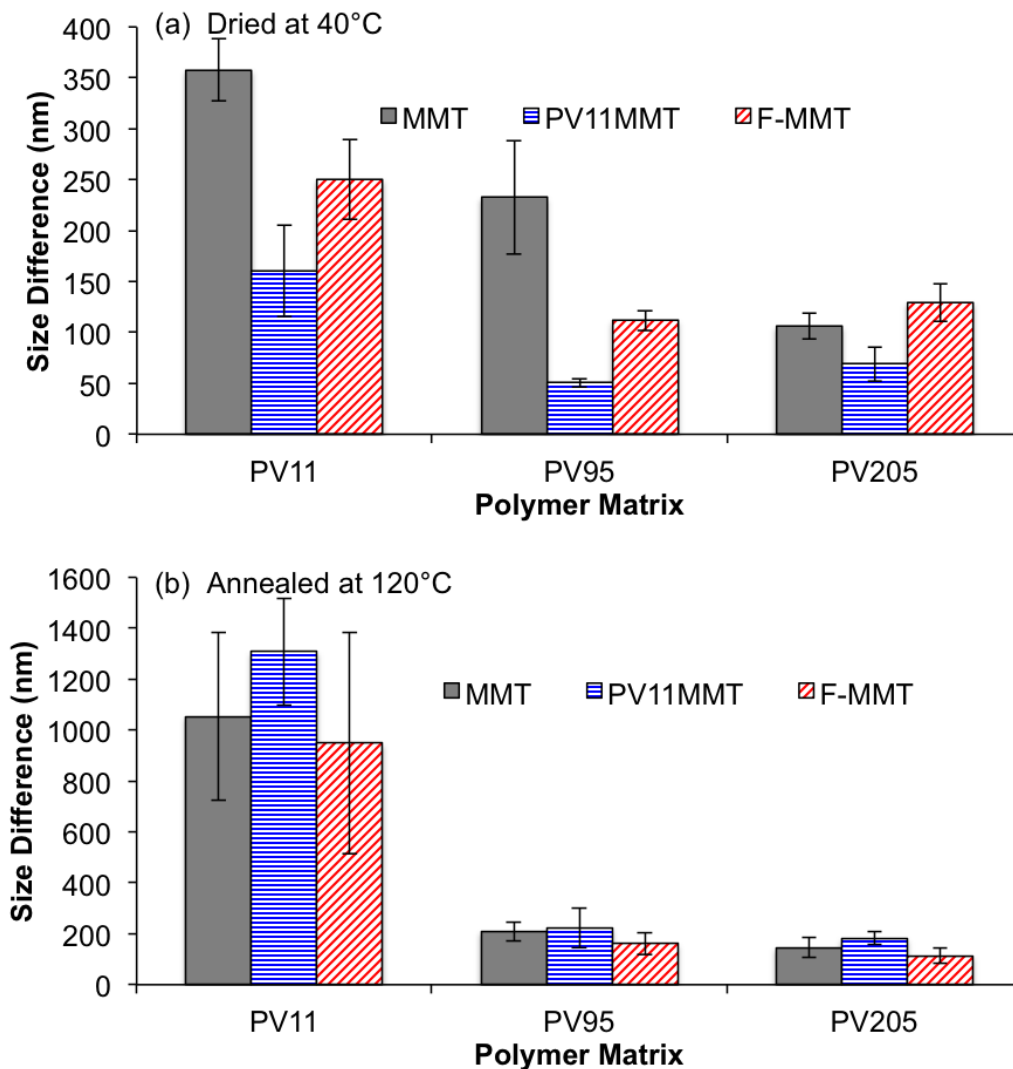
Figure 3.26. Particle size difference (relative to MMT particle size in stock suspension, measured by DLS) for MMT particles released from MMT/PVOH composite films dissolved in DI water. (a) Film samples dried at 40°C. (b) Film samples annealed at 120°C. Category labels indicate low, medium, and high molecular weight polymer matrix (PV_{11}, PV_{95}, PV_{205}). Within each group, bars from left to right denote results for composites incorporating untreated MMT, PV_{11}MMT, and F-MMT. Error bars are 95% confidence limits. In all cases, the dissolved film suspensions were diluted to a MMT weight fraction of 5.0×10^{-5} in DI water.

138

Pretreating MMT with PV_{11} or F108 has a remarkable effect on film dissolution behavior (Figure 3.26a). For $PV_{11}MMT/PV_{11}$, the average size of particles released from the dissolved film is almost 200 nm smaller than that of particles released from the dissolved, untreated MMT/PV_{11} composite. In other words, if one pretreats MMT with PV_{11} and then blends this suspension with identical PV_{11} as the matrix polymer, the resulting film dissolves more completely than films prepared by simply blending untreated MMT with PV_{11}.

This observation can be rationalized, once again, in terms of the nanoscale polymer structure at the MMT/PVOH interface. During MMT pretreatment, PV_{11} molecules adsorbing from dilute solution assume flattened "train" configurations. This results in high coverage of the MMT surface, making aggregation due to polymer bridging less likely. Moreover, during solution blending, incoming PV_{11} matrix molecules are less likely to adsorb on the pretreated $PV_{11}MMT$ surface, further mitigating polymer bridging aggregation. The PV_{11} matrix still maintains a steric barrier between nearby MMT platelets. Thus, upon $PV_{11}MMT/PV_{11}$ film dissolution, the released particle aggregates are smaller than those released from dissolved, untreated MMT/PV_{11}. During blending of untreated MMT with higher concentrations of PV_{11} solution, PV_{11} molecules adsorb in more extended "loop/tail" configurations. This surface structure permits more polymer bridging between neighboring platelets during film densification, and thus less complete dissolution when the final film is exposed to water.

Considering the treated $F-MMT/PV_{11}$ composite (Figure 3.26a), particles released during film dissolution are only about 100 nm smaller than those released from the

untreated MMT/PV$_{11}$ composite, and about 100 nm larger than particles released from the treated PV$_{11}$MMT/PV$_{11}$ composite. This implies that F108 does not protect the MMT surface against PV$_{11}$ bridging as effectively as pre-adsorbed PV$_{11}$. This again can be rationalized in terms of interfacial structure. F108 is a triblock copolymer that may adsorb onto MMT in a more extended configuration than PV$_{11}$, making the MMT surface more accessible to incoming matrix PV$_{11}$ molecules during the blending process.

The film dissolution behavior seen for composites based on PV$_{11}$ matrix polymer also applies to PV$_{95}$ composites (Figure 3.26a). Particles released during the dissolution of PV$_{11}$MMT/PV$_{95}$ and F-MMT/PV$_{95}$ composites are about 180 nm and 120 nm smaller, respectively, than particles released during the dissolution of MMT/PV$_{95}$ composite. In fact, the particles released by the dissolution of PV$_{11}$MMT/PV$_{95}$ film are only 50 nm larger than that of the starting MMT platelets used in the composite's synthesis. These results show that PV$_{11}$ and F108 are both effective pretreatments for mitigating polymer bridging during densification of PV$_{95}$-based composites.

In contrast, PV$_{11}$ and F108 pretreatments do not have much impact on the film dissolution behavior of composites based on the higher molecular weight PV$_{205}$ matrix polymer (Figure 3.26a). The relatively small particle size difference for untreated MMT/PV$_{205}$ (about 100 nm relative to the starting MMT platelet size) indicates that PV$_{205}$ adsorption onto untreated MMT produces a steric barrier thick enough to significantly reduce polymer bridging during film densification. MMT pretreatment with PV$_{11}$ and F108 does not have much impact, possibly due to the displacement of these lower molecular weight molecules during adsorption of higher molecular weight PV$_{205}$.

Figure 3.26b shows DLS particle size measurements for suspensions produced by dissolution of MMT/PVOH composite films annealed at 120°C. For composites based on low molecular weight PV_{11} matrix polymer, DLS results show that the particles released by film dissolution are more than 1000 nm larger than the starting MMT platelets. Moreover, MMT pretreatment has no significant impact on film dissolution behavior. In practice, these films do not easily dissolve in water, even with extended stirring and heating. For the higher molecular weight PV_{95} and PV_{205} matrix polymers, the released particles are 115-225 nm larger than the starting MMT platelets, indicating more facile film dissolution in these cases. Once again, however, we observe that MMT pretreatment has no significant impact on film dissolution behavior.

These observations can also be rationalized in terms of MMT/PVOH interfacial structure and its dependence on PVOH molecular weight. TGA shows that heating MMT/PVOH composites from 40°C to 120°C results in weight losses of 2-4% (Figures 3.17a-3.19a), almost certainly due to the removal of residual water. Much of this water probably came from the vicinity of the surfaces of the hydrophilic MMT platelets. The residual water occupied space on the MMT surfaces and associated with PVOH molecules, presumably through hydrogen bonding. Removal of the residual water certainly resulted in significant changes in the polymer's interfacial structure, primarily consolidation of the adsorbed polymer layers due to additional binding to the MMT surface. For low molecular weight PV_{11} matrix polymer, this leads to MMT platelet-platelet adhesion due to both polymer bridging and van der Waals attraction, making it very difficult to de-aggregate and re-disperse the MMT. On the other hand, the higher molecular weight PV_{95} and PV_{205} matrix polymers adsorb to form thicker layers on

MMT. Even when the residual water is removed, the thicker steric barriers help mitigate both polymer bridging and van der Waals attraction, making it easier to de-aggregate and re-disperse the MMT platelets.

3.5. Conclusions

In this work, a low molecular weight PVOH (PV_{11}) and a PEO-PPO-PEO triblock copolymer (F108 Pluronic®) were studied as pretreatments to modify the surface of exfoliated MMT platelets prior to solution blending with PVOH matrices of varying molecular weight. DLS (Figure 3.11) shows that pretreating MMT with PV_{11} or F108 limits platelet aggregation during solution blending, especially as matrix PVOH molecular weight increases. XRD gave no indication of MMT platelet re-stacking or any variations in polymer crystallinity due to MMT pretreatment. DSC revealed that PV_{11}MMT seemed to promote interfacial nucleation of matrix PVOH, while F-MMT seemed to generally have the opposite effect. Both TGA and DMA suggested that MMT pretreatment had no significant effect on composite thermal stability and mechanical properties, respectively.

On the other hand, MMT pretreatment does have a significant impact on water permeation in MMT/PVOH nanocomposites (Figure 3.25). By occupying polar water binding sites on the hydrophilic MMT surface, PV_{11} and F108 may impede water transport along the MMT surface, thus enhancing barrier performance. Film dissolution studies also show that MMT pretreatment also influences the dissolution behavior of partially-dried, non-annealed MMT/PVOH composite films. Both the water barrier and

film dissolution results show that the local nanostructure at the PVOH-MMT interface may be altered by pretreatment with PV_{11} and F108, producing significant changes in macroscopic properties. Direct comparison of results for $PV_{11}MMT/PV_{11}$ and untreated MMT/PV_{11} show that even though the composite compositions are identical, variations in processing details can have a major impact on composite properties and performance. These observations may be significant for polymer nanocomposite applications in the packaging industry.

References

[1]   F. Bergaya, M. Vayer, Appl. Clay Sci. 12 (1997) 275.

[2]   L. Ammann, F. Bergaya, G. Lagaly, Clay Miner. 40 (2005) 441.

[3]   M. Fang, C. H. Kim, T. E. Mallouk, Chem. Mater. 11 (1999) 1519.

[4]   M. Park, I.-K. Shim, E.-Y. Jung, J.-H. Choy, J. Phys. Chem. Solids 65 (2004) 499.

[5]   N. N. Herrera, J.-M. Letoffe, J.-P. Reymond, E. Bourgeat-Lami, J. Mater. Chem. 15 (2005) 863.

[6]   P. A. Wheeler, J. Wang, J. Baker, L. J. Mathias, Chem. Mater. 17 (2005) 3012.

[7]   L. M. Daniel, R. L. Frost, H. Y. Zhu, J. Colloid Interf. Sci. 321 (2008) 302.

[8]   S. P. Patil, R. Mathew, T. G. Ajithkumar, P. R. Rajamohanan, T. S. Mahesh, G. Kumaraswamy, J. Phys. Chem. B 112 (2008) 4536.

[9]   H. He, J. Duchet, J. Galy, J.-F. Gerard, J. Colloid Interf. Sci. 288 (2005) 171.

[10]   A. M. Shanmugharaj, K. Y. Rhee, S. H. Ryu, J. Colloid Interf. Sci. 298 (2006) 854.

[11]   W. Shen, H. He, J. Zhu, P. Yuan, R. L. Frost, J. Colloid Interf. Sci. 313 (2007) 268.

[12]   A. Di Gianni, E. Amerio, O. Monticelli, R. Bongiovanni, Appl. Clay Sci. 42 (2008) 116.

[13]   Z. Qian, G. Hu, S. Zhang, M. Yang, Physica B 403 (2008) 3231.

[14]   M. U. de la Orden, J. Arranz, V. Lorenzo, E. Pérez, J. M. Urreaga, J. Colloid
       Interf. Sci. 342 (2010) 185.

[15]   F. Piscitelli, P. Posocco, R. Toth, M. Fermeglia, S. Pricl, G. Mensitieri, M.
       Lavorgna, J. Colloid Interf. Sci. 351 (2010) 108.

[16]   S. Şen, Polym. Compos. 31 (2010) 482.

[17]   P. H. Mutin, G. Guerrero, A. Vioux, J. Mater. Chem. 15 (2005) 3761.

[18]   C. Queffélec, M. Petit, P. Janvier, D. A. Knight, B. Bujoli, Chem. Rev. 112
       (2012) 3777.

[19]   S. Marcinko, A. Y. Fadeev, Langmuir 20 (2004) 2270.

[20]   J. Randon, P. Blanc, R. Paterson, J. Membrane Sci. 98 (1995) 119.

[21]   J. Caro, M. Noack, P. Kölsch, Micropor. Mesopor. Mat. 22 (1998) 321.

[22]   G. Guerrero, P. H. Mutin, A. Vioux, J. Mater. Chem. 11 (2001) 3161.

[23]   G. Guerrero, P. H. Mutin, A. Vioux, Chem. Mater. 13 (2001) 4367.

[24]   U. Lafont, L. Simonin, M. Gaberscek, E. M. Kelder, J. Power Sources 174 (2007)
       1104.

[25]   K. Wapner, M. Stratmann, G. Grundmeier, Int. J. Adhes. Adhes. 28 (2007) 59.

[26]   S. Mohapatra, P. Pramanik, Colloid Surface A 339 (2009) 35.

[27]   Y. J. Weng, J. R. Ren, N. Huang, J. Wang, J. Y. Chen, Y. X. Leng, H. Q. Liu,
       Mat. Sci. Eng. C 28 (2008) 1495.

[28]   H. W. Choi, H. J. Lee, K. J. Kim, H.-M. Kim, S. C. Lee, J. Colloid Interf. Sci. 304
       (2006) 277.

[29]   W. Yan, E. W. Hagaman, S. Dai, Chem. Mater. 16 (2004) 5182.

[30] J. L. Guimarães, P. Peralta-Zamora, F. Wypych, J. Colloid Interf. Sci. 206 (1998) 281.

[31] C. Breen, N. D'Mello, J. Yarwood, J. Mater. Chem. 12 (2002) 273.

[32] C. Trobajo, S. A. Khainakov, A. Espina, J. R. García, Chem. Mater. 13 (2001) 4457.

[33] U. Costantino, M. Casciola, L. Massinelli, M. Nocchetti, R. Vivani, Solid State Ionics 97 (1997) 203.

[34] F. Wypych, W. H. Schreiner, N. Mattoso, D. H. Mosca, R. Marangoni, C. A. da S. Bento, J. Mater. Chem. 13 (2003) 304.

[35] J. D. Wang, G. Serrette, Y. Tian, A. Clearfield, Appl. Clay Sci. 10 (1995) 103.

[36] S. Carlino, M. J. Hudson, S. W. Husain, J. A. Knowles, Solid State Ionics 84 (1996) 117.

[37] H. Nijs, A. Clearfield, E. F. Vansant, Micropor. Mesopor. Mat. 23 (1998) 97.

[38] V. Prévot, C. Forano, J. P. Besse, Appl. Clay Sci. 18 (2001) 3.

[39] H. R. Allcock, M. A. Hofmann, C. M. Ambler, R. V. Morford, Macromolecules 35 (2002) 3484.

[40] A. L. Rusanov, P. V. Kostoglodov, M. J. M. Abadie, V. Y. Voytekunas, D. Y. Likhachev, Adv. Polym. Sci. 216 (2008) 125.

[41] R. E. Schaak, T. E. Mallouk, Chem. Mater. 14 (2002) 1455.

[42] M. A. Bizeto, A. L. Shiguihara, V. R. L. Constantino, J. Mater. Chem. 19 (2009) 2512.

[43] K. G. S. Ranmohotti, E. Josepha, J. Choi, J. Zhang, J. B. Wiley, Adv. Mater. 23 (2011) 442.

[44]   W. Sugimoto, M. Shirata, Y. Sugahara, K. Kuroda, J. Am. Chem. Soc. 121 (1999) 11601.

[45]   J. Gopalakrishnan, V. Bhat, Inorg. Chem. 26 (1987) 4299.

[46]   A. Clearfield, Chem. Rev. 88 (1988) 125.

[47]   S. Uma, A. R. Raju, J. Gopalakrishnan, J. Mater. Chem. 3 (1993) 709.

[48]   S. Uma, J. Gopalakrishnan, Chem. Mater. 6 (1994) 907.

[49]   N. S. P. Bhuvanesh, M.-P. Crosnier-Lopez, H. Duroy, J.-L. Fourquet, J. Mater. Chem. 10 (2000) 1685.

[50]   R. E. Schaak, T. E. Mallouk, J. Am. Chem. Soc. 122 (2000) 2798.

[51]   S. Takahashi, T. Nakato, S. Hayashi, Y. Sugahara, K. Kuroda, Inorg. Chem. 34 (1995) 5065.

[52]   H. Suzuki, K. Notsu, Y. Takeda, W. Sugimoto, Y. Sugahara, Chem. Mater. 15 (2003) 636.

[53]   S. Tahara, Y. Sugahara, Langmuir 19 (2003) 9473.

[54]   Y. Takeda, H. Suzuki, K. Notsu, W. Sugimoto, Y. Sugahara, Mater. Res. Bull. 41 (2006) 834.

[55]   S. Tahara, T. Ichikawa, G. Kajiwara, Y. Sugahara, Chem. Mater. 19 (2007) 2352.

[56]   Y. Tsunoda, W. Sugimoto, Y. Sugahara, Chem. Mater. 15 (2003) 632.

[57]   Y. Takeda, T. Momma, T. Osaka, K. Kuroda, Y. Sugahara, J. Mater. Chem. 18 (2008) 3581.

[58]   A. Shimada, Y. Yoneyama, S. Tahara, P. H. Mutin, Y. Sugahara, Chem. Mater. 21 (2009) 4155.

[59]   M. M. J. Treacy, S. B. Rice, A. J. Jacobson, J. T. Lewandowski, Chem. Mater. 2 (1990) 279.

[60]   M. Fang, C. H. Kim, G. B. Saupe, H.-N. Kim, C. C. Waraksa, T. Miwa, A. Fujishima, T. E. Mallouk, Chem. Mater. 11 (1999) 1526.

[61]   R. E. Schaak, T. E. Mallouk, Chem. Mater. 12 (2000) 2513.

[62]   R. E. Schaak, T. E. Mallouk, Chem. Mater. 12 (2000) 3427.

[63]   Y.-S. Han, I. Park, J.-H. Choy, J. Mater. Chem. 11 (2001) 1277.

[64]   Y. Ebina, T. Sasaki, M. Watanabe, Solid State Ionics 151 (2002) 177.

[65]   F. F. Xu, Y. Ebina, Y. Bando, T. Sasaki, J. Phys. Chem. B 107 (2003) 9638.

[66]   A. L. Shiguihara, M. A. Bizeto, V. R. L. Constantino, Colloid Surface A 295 (2007) 123.

[67]   H. Gao, S. Shori, X. Chen, H.-C. zur Loye, H. J. Ploehn, J. Colloid Interf. Sci. 392 (2013) 226.

[68]   K. Domen, J. Yoshimura, T. Sekine, A. Tanaka, T. Onishi, Catal. Lett. 4 (1990) 339.

[69]   K. Domen, Y. Ebina, J. Kondo, Res. Chem. Intermed. 20 (1994) 895.

[70]   R. Abe, K. Shinohara, A. Tanaka, M. Hara, J. N. Kondo, K. Domen, Chem. Mater. 9 (1997) 2179.

[71]   J. A. Schottenfeld, A. J. Benesi, P. W. Stephens, G. Chen, P. C. Eklund, T. E. Mallouk, J. Solid State Chem. 178 (2005) 2313.

[72]   K. Maeda, K. Domen, J. Phys. Chem. C 111 (2007) 7851.

[73]   K. Maeda, M. Eguchi, W. J. Youngblood, T. E. Mallouk, Chem. Mater. 20 (2008) 6770.

[74]   F. E. Osterloh, Chem. Mater. 20 (2008) 35.

[75]   A. Kudo, Y. Miseki, Chem. Soc. Rev. 38 (2009) 253.

[76]   M. R. Allen, A. Thibert, E. M. Sabio, N. D. Browning, D. S. Larsen, F. E. Osterloh, Chem. Mater. 22 (2010) 1220.

[77]   M. Kitano, M. Hara, J. Mater. Chem. 20 (2010) 627.

[78]   K. Maeda, J. Photoch. Photobio. C 12 (2011) 237.

[79]   O. C. Compton, E. C. Carroll, J. Y. Kim, D. S. Larsen, F. E. Osterloh, J. Phys. Chem. C 111 (2007) 14589.

[80]   O. C. Compton, C. H. Mullet, S. Chiang, F. E. Osterloh, J. Phys. Chem. C 112 (2008) 6202.

[81]   K. Maeda, M. Eguchi, W. J. Youngblood, T. E. Mallouk, Chem. Mater. 21 (2009) 3611.

[82]   K. Maeda, M. Eguchi, S.-H. A. Lee, W. J. Youngblood, H. Hata, T. E. Mallouk, J. Phys. Chem. C 113 (2009) 7962.

[83]   E. M. Sabio, M. Chi, N. D. Browning, F. E. Osterloh, Langmuir 26 (2010) 7254.

[84]   H. Zhou, E. M. Sabio, T. K. Townsend, T. Fan, D. Zhang, F. E. Osterloh, Chem. Mater. 22 (2010) 3362.

[85]   E. M. Sabio, R. L. Chamousis, N. D. Browning, F. E. Osterloh, J. Phys. Chem. C 116 (2012) 3161.

[86]   M. Lotya, A. Rakovich, J. F. Donegan, J. N. Coleman, Nanotechnology 24 (2013) 265703.

[87]   M. Fang, C. H. Kim, T. E. Mallouk, Chem. Mater. 11 (1999) 1519.

[88]   W. A. Schafer, P. W. Carr, J. Chromatogr. 587 (1991) 137.

[89]   H. Souma, R. Chiba, S. Hayashi, Bull. Chem. Soc. Jpn. 84 (2011) 1267.

[90]   T. J. R. Weakley, Acta Cryst. 32 (1976) 2889.

[91]   A. H. Mahmoudkhani, V. Langer, J. Mol. Struct. 609 (2002) 97.

[92]   C. Gervais, M. Profeta, V. Lafond, C. Bonhomme, T. Azaïs, H. Mutin, C. J. Pickard, F. Mauri, F. Babonneau, Magn. Reson. Chem. 42 (2004) 445.

[93]   W. Förner, H. M. Badawi, Z. Naturforsch. 65b (2010) 357.

[94]   A. H. Mahmoudkhani, V. Langer, Solid State Sci. 3 (2001) 519.

[95]   C. B. A. Lima, C. Airoldi, Solid State Sci. 4 (2002) 1321.

[96]   T. Sasaki, S. Nakano, S. Yamauchi, M. Watanabe, Chem. Mater. 9 (1997) 602.

[97]   K. Saruwatari, H. Sato, T. Kogure, T. Wakayama, M. Iitake, K. Akatsuka, M. Haga, T. Sasaki, A. Yamagishi, Langmuir 22 (2006) 10066.

[98]   K. Akatsuka, M.-a. Haga, Y. Ebina, M. Osada, K. Fukuda, T. Sasaki, ACS Nano. 3 (2009) 1097.

[99]   S.-H. Kwon, Y.-K. Jun, S.-H. Hong, H.-E. Kim, J. Eur. Ceram. Soc. 23 (2003) 1039.

[100] Liga Berzina-Cimdina and Natalija Borodajenko (2012). Research of Calcium Phosphates Using Fourier Transform Infrared Spectroscopy, Infrared Spectroscopy - Materials Science, Engineering and Technology, Prof. Theophanides Theophile (Ed.), ISBN: 978-953-51-0537-4, InTech, Available from:

http://www.intechopen.com/books/infrared-spectroscopy-materials-science-engineering-andtechnology/research-of-calcium-phosphates-using-fourier-transformation-infrared-spectroscopy

[101] Z. He, C. W. Honeycutt, T. Zhang, P. J. Pellechia, W. A. Caliebe, Soil Sci. Soc. Am. J. 71 (2007) 940.

[102] C. Slater, D. Laurencin, V. Burnell, M. E. Smith, L. M. Grover, J. A. Hriljac, A. J. Wright, J. Mater. Chem. 21 (2011) 18783.

[103] Y. Chen, X. Zhao, H. Ma, S. Ma, G. Huang, Y. Makita, X. Bai, X. Yang, J. Solid State Chem. 181 (2008) 1684.

[104] P. Kim, N. M. Doss, J. P. Tillotson, P. J. Hotchkiss, M.-J. Pan, S. R. Marder, J. Li, J. P. Calame, J. W. Perry, ACS Nano. 3 (2009) 2581.

[105] A. J. Jacobson, J. T. Lewandowski, J. W. Johnson, J. Less-Common Met. 116 (1986) 137.

[106] B. J. Cade-Menun, in Organic Phosphorus in the Environment (B. L. Turner, E. Frossard, D. Baldwin, eds.). CAB International, Wallingford, UK, 2005, pp. 21-44.

[107] W. Gao, L. Dickinson, C. Grozinger, F. G. Morin, L. Reven, Langmuir 12 (1996) 6429.

[108] S. Pawsey, M. McCormick, S. De Paul, R. Graf, Y. S. Lee, L. Reven, H. W. Spiess, J. Am. Chem. Soc. 125 (2003) 4174.

[109] M. Nilsing, S. Lunell, P. Persson, L. Ojamäe, Surf. Sci. 582 (2005) 49.

[110] R. Luschtinetz, G. Seifert, E. Jaehne, H.-J. P. Adler, Macromol. Symp. 254 (2007) 248.

[111] F. Brodard-Severac, G. Guerrero, J. Maquet, P. Florian, C. Gervais, P. H. Mutin, Chem. Mater. 20 (2008) 5191.

[112] P. B. Paramonov, S. A. Paniagua, P. J. Hotchkiss, S. C. Jones, N. R. Armstrong, S. R. Marder, J.-L. Brédas, Chem. Mater. 20 (2008) 5131.

[113] Y. Paz, Beilstein J. Nanotechnol. 2 (2011) 845.

[114] P. J. Hotchkiss, S. C. Jones, S. A. Paniagua, A. Sharma, B. Kippelen, N. R. Armstrong, S. R. Marder, Accounts Chem. Res. 45 (2012) 337.

[115] A. M. B. do Rego, A. M. Ferraria, J. El Beghdadi, F. Debontridder, P. Brogueira, R. Naaman, M. R. Vilar, Langmuir 21 (2005) 8765.

[116] S. Yagyu, M. Yoshitake, N. Tsud, T. Chikyow, Jpn. J. Appl. Phys. 50 (2011) 081606.

[117] N. K. Mal, A. Bhaumik, M. Fujiwara, M. Matsukata, Micropor. Mesopor. Mat. 93 (2006) 40.

[118] J. Svoboda, V. Zima, L. Beneš, K. Melánová, M. Vlček, M. Trchová, J. Phys. Chem. Solids 69 (2008) 1439.

[119] E. Jaimez, A. Bortun, G. B. Hix, J. R. García, J. Rodríguez, R. C. T. Slade, J. Chem. Soc., Dalton Trans. (1996) 2285.

[120] P. Persson, E. Laiti, L.-O. Öhman, J. Colloid Interf. Sci. 190 (1997) 341.

[121] W. O. Yah, A. Takahara, Y. M. Lvov, J. Am. Chem. Soc. 134 (2012) 1853.

[122] C. Viornery, Y. Chevolot, D. Léonard, B.-O. Aronsson, P. Péchy, H. J. Mathieu, P. Descouts, M. Grätzel, Langmuir 18 (2002) 2582.

[123] B. Adolphi, E. Jähne, G. Busch, X. Cai, Anal. Bioanal. Chem. 379 (2004) 646.

[124] G. Zorn, I. Gotman, E. Y. Gutmanas, R. Adadi, G. Salitra, C. N. Sukenik, Chem. Mater. 17 (2005) 4218.

[125] N. Tsud, M. Yoshitake, Surf. Sci. 601 (2007) 3060.

[126] K. Domen, Y. Ebina, S. Ikeda, A. Tanaka, J. N. Kondo, K. Maruya, Catal. Today 28 (1996) 167.

[127] N. Kimura, Y. Kato, R. Suzuki, A. Shimada, S. Tahara, T. Nakato, K. Matsukawa, P. H. Mutin, Y. Sugahara, Langmuir 30 (2014) 1169.

[128] P. C. LeBaron, Z. Wang, T. J. Pinnavaia, Appl. Clay Sci. 15 (1999) 11.

[129] D. Schmidt, D. Shah, E. P. Giannelis, Curr. Opin. Solid St. M. 6 (2002) 205.

[130] S. S. Ray, M. Okamoto, Prog. Polym. Sci. 28 (2003) 1539.

[131] S. J. Ahmadi, Y. D. Huang, W. Li, J. Mater. Sci. 39 (2004) 1919.

[132] O. Becker, G. P. Simon, Adv. Polym. Sci. 179 (2005) 29.

[133] E. T. Thostenson, C. Li, T.-W. Chou, Compos. Sci. Technol. 65 (2005) 491.

[134] A. Usuki, N. Hasegawa, M. Kato, Adv. Polym. Sci. 179 (2005) 135.

[135] Q. H. Zeng, A. B. Yu, G. Q. Lu, D. R. Paul, J. Nanosci. Nanotechno. 5 (2005) 1574.

[136] A. C. Balazs, T. Emrick, T. P. Russell, Science 314 (2006) 1107.

[137] J. Baur, E. Silverman, MRS Bull. 32 (2007) 328.

[138] D. L. Hunter, K. W. Kamena, D. R. Paul, MRS Bull. 32 (2007) 323.

[139] F. Hussain, M. Hojjati, M. Okamoto, R. E. Gorga, J. Compos. Mater. 40 (2006) 1511.

[140] R. Krishnamoorti, MRS Bull. 32 (2007) 341.

[141] R. A. Vaia, J. F. Maguire, Chem. Mater. 19 (2007) 2736.

[142] K. I. Winey, R. A. Vaia, MRS Bull. 32 (2007) 314.

[143] D. R. Paul, L. M. Robeson, Polymer 49 (2008) 3187.

[144] Q. H. Zeng, A. B. Yu, G. Q. Lu, Prog. Polym. Sci. 33 (2008) 191.

[145] R. F. Gibson, Compos. Struct. 92 (2010) 2793.

[146] C. Li, J. Han, C. Y. Ryu, B. C. Benicewicz, Macromolecules 39 (2006) 3175.

[147] M. E. Mackay, A. Tuteja, P. M. Duxbury, C. J. Hawker, B. Van Horn, Z. Guan,
       G. Chen, R. S. Krishnan, Science 311 (2006) 1740.

[148] L. S. Schadler, S. K. Kumar, B. C. Benicewicz, S. L. Lewis, S. E. Harton, MRS
       Bull. 32 (2007) 335.

[149] Y. Li, B. C. Benicewicz, Macromolecules 41 (2008) 7986.

[150] P. Akcora, H. Liu, S. K. Kumar, J. Moll, Y. Li, B. C. Benicewicz, L. S. Schadler,
       D. Acehan, A. Z. Panagiotopoulos, V. Pryamitsyn, V. Ganesan, J. Ilavsky, P.
       Thiyagarajan, R. H. Colby, J. F. Douglas, Nat. Mater. 8 (2009) 354.

[151] Y. Wu, J. Zhang, H. Zhao, J. Polym. Sci. A1 47 (2009) 1535.

[152] D. Maillard, S. K. Kumar, B. Fragneaud, J. W. Kysar, A. Rungta, B. C.
       Benicewicz, H. Deng, L. C. Brinson, J. F. Douglas, Nano Lett. 12 (2012) 3909.

[153] S. K. Kumar, N. Jouault, B. Benicewicz, T. Neely, Macromolecules 46 (2013)
       3199.

[154] G. M. Odegard, T. C. Clancy, T. S. Gates, Polymer 46 (2005) 553.

[155] K. E. Strawhecker, E. Manias, Chem. Mater. 12 (2000) 2943.

[156] K. E. Strawhecker, E. Manias, Macromolecules 34 (2001) 8475.

[157] J.-H. Chang, T.-G. Jang, K. J. Ihn, W.-K. Lee, G. S. Sur, J. Appl. Polym. Sci. 90 (2003) 3208.

[158] J.-M. Yeh, M.-Y. Yu, S.-J. Liou, J. Appl. Polym. Sci. 89 (2003) 3632.

[159] Y.-H. Yu, C.-Y. Lin, J.-M. Yeh, W.-H. Lin, Polymer 44 (2003) 3553.

[160] L.-M. Döppers, C. Breen, C. Sammon, Vib. Spectrosc. 35 (2004) 27.

[161] J. C. Grunlan, A. Grigorian, C. B. Hamilton, A. R. Mehrabi, J. Appl. Polym. Sci. 93 (2004) 1102.

[162] L.-P. Wang, Y.-P. Wang, F.-A. Zhang, Polym. Polym. Compos. 13 (2005) 839.

[163] S. G. Adoor, M. Sairam, L. S. Manjeshwar, K. V. S. N. Raju, T. M. Aminabhavi, J. Membrane Sci. 285 (2006) 182.

[164] J. Gaume, C. Taviot-Gueho, S. Cros, A. Rivaton, S. Thérias, J.-L. Gardette, Sol. Energ. Mat. Sol. C 99 (2012) 240.

[165] H. J. Ploehn, C. Liu, Ind. Eng. Chem. Res. 45 (2006) 7025.

[166] D. J. Greenland, J. Coll. Sci. Imp. U. Tok. 18 (1963) 647.

[167] W. W. Emerson, M. Raupach, Aust. J. Soil Res. 2 (1964) 46.

[168] B. K. G. Theng, Clay Clay Miner. 18 (1970) 357.

[169] K. Suzuki, T. Mori, K. Kawase, H. Sakami, S. Iida, Clay Clay Miner. 36 (1988) 147.

[170] K. A. Carrado, P. Thiyagarajan, D. L. Elder, Clay Clay Miner. 44 (1996) 506.

[171] P. F. Luckham, S. Rossi, Adv. Colloid Interfac. 82 (1999) 43.

[172] S. G. de Bussetti, E. A. Ferreiro, Clay Clay Miner. 52 (2004) 334.

[173] L. E. Nielsen, J. Macromol. Sci. A1 (1967) 929.

[174] E. L. Cussler, S. E. Hughes, W. J. Ward, A. Rutherford, J. Membrane Sci. 1988, 38 (1988) 161.

[175] W. R. Falla, M. Mulski, E. L. Cussler, J. Membrane Sci. 119 (1996) 129.

[176] N. K. Lape, E. E. Nuxoll, E. L. Cussler, J. Membrane Sci. 236 (2004) 29.

[177] W. B. Russel, D. A. Saville, W. R. Schowalter, Colloidal Dispersions; Cambridge University: Cambridge, 1989.

[178] G. Fleer, M. A. Cohen Stuart, J. M. H. M. Scheutjens, T. Cosgrove, B. Vincent, Polymers at Interfaces; Chapman & Hall: London, 1993.

[179] V. Chaplain, M. L. Janex, F. Lafuma, C. Graillat, R. Audebert, Colloid Polym. Sci. 273 (1995) 984.

[180] K. Backfolk, J. B. Rosenholm, J. Husband, D. Eklund, Colloid Surface A 275 (2006) 133.

[181] T. F. Tadros, Colloid Surface 18 (1986) 137.

[182] W.-L. Wu, M. Shibayama, S. Roy, H. Kurokawa, L. D. Coyne, S. Nomura, R. S. Stein, Macromolecules 23 (1990) 2245.

[183] P. J. Willcox, D. W. Howie Jr., K. Schmidt-Rohr, D. A. Hoagland, S. P. Gido, S. Pudjijanto, L. W. Kleiner, S. Venkatraman, J. Polym. Sci. Pol. Phys. 37 (1999) 3438.

[184] T. Kanaya, N. Takahashi, H. Takeshita, M. Ohkura, K. Nishida, K. Kaji, Polym. J. 44 (2012) 83.

[185] J. W. Thompson, H. A. Stretz, P. E. Arce, H. Gao, H. J. Ploehn, J. He, J. Appl. Polym. Sci. 126 (2012) 1600.

[186] Y. Cui, J. S. van Duijneveldt, Langmuir 26 (2010) 17210.

[187] S. Rossi, P. F. Luckham, T. F. Tadros, Colloid Surface A 215 (2003) 1.

[188] P. Alexandridis, T. Nivaggioli, T. A. Hatton, Langmuir 11 (1995) 1468.

[189] A. A. Sapalidis, F. K. Katsaros, T. A. Steriotis, N. K. Kanellopoulos, J. Appl. Polym. Sci. 123 (2012) 1812.

[190] S. Chibowski, M. Paszkiewicz, M. Krupa, Powder Technol. 107 (2000) 251.

Appendix A: Typical Solution Blending Recipes

MMT stock suspension weight fraction =   0.009058

Untreated MMT/PVOH Blends Recipe

Material	Amount		% Solids	% Polymer
DI Water	9.933	g		
PVOH matrix	1.500	g	90.0%	5.0%
Dry MMT solids	0.167	g	10.0%	
Volume of MMT stock required	18.400	ml		
Total:	*30.000*	*g*	*100.0%*	*5.0%*

Note: MMT stock is in water

0.5% PV$_{11}$MMT Stock Suspension Recipe

Material	Amount		% Solids	% Polymer
DI Water	85.719	g		
PV$_{11}$	0.625	g	64.3%	0.5%
Dry MMT solids	0.347	g	35.7%	
Volume of MMT stock required	38.309	ml		
Total:	*125.000*	*g*	*100.0%*	*0.5%*

PV$_{11}$MMT/PVOH Blends Recipe

Material	Amount		% Solids	% Polymer
DI Water	8.200	g		
[Total Polymer]	0.534	g	90.0%	1.78%
PVOH matrix	0.427	g		1.42%
PV$_{11}$MMT stock	21.373	g		
[PV$_{11}$]	0.107	g		0.36%
[Dry MMT solids]	0.059	g	10.0%	
Total:	*30.000*	*g*	*100.0%*	*1.78%*

Note: [] are not added to the blend

0.1% F-MMT Stock Suspension Recipe

Material	Amount		% Solids	% Polymer
DI Water	83.100	g		
F108	0.125	g	25.0%	0.1%
Dry MMT solids	0.375	g	75.0%	
Volume of MMT stock required	41.400	ml		
Total:	*125.000*	*g*	*100.0%*	*0.1%*

F-MMT/PVOH Blends Recipe

Material		Amount		% Solids	% Polymer
DI Water		7.200	g		
	[Total Polymer]	0.600	g	90.0%	2.00%
PVOH matrix		0.578	g		1.93%
F-MMT stock		22.222	g		
	[F108]	0.022	g		0.07%
	[Dry MMT solids]	0.067	g	10.0%	
Total:		*30.000*	*g*	*100.0%*	*2.00%*

Note: [] are not added to the blend

Appendix B: Copyright Transfer Agreement

Title of your thesis / dissertation	Surface Modification of Nanoplatelets in Polymer Nanocomposites
Expected completion date	Dec 2014
Expected size (number of pages)	175
Total	0.00 USD
Terms and Conditions	

TERMS AND CONDITIONS

162

permission of the respective copyright owner. You may not alter, remove or suppress in any manner any copyright, trademark or other notices displayed by the Wiley Materials. You may not license, rent, sell, loan, lease, pledge, offer as security, transfer or assign the Wiley Materials on a stand-alone basis, or any of the rights granted to you hereunder to any other person.

- The Wiley Materials and all of the intellectual property rights therein shall at all times remain the exclusive property of John Wiley & Sons Inc, the Wiley Companies, or their respective licensors, and your interest therein is only that of having possession of and the right to reproduce the Wiley Materials pursuant to Section 2 herein during the continuance of this Agreement. You agree that you own no right, title or interest in or to the Wiley Materials or any of the intellectual property rights therein. You shall have no rights hereunder other than the license as provided for above in Section 2. No right, license or interest to any trademark, trade name, service mark or other branding ("Marks") of WILEY or its licensors is granted hereunder, and you agree that you shall not assert any such right, license or interest with respect thereto.

- NEITHER WILEY NOR ITS LICENSORS MAKES ANY WARRANTY OR REPRESENTATION OF ANY KIND TO YOU OR ANY THIRD PARTY, EXPRESS, IMPLIED OR STATUTORY, WITH RESPECT TO THE MATERIALS OR THE ACCURACY OF ANY INFORMATION CONTAINED IN THE MATERIALS, INCLUDING, WITHOUT LIMITATION, ANY IMPLIED WARRANTY OF MERCHANTABILITY, ACCURACY, SATISFACTORY QUALITY, FITNESS FOR A PARTICULAR PURPOSE, USABILITY, INTEGRATION OR NON-INFRINGEMENT AND ALL SUCH WARRANTIES ARE HEREBY EXCLUDED BY WILEY AND ITS LICENSORS AND WAIVED BY YOU

- WILEY shall have the right to terminate this Agreement immediately upon breach of this Agreement by you.
- You shall indemnify, defend and hold harmless WILEY, its Licensors and their respective directors, officers, agents and employees, from and against any actual or threatened claims, demands, causes of action or proceedings arising from any breach of this Agreement by you.

- IN NO EVENT SHALL WILEY OR ITS LICENSORS BE LIABLE TO YOU OR ANY OTHER PARTY OR ANY OTHER PERSON OR ENTITY FOR ANY SPECIAL, CONSEQUENTIAL, INCIDENTAL, INDIRECT, EXEMPLARY OR PUNITIVE DAMAGES, HOWEVER CAUSED, ARISING OUT OF OR IN CONNECTION WITH THE DOWNLOADING, PROVISIONING, VIEWING OR USE OF THE MATERIALS REGARDLESS OF THE FORM OF ACTION, WHETHER FOR BREACH OF CONTRACT, BREACH OF WARRANTY, TORT, NEGLIGENCE, INFRINGEMENT OR OTHERWISE (INCLUDING, WITHOUT LIMITATION, DAMAGES BASED ON LOSS OF PROFITS, DATA, FILES, USE, BUSINESS OPPORTUNITY OR CLAIMS OF THIRD PARTIES), AND WHETHER OR NOT THE PARTY HAS BEEN ADVISED OF THE POSSIBILITY OF SUCH DAMAGES. THIS LIMITATION SHALL APPLY NOTWITHSTANDING ANY FAILURE OF ESSENTIAL PURPOSE OF ANY LIMITED REMEDY PROVIDED HEREIN.

- Should any provision of this Agreement be held by a court of competent jurisdiction to be illegal, invalid, or unenforceable, that provision shall be deemed amended to

achieve as nearly as possible the same economic effect as the original provision, and the legality, validity and enforceability of the remaining provisions of this Agreement shall not be affected or impaired thereby.

- The failure of either party to enforce any term or condition of this Agreement shall not constitute a waiver of either party's right to enforce each and every term and condition of this Agreement. No breach under this agreement shall be deemed waived or excused by either party unless such waiver or consent is in writing signed by the party granting such waiver or consent. The waiver by or consent of a party to a breach of any provision of this Agreement shall not operate or be construed as a waiver of or consent to any other or subsequent breach by such other party.

- This Agreement may not be assigned (including by operation of law or otherwise) by you without WILEY's prior written consent.

- Any fee required for this permission shall be non-refundable after thirty (30) days from receipt by the CCC.

- These terms and conditions together with CCC�s Billing and Payment terms and conditions (which are incorporated herein) form the entire agreement between you and WILEY concerning this licensing transaction and (in the absence of fraud) supersedes all prior agreements and representations of the parties, oral or written. This Agreement may not be amended except in writing signed by both parties. This Agreement shall be binding upon and inure to the benefit of the parties' successors, legal representatives, and authorized assigns.

- In the event of any conflict between your obligations established by these terms and conditions and those established by CCC�s Billing and Payment terms and conditions, these terms and conditions shall prevail.

- WILEY expressly reserves all rights not specifically granted in the combination of (i) the license details provided by you and accepted in the course of this licensing transaction, (ii) these terms and conditions and (iii) CCC�s Billing and Payment terms and conditions.

- This Agreement will be void if the Type of Use, Format, Circulation, or Requestor Type was misrepresented during the licensing process.

- This Agreement shall be governed by and construed in accordance with the laws of the State of New York, USA, without regards to such state�s conflict of law rules. Any legal action, suit or proceeding arising out of or relating to these Terms and Conditions or the breach thereof shall be instituted in a court of competent jurisdiction in New York County in the State of New York in the United States of America and each party hereby consents and submits to the personal jurisdiction of such court, waives any objection to venue in such court and consents to service of process by registered or certified mail, return receipt requested, at the last known address of such party.

165

Creative Commons Attribution Non-Commercial License

The Creative Commons Attribution Non-Commercial (CC-BY-NC) License permits use, distribution and reproduction in any medium, provided the original work is properly cited and is not used for commercial purposes.(see below)

Creative Commons Attribution-Non-Commercial-NoDerivs License

The Creative Commons Attribution Non-Commercial-NoDerivs License (CC-BY-NC-ND) permits use, distribution and reproduction in any medium, provided the original work is properly cited, is not used for commercial purposes and no modifications or adaptations are made. (see below)

Use by non-commercial users

For non-commercial and non-promotional purposes, individual users may access, download, copy, display and redistribute to colleagues Wiley Open Access articles, as well as adapt, translate, text- and data-mine the content subject to the following conditions:

- The authors' moral rights are not compromised. These rights include the right of "paternity" (also known as "attribution" - the right for the author to be identified as such) and "integrity" (the right for the author not to have the work altered in such a way that the author's reputation or integrity may be impugned).

- Where content in the article is identified as belonging to a third party, it is the obligation of the user to ensure that any reuse complies with the copyright policies of the owner of that content.

- If article content is copied, downloaded or otherwise reused for non-commercial research and education purposes, a link to the appropriate bibliographic citation (authors, journal, article title, volume, issue, page numbers, DOI and the link to the definitive published version on **Wiley Online Library**) should be maintained. Copyright notices and disclaimers must not be deleted.

- Any translations, for which a prior translation agreement with Wiley has not been agreed, must prominently display the statement: "This is an unofficial translation of an article that appeared in a Wiley publication. The publisher has not endorsed this translation."

Use by commercial "for-profit" organisations

Use of Wiley Open Access articles for commercial, promotional, or marketing purposes requires further explicit permission from Wiley and will be subject to a fee. Commercial purposes include:

- Copying or downloading of articles, or linking to such articles for further

redistribution, sale or licensing;

- Copying, downloading or posting by a site or service that incorporates advertising with such content;

- The inclusion or incorporation of article content in other works or services (other than normal quotations with an appropriate citation) that is then available for sale or licensing, for a fee (for example, a compilation produced for marketing purposes, inclusion in a sales pack)

- Use of article content (other than normal quotations with appropriate citation) by for-profit organisations for promotional purposes

- Linking to article content in e-mails redistributed for promotional, marketing or educational purposes;

- Use for the purposes of monetary reward by means of sale, resale, licence, loan, transfer or other form of commercial exploitation such as marketing products

- Print reprints of Wiley Open Access articles can be purchased from: corporatesales@wiley.com

Further details can be found on Wiley Online Library
http://olabout.wiley.com/WileyCDA/Section/id-410895.html

Other Terms and Conditions:

v1.9

Questions? customercare@copyright.com or +1-855-239-3415 (toll free in the US) or +1-978-646-2777.

Gratis licenses (referencing $0 in the Total field) are free. Please retain this printable license for your reference. No payment is required.